UNIVERSIDADE DE COIMBRA
FACULDADE DE CIÊNCIAS E TECNOLOGIA
Departamento de Ciências da Terra

Integrating Geophysical Airborne and Geological Data to Characterized Karst Aquifer at Baucau Plateau, Baucau Municipality Timor-Leste

Moisés Soares

MESTRADO EM GEOCIÊNCIAS-RECURSOS GEOLÓGICOS

Julho, 2018

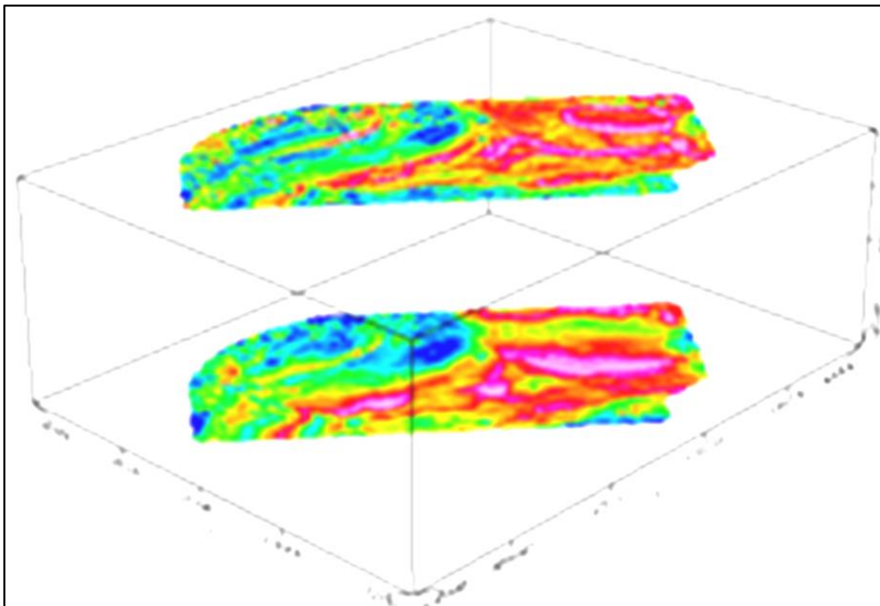

UNIVERSIDADE DE COIMBRA
FACULDADE DE CIÊNCIAS E TECNOLOGIA
Departamento de Ciências da Terra

Integrating Geophysical Airborne and Geological Data to Characterize Karst Aquifer at Baucau Plateau, Baucau Municipality Timor Leste

Moisés Soares

MESTRADO EM GEOCIÊNCIAS
Área de especialização em Recursos Geológicos

Orientadores científicos
Prof. Doutor Fernando Pedro Ortega Oliveira Figueiredo, F.C.T.U.C
Prof. Doutor José Manuel Martins de Azevedo, F.C.T.U.C

Julho,2018

Acknowledgment

Firstly, I want to express my sincere thanks to the Almighty God Lord Jesus Christ for knowledge and grace to finalize thesis. My deepest recognition of intellectual quality and experience of my supervisor Prof. Doutor Fernando Pedro Ortega Oliveira Figueiredo and Prof. Doutor José Manuel Martins de Azevedo who guide me in my academic on Master Degree in Geoscience Universidade Coimbra. They had been helped me in developing and enhance my intellectual academic with quality in airborne geophysical data to characterize groundwater karst aquifer.

Also, I wish to express my thanks to Prof.Dr Joao Pratas, Prof.Dr Nelson Edgar Viegas Rodrigues, and Prof.Dr Ana Machadino guide me during in data interpretation.

I wish to express my gratitude to H.E President of IPG Mr.Helio Gutteres for giving me the opportunity and funding to pursue my master degree in Universidade Coimbra Portugal. Also founding me to collect geological information in the field.

I wish to express my thanks to Mr. Osrorio Chief of Groundwater Investigation of DNGRA who provided Geophysical airborne data and dye tracing data for the thesis

I wish to express my thanks to Mr. Terencio National Director of DNMG Timor Leste provide rainfall data to use in this thesis.

I wish to express my thank to Mr.Craig who share groundwater data in Timor Leste and knowledge in groundwater survey in entire the Timor Leste especially Baucau plateau.

My thank to the colleague of IPG Mr. Ernesto who always helps me in LIDAR data interpretation.

Special thank to my all colleagues from IPG Timor Leste who pursue the master degree in the same program and in the Doctoral program in special Victor Alleluia de Sousa, Frederico Carlos, Juvencio do Rosario, Oktoviano Tilman, Marcal Ximenes and Job Brites dos Santos.

My special thank to my lovely father Roberto Soares and lovely mother Maria Evaristo (+) for their sacrifice and prayer, that I had an excellent education. They always care and encourage me in every situation. Their value of life and all message still alive in the heart.

My special thanks to my all beloved brothers and sister who always support me in opinion and knowledge during in studying process.

My special thank to my dear wife Natercia Tomas Martins for her love, affection, attention and praying that make strength me to face various difficulties during developing this thesis.

Abstract

Have conducted the characterization on geology and geophysics data to describe coral-reef limestone aquifer in the Baucau plateau at Baucau Municipality Timor Leste. High elevation in the southern plateau and slope down to the sea in the north and to the east and west escarpment. Airborne electromagnetic and airborne magnetic data conducted by FUGRO at 2nd July 2011. TDEM/SNMR information and boreholes data utilize to enhance the inversion of airborne geophysical data. Coral-reef limestone acts as an aquifer for groundwater and marl and grey claystone of Viqueqeu formation act as aquicludes. Baucau formation deposited overlying on a syncline with axes fold north eas-southwest. The underground drainage pattern generally controlled by the underlying structure, this is proved by the tracer where the groundwater flow follows the axes of the syncline. Airborne electromagnetic inversion reveals the thickness of limestone increase to the north (100 m) and decreases to the south-west (5-10 m). Numerous natural spring occurs in the gravity sliding zone, due to the aquicludes closer to the surface. Viqueqeu formation has the large implication of groundwater flow in the plateau. Based on borehole and field investigation the end of the lateral distribution of in the Bucoli and Uatabo (road to Laga). This interpretation supported by airborne magnetic which is the anomaly coincides with the end of the lateral distribution. It implicates seasonal spring emerge in the north, except in the east of Uatabo beach. To the Buraui and Bucoli emergence of natural spring related to the aquicludes closer to the surface. Further to the Uailili, Uatabo, and Berecoli the spring occurrence related to the gravity sliding. The discharge measurement and observation in the field indicated high discharge in the Uailili, Uainoe, Bucoli, Buruai, and Uaihisu, than the lower discharge in the Berecoli area. The diameter of the conduit from Uailiabere to Uailili spring obtained is about 0.5 m. Physical parameter measurement (pH, TDS, EC and Temperature) graphic show the groundwater in the same regime. Rainfall calculation in annual precipitation, high precipitation in the southern plateau (1500 mm/yr) and lower in the northern plateau (500 mm/yr). According to the result proposed further ground geophysical investigation in five different places. These locations are Buarui, Aubaca, Uailili, Fatumaca, and south of Baucau city.

Key words : Coral-reef limestone, underground drainage, airborne electromagnetic and airborne magnetic, dye tracing, Baucau formation

Abreviation

AEM : Airborne Electromagnetic
pH : Potential Hydrogen
TDS : Total Disolved Solid
EC : Electrical Conductivity
RTP : Reduce to Pole
FDEM : Frequency Domain Electromagnetic
TDEM : Time Domain Electromagnetic
SNMR : Surface Nuclear Magneric Resonance
FFT : Fast Fourier Transform
RMI : Residual Magnetic Intensity
HEM : Helicopter Electromagnetic
DNGRA : Direcção Nacional *de* Gestão dos Recursos de Água
BTC : Breakthrough Curve
DEM : Digital Elevation Model
LIDAR : Light Detection and Ranging
DNMG *:* Direcção Nacional Meteorologia e Geofisica
MOPTC : Ministerio Obras Publico e Telecomunicacao
CSV : Comma Separated Values
GDB : Geosoft Database
IGRF : International Geomagnetic Reference Field
SAS : Servisu Agua Saneamentu

Contents

List of Figure

List of Table

List of Graphic

Chapter 1. Introduction

1.1. Background of Study

Water is a very important natural resource in our daily life, it is a mysterious nature's hidden treasure all over the world. The scarcity of water is more intense in the developing countries where statistics show that 67% of the rural population have no access to safe water supply (Rosen and Vincent, 1999). The water that lies beneath the subsurface is called groundwater, and other water on the surface called surface water. Surface water lies above the surface such as rivers, lakes and so forth. Surface water is usually used for domestic purposes, by the reason it is very vulnerable to pollution and waterborne diseases. Groundwater which is found to exist below the surface in the soil pores, fractures within rocks, fissures and other weak geological features or zones is comparatively protected from pollution and evaporation and can be useful for both domestic and industrial purposes (John, _)

About 20 percent of the Earth's land surface is covered by carbonate karst formations (White, 1988), and roughly 20-25 percent of the global population depends largely or entirely on karst groundwater (Ford and Williams, 2007). When the rainfall and carbon dioxide in the atmosphere is dissolved making the rainwater acidic. That acidic rainwater passes through the joint/fracture and dissolving the limestone beneath the surface. The conduits and caves formed by chemical dissolution act as karst aquifer. Those waters flow through the conduits and fracture emerges to the surface are called karst spring (see Figure 1.1). The distribution of karst and potential flow path such as conduit and fracture of its karst very influenced to the location and the form of the karst spring. Karst springs are predominantly found at low topographic positions, such as valley floors, although they may be concealed beneath alluvium, rivers, lakes, or the sea. Some karst springs emerge in more elevated positions, usually as a result of geological or geomorphological controls on their position (Gunn, 2004). Karst aquifer recharge water flows rapidly through conduits and fractures and very slowly through the small pores and fissures where most of the recharged water may be stored for a long period (Kavosi and Raeise, 2014).

Fluorescent dyes are the most practical and widely used artificial tracers in karst aquifers. The mean transit time of dye can be approximated as the time difference between the injection and the centroid of the tracer-breakthrough curve. The main purpose of dye tracing is to know the connection among karst springs distributions (Benischke *et al.,* 2007). Due to the groundwater flow, path karst area is more difficult than non-karst area. The flow path of the groundwater in the karst is very dependent on the dissolution and fracture distribution in the subsurface. By the dye tracing method can provide an overview of groundwater flow in the karst.

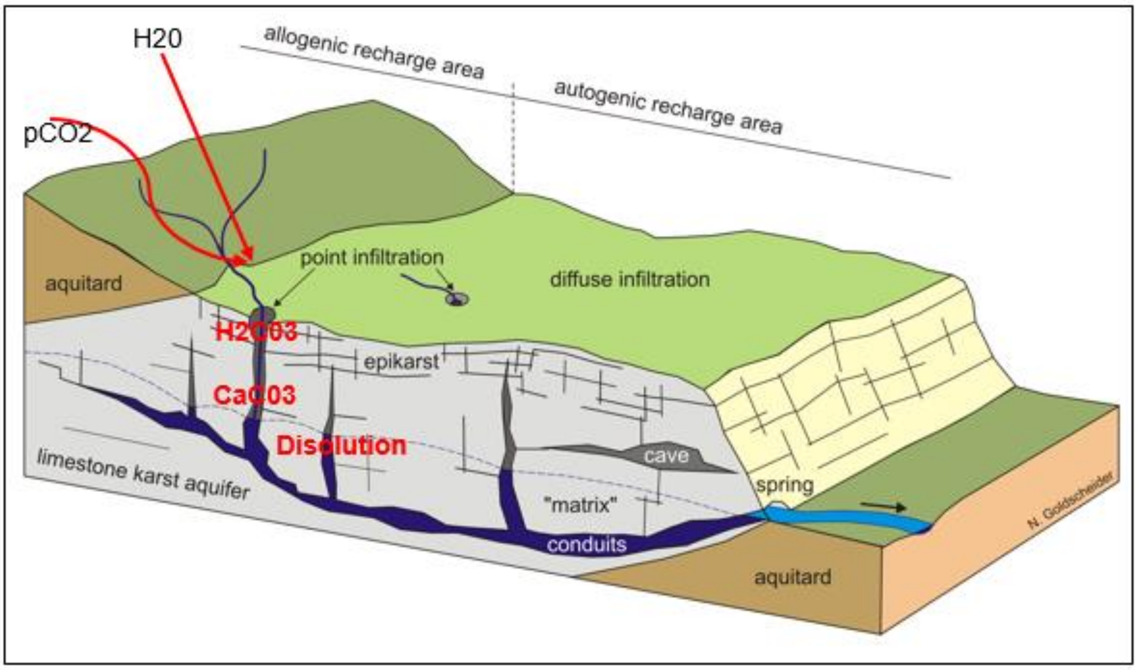

Figure 1. 1 Block diagram illustrating the hydrogeological functioning of a karst aquifer (Source: https://www.agw.kit.edu/img/Hydro/01_Karst_Block_Diagram.jpg)

Carbonate rocks do not contain sufficient magnetic minerals to cause magnetic anomalies. So the high resolution of ground magnetic survey rarely conducts in karst investigation. But the high resolution of magnetic can take place on the condition where high susceptibility sediments overlie karstic limestone. It is possible to map areas where the soils are concentrated, as with an active sinkhole (Smith *et al,* 2005). Magnetometers with 0.01 nT sensitivity accurately defined the shape of the doline and the properties of its filling material in e Zaragoza area, North East Spain (Mochales *et al,* 2008). Aeromagnetic data from a helicopter survey over a small study area centered on a sinkhole revealed a magnetic lineation aligned with a major fault juxtaposing the Edwards and Glen Rose limestone (Smith and Pratt, 2003). Many authors using airborne magnetic anomaly to identify the depth of the magnetic basement and the thickness of sedimentary package in the survey area. An airborne magnetic survey conducted in Onigbedu Nigeria with a purpose in limestone exploration, the low magnetic amplitude was interpreted to be indicative of the area of the shallow basement and the high amplitude of anomalies was interpreted to be an area of the deep basement (Oyedele *et al,* 2015). By the information obtained from magnetic anomaly field of karst feature in understanding geohydrology framework and helped to develop a geologic model of the aquifer.

AEM systems have been used for groundwater exploration purposes. Electromagnetic systems are suitable for providing information about the aquifer structures and water quality, respectively (Steuer *et al.* 2007). An airborne electromagnetic survey conducted at Sian Ka'an Biosphere Reserve located in Yucatán, Mexico. The apparent resistivity of airborne electromagnetic indicated low anomaly resistivity at caves (Supper *et al*, 2009). Another helicopter electromagnetic survey conducted in Northern Bexar County, Texas. This survey in objective to understand the groundwater flow path in cave karst of Edward Group. Electromagnetic inversion result of this survey able to separate different types of lithology based on resistivity values. Where the massive limestone of the Edwards Group commonly indicated high resistivity value (>1000 ohm-meters). Mudstones of the Glen Rose Formation have resistivity ranging from less than 10 to more than 50 ohmmeters (Smith *et al,* 2005). At the highest frequency, depths of exploration are just a few meters. At the lowest frequency, 400 Hz, the depth of exploration may be on the order of 80-m. These resistivities and depths can be used to construct resistivity-depth inversion sections. In the best case, the flight line intersects at a right angle and displays a sharp contrast at the discontinuity. In the worst case, the flight line runs parallel to the discontinuity, resulting in no abrupt change in signal contrast. Therefore, picks are readily discerned and more accurate when the flight line crosses a feature at an acute angle, whereas picks are more difficult and least accurate when the feature runs parallel between flight lines.

Baucau plateau dominantly by karst limestone in quaternary age. The morphology of the escarpment controlled by the underlying geological material. Where the coral limestone of the plateau is underlain by a layer of Viqueque formation (Audley-Charles,1968). There are large number of karst spring located in the East and West escarpment of Baucau Plateau. Some others localized in the marine terraces in the north of the Baucau Plateau. To understand the regional structure and karst depression of the study area using DEM of LIDAR data and aerial imagery to obtain delineation of geological structure and some topography depression such sinkholes distribution. The surface information, structure lineament, sinkhole presence and watershed on the surface as a guide to interpreted geophysical data. In the other side dye tracing information very helpful to know the connection between the cave and spring in the study area. To identify the hidden groundwater flow beneath the surface of karst, need to do study further in understanding of the geometry of the groundwater aquifer. One of the geophysics method very popular today is airborne electromagnetic method. AEM surveys have been used recently to provide subsurface information for hydrogeological characterization (Siemon et al., 2009).

The geophysical airborne data use in this work is conducted by FUGRO carried out for BESIK (Bee, Saneamentu no Ijiene iha Komunidade). By using RESOLVE electromagnetic system and magnetometer 1-Scintrex Cesium Vapour (CS-2 or CS-3) flown over Baucau Plateau between 2-3 June 2012. The traverse lines were flown with a spacing of 200 m and tie lines with a spacing of 2000 m. This survey uses five horizontal coplanar coils and one vertical coaxial coil, the altitude of the electromagnetic sensor about 30 m above ground level. The lowest frequencies penetrated to the deeper and on the contrary of the highest frequencies. The configuration of the coils is given in Table 1.1.

Table 1. 1 The configuration of the coils

Dipole Moment (Atm2)	**Orientation**	**Nominal Frequency (Hz)**	**Coil Separation**
310	Coplanar	300	7.93
175	Coplanar	1800	7.94
211	Coaxial	3300	9.06
70	Coplanar	8200	7.95
35	Coplanar	40000	7.93
18	Coplanar	140000	7.95

The RESOLVE utilize the transmitter and receiver to record the data. The primary magnetic field are generated by sinusoidal current through transmitter coil at a discrete frequency. The oscillation of the primary field induced eddy current and generate the secondary magnetic field. The secondary magnetic field measured by receiver coil, where the secondary magnetic value depends on the resistivity distribution beneath the surface (Steuer *et al,* 2007). The secondary field data comprising in-phase and quadrature. Those in-phase and quadrature are inverted into resistivity using two principal models: the homogeneous half-space and the layered half-space. The resulting parameter of the half-space inversion is the apparent resistivity (or half-space resistivity), which is the inverse of the apparent conductivity (Siemon *et al*, 2009). As we know that in karst area the groundwater is flowed through underground conduit often connect to the land surface via sinkhole and caving. The sinkhole and caving serve as agents or pathway for groundwater flow in the karst aquifer. The conduits under the surface can cause significant contrast of some physical properties, where underground void filled by groundwater has lower resistivity than most surrounding rocks and a void filled by air has higher resistivity than most geologic material (Zhu *et al.,* 2011). This provides much more effective and economical way to reduce the overall amount of drillings and to improve locating test drilling for verification (Metwaly & Alfouzan, 2013).

1.2 Objectives

In karst aquifer investigation, it is very difficult to understand the underground drainage pattern. Therefore, by combining various data, it is possible to reveal the karst groundwater aquifer in entire Baucau plateau.

Based on the available data, the main objective of this work is classified to:

1. **Primary objective**
    - To understand spatial distribution (vertical stratigraphy and lateral distribution) and organization coral-reef limestone of Baucau formation.
    - To understand its implication on groundwater storage and circulation in entire Baucau plateau.
2. **Secondary objective**
    - To characterized geophysical and geological data to reveal the limestone karst aquifer in entire Baucau plateau including the escarpment of Baucau plateau area.

1.3 Methodologies

1.3.1 Literature Review

Surface of Baucau plateau covered by coral-reef limestone of Baucau formation. Audley-Charles (1968) reported Baucau limestone deposited after underlying formation folded. Underlying formation is Viquque formation, this formation comprising of marl and grey clay stone.

Mentzner (1977), classified physiography unit based on morphological characteristic to be four zone namely; Baucau plateau, east and west escarpment, marine terraces zone and coastal zone. There are several work has conducted groundwater investigation over Baucau karst area. Furnes (2011a) reported the connection of groundwater in Baucau plateau by studying dye tracing. The all result shown that the drainage pattern trending to the eastern escarpment.

Ley-Cooper and Munday (2011) establish TDEM ans SNMR ground survey Than DNGRA follow up by drilling, the result of drilling indicate a thick limestone unit with an upper unsaturated and poorly conductive part. Where the groundwater was encountered modelled conductivities were noted to increase. They assumed that limestone was underlain by a saturated clay unit, which was interpreted to coincide with the high ground conductivities observed in the soundings.

Ley-Cooper and Davis (2015a) built a conceptual 3D conductivity structure after re-calibrating and re-inventing the AEM survey. By the sharp conductivity between the undelaying materials which is clearly identifiable in the profile-section. They are confident interpreted that it is directly relates to the massive hard coral limestone, which controls the topography of the plateau. Due to the homogeneity of the conductivity, the thickness of the first layer to be a direct detection of the thickness of the Baucau Formation and enabled to predict to be preferential flow paths within the Baucau limestone.

Ornai (2017) reported that several sprigs in the east escarpment of Baucau plateau localized in lithology contact and another one is Uailia in the north of Buacau plateau emerge in the fault structure.

1.3.2 Data Collection

For the purpose of this research, there are numerous methods and procedures applied such as secondary data collection and field investigation and measurements.The secondary data were collected from the various relevant institution. The main secondary data of this research are geophysical airborne electromagnetic and magnetic data. Due to the airborne geophysical data important to obtain the spatial distribution of coral-reef limestone.

Field investigation and measurements conducted in order to enhance geophysical interpretation. The main advantage for doing the bedding measurement is to reveal the structure which controls the underground drainage pattern. Geological struture (fracture and fold) direction often used to define drainage pattern and groundwater flow path.Thus, always required understanding of the geological setting of study area. The description of field field investigation and measurements as below.

1.3.2.1 Structural Assessment

The main objective of field investigation is to obtain the bedding stratification of Viqueqeu fromation. This fromation has influence of natural spring emergence in field. Regional geological map of Audley-Charles (1968) as a guide during in the field. According to the Audley-Charles (1968) Viqueqeu fromation composed of marl and greyclaystone. The distribution of this formation abundantly in the eastern eascarpment, western escarpment and southern of Baucau plateau. Thus, the structural assessment will fosuc on these escarpments area. In other hand, cross check the boundary of lithilogy was interpreted based on the DEM LIDAR and aerial imagery dataset.

The key feature to measure in the field is the orientation of bedding. Normally sedimentary layer deposited in horizontal condition, if the layer observed in the field no longer horizontal we can inferred that they have been effected by tectonic force. Usually the outcrop which is exposed on the surface become tilted and folded.

To express the orientation of beds in two values such as: strike and dip of the layer exposed on the surface. Strike indicates the distribution of layer on the surface and dip indicates the line perpendicular to strike. Measurement of the orientation is done with geological compass that has clinometer, which is a device for measuring vertical angles. These values may help to imagine the type of structure under the surface. To guess the type structure on the field by placed strike and dip symbol on the map. These strike and dip indicate the orientation of beds shown the fold and fault. Due to Baucau karst limestone deposited on the Viqueqeu formation, probably coral-reed limestone of Baucuau controlled by underlying formation. In the karst normally drainage pattern formed according to the hardness of limestone on dissolution. In other hand the drainage pattern also influenced by the topography of underlying formation. So, structure of Viqueque formation is very important to understand the drainage pattern in the Baucau plateau.

1.3.2.2 Main Natural Spring Identification

Natural identification in the field very important, due to the natural spring consider as discharge area. They may aim to identify some characteristic of the karst aquifer. Seasonal natural spring normally emerges in the rain to wet season and permanent natural spring normally connected directly to the main underground drainage. The characteristic of natural spring may aim to interpret the main underground drainage pattern direction.

1.3.2.3 In situ Physico-Chemical and Flow Rate Measurements

The specific physico-chemical of groundwater will be measured in the site. Those parameters are pH, TDS and EC. In the karst area they used to identify the origin of groundwater and their flow regimes. The Hanna Instrument was used to measure the physico-chemical in the field. The relationship between EC and T indicate the existence of groups of water with different origins. Aquifers are classified as deep and shallow circulating water based on the fact that groundwater samples with high EC, high T represent the deep circulating water, while low EC, low T represent the shallow circulating water (Mazor, 1991).

The flow rate mesurements conducted with float method. The measurments will focused on the area considering main groundwater discharge. The record time repeated more three time than calculated average time. By the distance and average time to calculate the velocity of water. To obtain discharge value by multiplying velocity value to cross-sectional area value. The discharge value corrected with correction factor (0.8). The discharge value may help to understand the direction of groundwater flow. The equation 1.1 below was applied for the float method.

Discharge (Q) = Velocity x Area **(Eq.1.1)**

Besides, to identify the main flow path direction on the underground drainage pattern. Generally discharge from aquifer is always higher than the recharge into the aquifer. The difference is usually assumed to be balanced by contribution of neighboring drainage (Demiroglu, 2016). Springs with high discharge variability can indicate a high degree of transport properties of the aquifer and the quick response of the system to recharge.

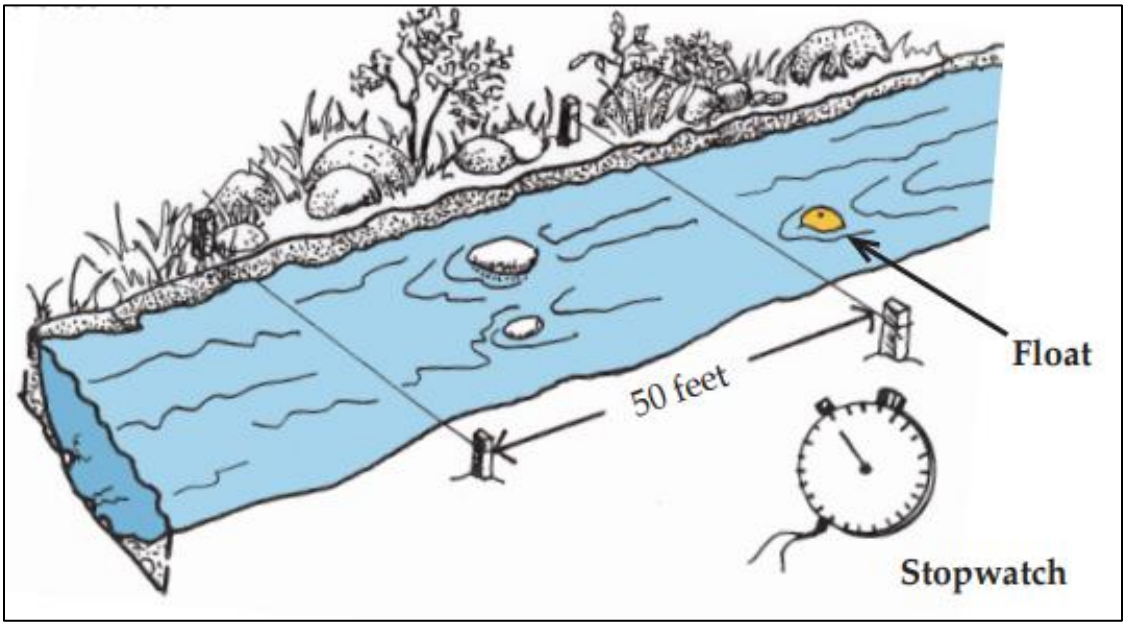

Figure 1. 2 Flow rate measurements with float method (Michaud and Wierenga, 2005)

1.3.3 Data Processing and Interpretation

In this work used various data to know Baucau karst aquifers such as geophysical airborne data, rainfall data, dye tracing data and borehole data. The data processing will focus on geophysical airborne data. The step of the data processing and interpretation demonstrated in Chapter 4 and Chapter 5. In other side dye tracing data which is extracted from the report used to obtain the mean transit time. The mean transit time used to obtain the diameter of the conduit.

1.4 Research Limitation

Although using various data in the research, every study has limitation. This thesis had the following limitations:

1. The geophysical airborne survey only covered the plateau area
2. Limit of time, the field cross check and bedding measurements conducted only several outcrops.

Chapter 2. Fundamentals of Geophysical Applied Method

Airborne geophysical method measured physical properties of rock underlying beneath the earth surface. Combination of magnetic and electromagnetic airborne have been used for groundwater exploration in the karst area. Magnetic surveys rarely conduct in karst investigation due to carbonate rocks do not contain sufficient magnetic minerals to cause magnetic anomalies. In some condition aeromagnetic revealed magnetic lineation aligned with a major fault. By the information obtained from magnetic anomaly field of karst feature in understanding the geohydrologic framework and helped to develop the geological model of the aquifer. Multi frequencies of airborne electromagnetic suitable for providing information about the karst aquifer structures. Airborne electromagnetic indicated low anomaly resistivity at caves and separate different types of lithology based on resistivity values. Massive limestone commonly indicated high resistivity value and clay low resistivity value.

2.1 Basic Concept of Magnetic Method

2.1.1 Magnetic Field

The magnetic consist of two poles. The poles of the magnet, which tends to point in the direction of the Earth's North Pole is called the north-seeking or positive pole, and this is balanced by a south-seeking, or negative pole, of identical strength at the opposite end of the magnet (Kearey *et al*, 2002). The Force between (F) two pole (P1 and P2) separated by a distance (r) is given by Newton's law as follow (Hinze *et al,* 2013).

$$\boldsymbol{F = \frac{\mu_0\, P_1 P_2}{4\pi\mu_R r^2}} \qquad \textbf{(Eq. 2.1)}$$

μ_0 is the magnetic permeability of the vacuum and μ_R is the corresponds to the relative magnetic permeability of the medium separating the poles. The unit of magnetic stregnht is in nT.

In geophysics exploration is concerned geomagnetic field of the earth. The geomagnetic of the earth composed of three parts such as: the main magnetic field, external magnetic field and local magnetic field. Spherical observed analysis of the magnetic field shows that the origin of the main magnetic field 99% inside the earth. Occurrences of this main magnetic field caused by convection currents of conducting material circulating in the outer core of the earth. The external magnetic field associated with electrical currents in the ionized layers of the upper atmosphere. In geophysics exploration, the main and external magnetic field consider as noise. Thus, in processing step both noise remove first from data. The local change in the main magnetic field obtained from variations in the magnetic minerals content of near-surface rock. The anomalies of local field large enough compared to the main magnetic field. Generally, the local magnetic anomalies from shallow deep, due at very deep the temperature is higher. Based on Curie point below 40 Km the temperature increase to be 550^{0}C, at that higher temperature, the rocks lose their magnetic properties. Thus, local anomalies associated with the rock lied above upper crust of the earth (Telford, *et al,* 1990). Variations in the strength of magnetic anomaly depend on source geometry and orientation of the body's magnetism (Dentith and Mudge, 2014).

2.1.2 Magnetism Rocks and Soil

Basis on magnetic susceptibility of distinguished in three classes: diamagnetis, paramagnetism and ferromagnetism. Diamagnetims occur when an external magnetic field is applied the electrons orbit opposes the applied field, producing a weak negative susceptibility (Hinze *et al,*2013). Generally, the minerals in diamagnetism class are quartz and calcite (see Table 2.1).

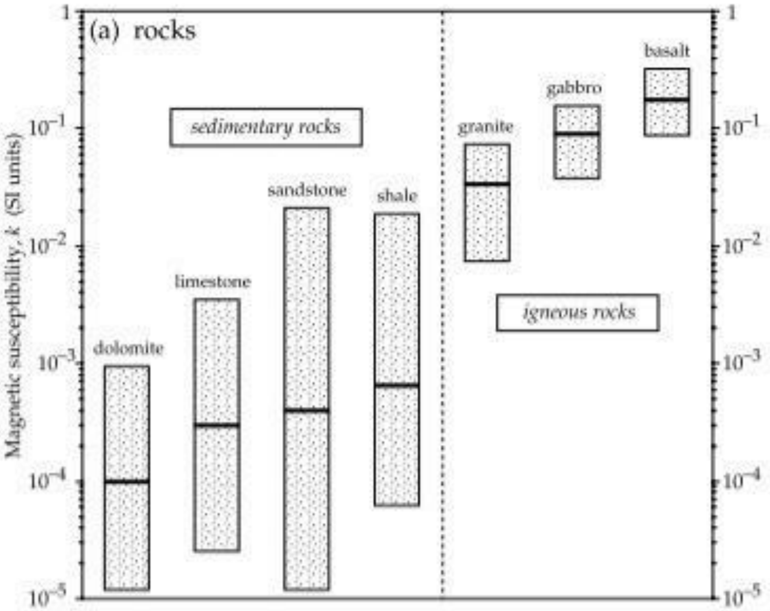

Figure 2. 1 Median susceptibility values and ranges of some common rock types (Lowrie, 2007)

Paramagnetism materials producing weak positive susceptibility when an external magnetic applied. The mineral in this class is clay minerals as illite and montmorillonite, biotite, pyrite, and siderite. In ferromagnetism material producing strong positive susceptibility. The magnetization that can exist in this class without an external magnetic field. Example of mineral in this class are hematite, Magnetite, pyrrhotite, maghemite, and goethite (see Table 2.1). As explained in Table 2.1 the minerals produce weak and strong magnetic susceptibility value. Mean that the response of rock magnetism depends on the type of rock contains in those rocks. Generally, igneous and metamorphic has high magnetic respond than sedimentary, due to sedimentary rocks mostly contains diamagnetism minerals (Figure 2.1). Quartz mineral from a mature source area have lower susceptibility and sediment sources from immature volcanic terrain have a high susceptibility. Fine-grained sedimentary rocks rich iron mineral, often associated with clays (Dentith and Mudge, 2014).

Table 2. 1 Susceptibility of mineral

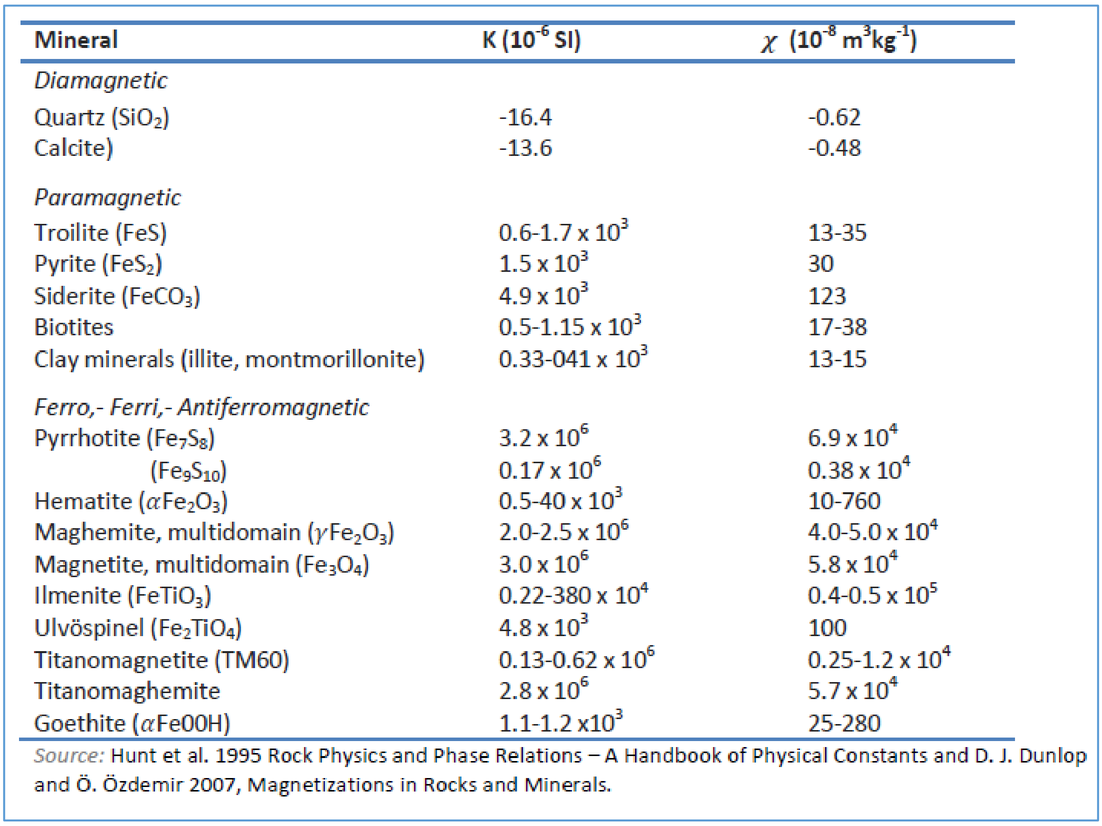

Mineral	K (10^{-6} SI)	χ (10^{-8} m^3kg^{-1})
Diamagnetic		
Quartz (SiO_2)	-16.4	-0.62
Calcite)	-13.6	-0.48
Paramagnetic		
Troilite (FeS)	$0.6\text{-}1.7 \times 10^3$	13-35
Pyrite (FeS_2)	1.5×10^3	30
Siderite ($FeCO_3$)	4.9×10^3	123
Biotites	$0.5\text{-}1.15 \times 10^3$	17-38
Clay minerals (illite, montmorillonite)	$0.33\text{-}041 \times 10^3$	13-15
Ferro,- Ferri,- Antiferromagnetic		
Pyrrhotite (Fe_7S_8)	3.2×10^6	6.9×10^4
(Fe_9S_{10})	0.17×10^6	0.38×10^4
Hematite (αFe_2O_3)	$0.5\text{-}40 \times 10^3$	10-760
Maghemite, multidomain (γFe_2O_3)	$2.0\text{-}2.5 \times 10^6$	$4.0\text{-}5.0 \times 10^4$
Magnetite, multidomain (Fe_3O_4)	3.0×10^6	5.8×10^4
Ilmenite ($FeTiO_3$)	$0.22\text{-}380 \times 10^4$	$0.4\text{-}0.5 \times 10^5$
Ulvöspinel (Fe_2TiO_4)	4.8×10^3	100
Titanomagnetite (TM60)	$0.13\text{-}0.62 \times 10^6$	$0.25\text{-}1.2 \times 10^4$
Titanomaghemite	2.8×10^6	5.7×10^4
Goethite ($\alpha Fe00H$)	$1.1\text{-}1.2 \times 10^3$	25-280

Source: Hunt et al. 1995 Rock Physics and Phase Relations – A Handbook of Physical Constants and D. J. Dunlop and Ö. Özdemir 2007, Magnetizations in Rocks and Minerals.

2.1.3 Analysis of Potential Field

The magnetic dataset is in RMI. In order to enhance magnetic anomaly, a number of filters applied to RMI data set. The enhancement performed in this work include the reduction to pole, first vertical and horizontal derivative, total horizontal derivative and 3D Euler Deconvolution. The main objective of reducing to pole is to migrate geomagnetic field from the measured inclination and declination of survey area as if it were at the pole. This filtering technique used to align the peaks and gradients of the magnetic anomalies directly over their sources. Reduce to pole data set used to obtain magnetic derivative anomalies. The result of first vertical and horizontal derivative aim to sharpen the edge of anomalies and enhance shallow feature. The 3D Euler Deconvolution was applied on the obtained reduce to pole from residual magnetic intensity data set. The Euler solutions used to analyze depth and geometry of sources anomaly in three dimensional model in the survey area. In this study the filtering technique such as reduce to pole, first vertical and horizontal derivative were generated in Oasis Montaj Software using the MAGMAP GX and Euler solutions using 3DEULER GX.

2.1.3.1 RTP

Each source body has positive and negative set on the magnetic anomaly map. The distance of both sets depends upon the depth, shape, dimensions of the source and inclination of the magnetic field. In the north pole, there is only positive centered over the body and negative centered over the body in the equator with small positive lobes on the northern and southern of the edges (Jain, 1988). The illustration of a magnetic anomaly in the equator in Figure 2.2a. At all other magnetic latitudes, the anomalies are asymmetric and do not correspond simply with the magnetic bodies. This makes it hard for the interpreter to delineate the boundaries of the bodies causing the anomalies. The solution is to reduce the total field anomaly to the north or south pole (Kearey *et al*, 2002). The illustration of a magnetic anomaly in the equator in Figure 2.2b. Macleod *et al* (1993) proposed simplest and most effective technique that addresses the amplitude problem is that developed by Grant and Dodds in the development of the MAGMAP FFT in GEOSOFT Ltd. The reduction to the pole operator can be given by:

$$\boldsymbol{L(\theta(=\frac{1}{[\sin(I)+i\cos(I)\cos(D-\theta)]^2})} \qquad \textbf{(Eq.2.2)}$$

Where θ is the wavenumber direction, *I* is the magnetic inclination, *D* is the magnetic declination. The formula showed that the I approaches 0 in the magnetic equator and magnetic equator and (D- θ) approaches $\pi/2$, the operator approaches infinity.

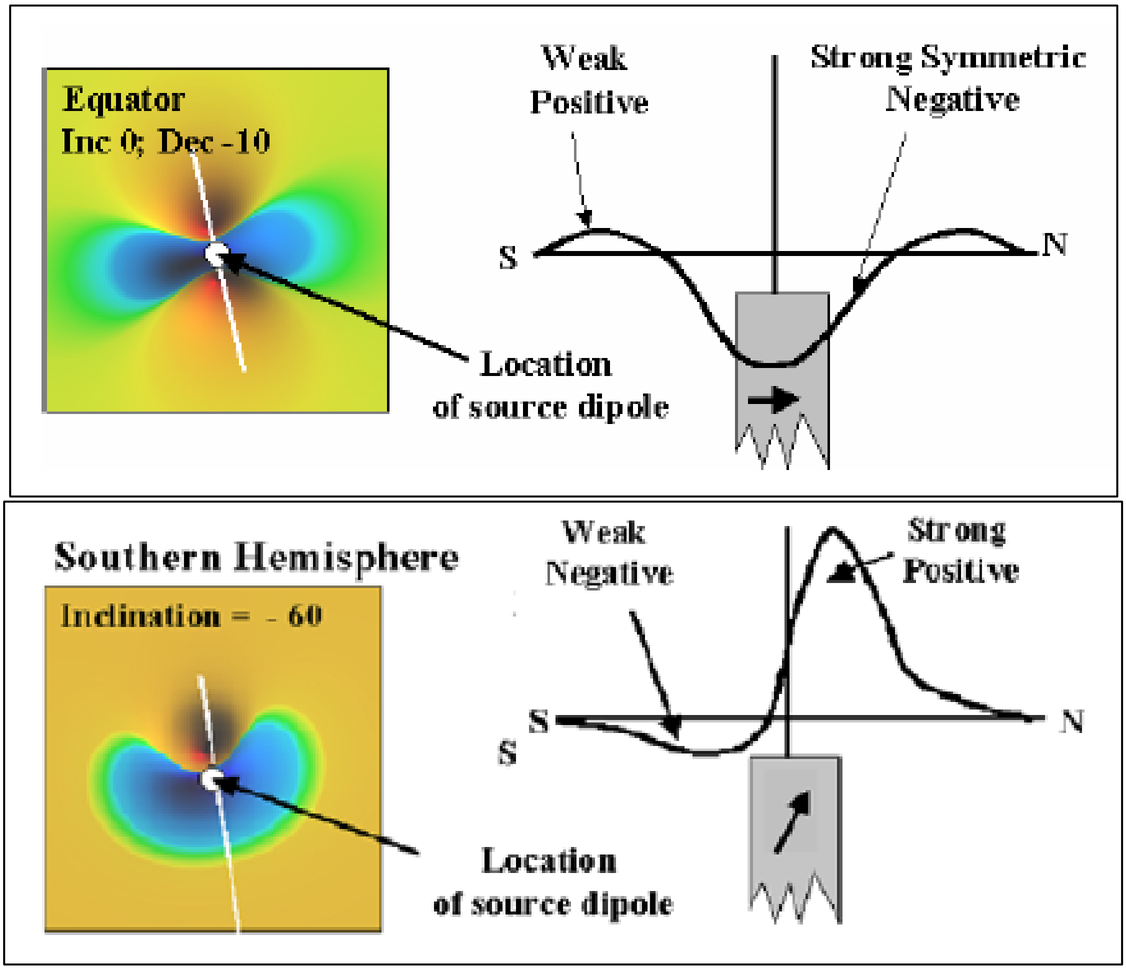

Figure 2. 2 Magnetic anomaly and profile. Magnetic anomaly at the Equator and profile for Declination –100 and Inclination 00 (a), Inclined field in the southern hemispheres and profile for Inclination -60 (b) (Fairhead, 2004)

2.1.3.2 Spectrum Analysis

A magnetic anomaly map comprising of different wavelength, various of wavelength in magnetic anomaly caused by magnetic sources at difference depths (Fairhead, 2004). One of the another method to analyze magnetic anomaly in difference depth is spectral analysis (Hinze *et al*, 2013). The FFT applied on the RTP aeromagnetic survey data to calculate the energy spectrum. The advantage this technique is averaging source depth over a region consist of complex pattern of magnetic anomalies. Spector and Grant (1970) introduced Power Spectrum can be used to identify average of source assemblages. This Power Spectrum is a 2D function of the energy and wave number. Spectral analysis of magnetic anomaly widely used FFT (Hinze *et al*, 2013). Commonly the result of 2D power spectrum plot natural log (*Ln* to base *e)* in Y axis and wavelength (wavenumber) in X axis as illustrated in Figure 2.3.

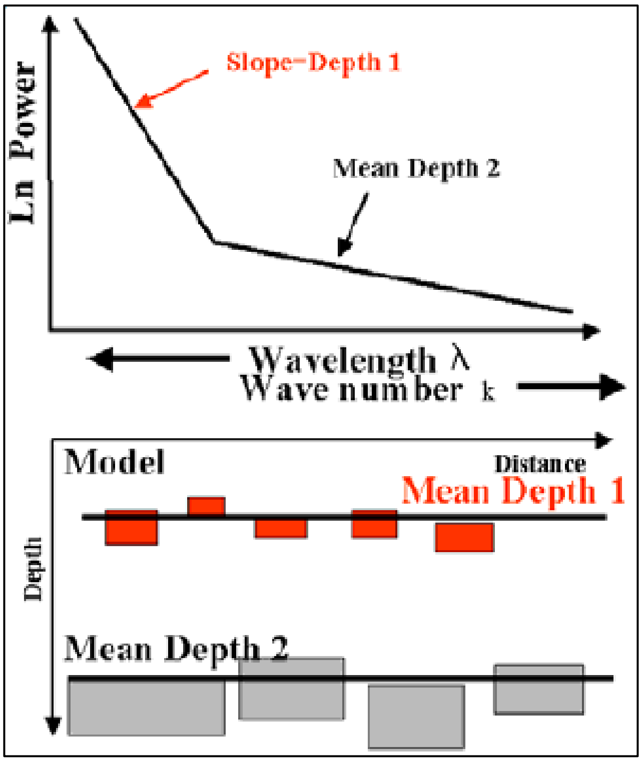

Figure 2. 3 2D power spectrum analysis (Fairhead, 2004)

Energy spectrum of magnetic classified into three segments such as: shallow source (high frequency), deep source (low frequency) and noise (Stella *et al*, 2015) as shown in Figure 2.3. Magnetic anomaly caused by shallow source are more dominated by short wavelength components and long wavelength components from deeper source (Kearey *et al*, 2002). Information of depth estimation value for designing to separate regional and residual field (Fairhead, 2004). By the change of spectrum curve can be used to estimate depth thickness of sediments in sedimentary basins (Telford *et al.,* 1990).

2.1.3.3 Directional Derivative

Delineating edges of magnetized structures is a common application of magnetic data to geological interpretation. Magnetic anomalies are always broader than the body causing them, this creates problems of anomaly interference between adjacent bodies resulting in delineating body outlines. Also an anomaly due to a deep, large body can mask a shallow, less magnetic body. The solution is to calculate anomaly derivatives of either the magnetic fields to isolate and/or separate these anomalies or aim to sharpen the edge of anomalies and enhance shallow feature (Fairhead, 2004).

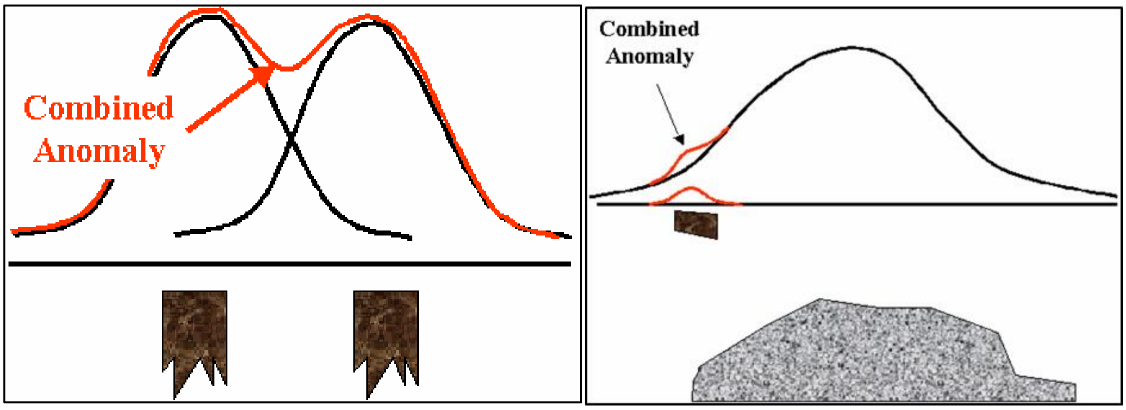

Figure 2. 4 Anomaly of magnetic data due to sources. Combined anomaly (a), Combination of small and large anomalies (b) (Fairhead, 2004).

There are various way used in derivative to help delineate edges and depths to structure. The first vertical and horizontal derivative are calculated using FFT (Gunn, 1975), they are routinely used to enhance details in magnetic data (Arisoy and Dikmen, 2013). Horizontal derivative filter responses calculate n^{th}-orde (derivation order) in the x and y direction and vertical derivative in z direction.

Commonly, the first horizontal derivative (1HD) are $\frac{\partial T}{\partial x}$ and $\frac{\partial T}{\partial y}$ **(Eq.2.3)**

Where *T* is magnetic field, so $\frac{\partial T}{\partial x}$ is horizontal derivative in *x* direction and $\frac{\partial T}{\partial y}$ is horizontal derivative in *y* direction.

The first vertical (1VD) is $\frac{\partial T}{\partial z}$ **(Eq.2.4)**

Where *T* is magnetic field in z direction.

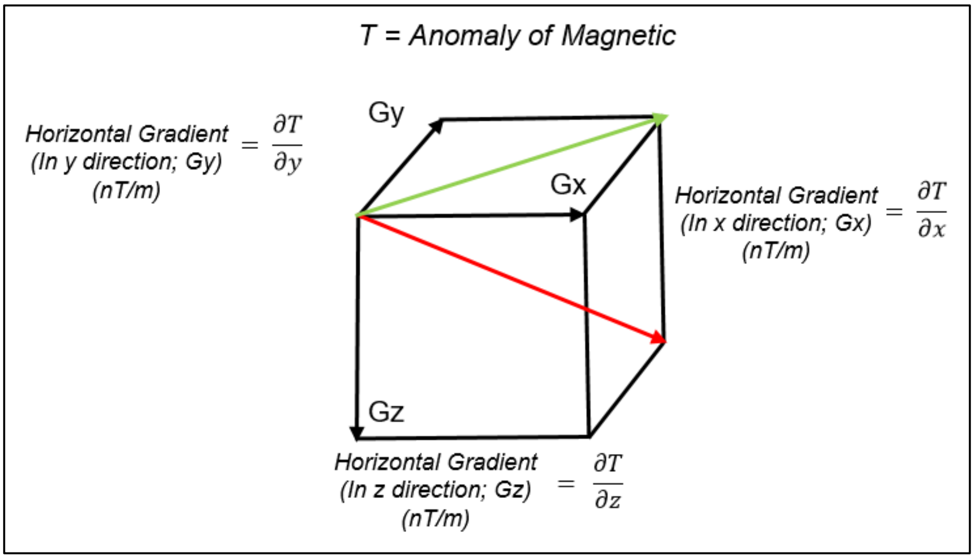

Figure 2. 5 Illustration of Directional derivative of magnetic anomaly (Castro et al, 2010)

Vertical derivatives of magnetic data used to enhance and sharpens geophysical anomalies (Komolafe *et al,* 2013). Vertical derivatives methods very important in magnetic data interpretation process. This filtering is powerful to enhance magnetic anomalies due to shallow source and the width of anomalies and also very effective to locate the source of source bodies (Cooper *et al,* 2004). Vertical derivative was done by applying low pass filters to remove high-wavelength, thereby enhancing low-wavelength component of the magnetic spectrum (Komolafe et al, 2013).

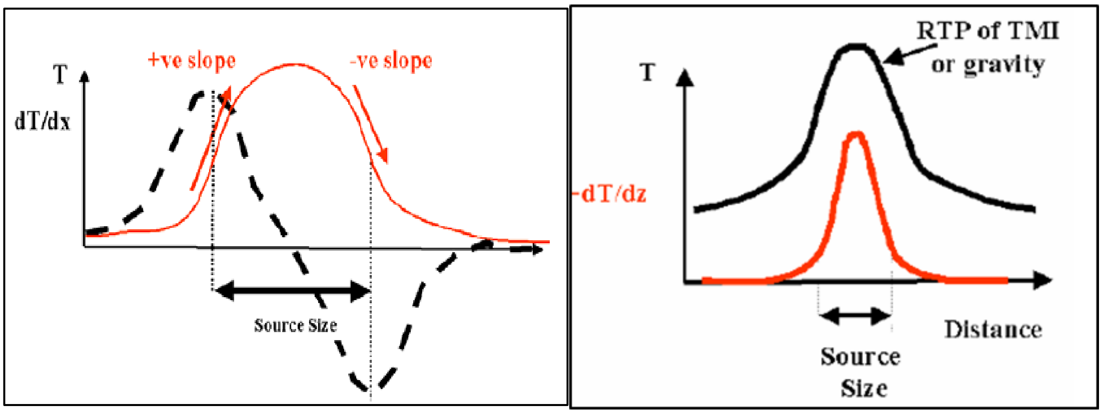

Figure 2. 6 Vertical derivative of magnetic anomaly (Fairhead, 2004)

2.1.3.4 Total Horizontal derivative

The combination of the two horizontal is used to define the horizontal positions of the density/magnetization contrasts. Blakely and Simpson (1986), proved that the combination of the two horizontal derivatives to be an effective tool for the boundary analysis and used to detect the edges of magnetized structures (Pilkington and Keating, 2004). Horizontal derivative of magnetic anomalies will give an indication of the boundary but due to the complexity of the anomaly will not made mapping of the edges of structures very easy. To make it easy the magnetic anomaly needs first to be transformed to Reduced To Pole (Fairhead, 2004). Total horizontal derivative is more effective in imaging shallower bodies than deeper one (Arisoy and Dikmen, 2013). Cordell and Grauch (1984a) gave formula used to detect the total horizontal derivative as follow:

$$THDR = \sqrt{\left(\frac{\partial T}{\partial x}\right)^2 + \left(\frac{\partial T}{\partial y}\right)^2} \qquad \textbf{(Eq.2.5)}$$

Where T is magnetic field, $\frac{\partial T}{\partial x}$ and $\frac{\partial T}{\partial y}$ are the two orthogonal horizontal derivative of T (magnetic field).

2.1.3.5 Euler Deconvolution

Euler deconvolution is a tools to interpret potential field (magnetic and gravity) for locating anomalous source and their depth. This technique proposed by Thompson (1982) for determine the depth and locating anomaly source. Reid *et al* (1990) applied this technique developed the special case for magnetic field. This method based on anomaly gradients for selected source geometry and is sequentially applied to all the points along the anomaly profile. It is represents the strength of magnetic field at a measurements point (Dentith amd Mudge, 2014). Thompson's technique widely applied to magnetic and gravity data. Thompson (1982) showed Euler's homogeneity could be written by

$$\boldsymbol{\frac{\partial T}{\partial x}(x - xn) + \frac{\partial T}{\partial y}(y - yn) + \frac{\partial T}{\partial z}(z - zn) = N(B - T)} \qquad \textbf{(Eq.2.6)}$$

where $x, y\ and\ z$ coordinates of observation point, T is the observed field measured in $x, y\ and\ z$, n is degree of homogeneity, N is structural index and B is regional value of total field. Variation of depth estimation (z) depend on the value of structural index (N), where if N is too low caused the depth estimation will be too shallow and N is too high the depth estimation will be overestimated (Dentith amd Mudge, 2014). Dentith and Mudge (2014) recommended affective value of N between 0-3. Calculating Euler deconvolution doing after obtained : RMI reduced to pole, horizontal and vertical gradients of magnetic field, window size and structural index. The window size of the deconvolution must be at least twice of line spacing or observed grid spacing and more than half the depth of target (Reid *et al,* 2013). The advantage of Euler solutions are useful to analyze depth and geometry of sources, in three-dimensional it is presented different source depth and geometry distinguish using variations colours/symbols in the map (Dentith amd Mudge, 2014). Euler deconvolution produces more rigorous depth estimates than other methods, but it is considerably more difficult to implement. Aeromagnetic anomaly in the English Midlands contstructed the geological interpretation based on Euler deconvolution using variuos structural index (N) from 0.0, 0.5 and 0.6. (Kearey *et al,*2002).

2.2 Electromagnetic Method

2.2.1 Basic Physics Frequency Domain of EM

All electromagnetic phenomen governed by Maxwell's equation. This equation can be derive the electromagnetic wave in time and frequency domain. The frequency domain based on Maxwell's equation such as follows:

$$\nabla \, x \, \boldsymbol{E} = -\frac{\partial \boldsymbol{B}}{\partial \boldsymbol{t}} \qquad \textbf{(Eq.2.7)}$$

$$\nabla \, x \, \boldsymbol{H} = \boldsymbol{J} + \frac{\partial \boldsymbol{D}}{\partial \boldsymbol{t}} \qquad \textbf{(Eq.2.8)}$$

$$\nabla . \boldsymbol{D} = \boldsymbol{\rho} \qquad \textbf{(Eq.2.9)}$$

where **E** (electric field intensity, V/m), **B** (magnetic flux densities/magnetic induction, Wb/m2 or Tesla), **D** (dielectric displacement, C/m2), **H** (magnetic field intensity, A/m) and **J** (electric current density, A/m2). Eqs. 2.1 and 2.3 are uncoupled differential equations of the five vector such as E B D H and J. These equations are coupled through frequency domain (Grant and West, 1965).

$$\boldsymbol{D} = \boldsymbol{\varepsilon}^* \, (\boldsymbol{\omega}, \boldsymbol{E}, \boldsymbol{r}, \boldsymbol{t}, \boldsymbol{T}, \boldsymbol{P}, \dots). \boldsymbol{E} \qquad \textbf{(Eq.2.10)}$$

$$\boldsymbol{B} = \boldsymbol{\mu}^* (\boldsymbol{\omega}, \boldsymbol{E}, \boldsymbol{r}, \boldsymbol{t}, \boldsymbol{T}, \boldsymbol{P}, \dots). \boldsymbol{H} \qquad \textbf{(Eq.2.11)}$$

$$\boldsymbol{J} = \boldsymbol{\sigma}^* \, (\boldsymbol{\omega}, \boldsymbol{E}, \boldsymbol{r}, \boldsymbol{t}, \boldsymbol{T}, \boldsymbol{P}, \dots). \boldsymbol{E} \qquad \textbf{(Eq.2.12)}$$

ε^* (dielectric permitivity,F/m), μ^* (manetic permeability,H/m), σ^* (electric conductivity, S/m), ω (angular frequency), r (position), T(temperature), t (time) and P (presure). Eqs 2.10- 2.12 are complex in general case, the phase of D and E, of H and B, and of J and E to be different. In electromagnetic earth problem, assume all media are linear, isotropic, homogeneous and electrical properties indepedent of time, temperatur and presure. The magnetic permeability assumed free space ($\mu = \mu_0$).

$$\boldsymbol{D} = \boldsymbol{\varepsilon E} \qquad \textbf{(Eq.2.13)}$$

$$\boldsymbol{J} = \boldsymbol{\sigma E} \qquad \textbf{(Eq.2.14)}$$

$$\boldsymbol{B} = \boldsymbol{\mu H} \qquad \textbf{(Eq.2.15)}$$

The Fourier Transform of Eqs.2.7 and 2.8 , and utilize the constitutive of Eqs 2.13, 2.14 and 2.15 to obtain Maxwell's equation in electromagnetic frequency domain. As showed in Eq. 2.16 and 2.17 (Ward anf Hohmann,1988).

$$\nabla x E + i\mu\omega H = 0 \qquad \textbf{(Eq.2.16)}$$

$$\nabla x H - (\sigma + i\mu\omega)E = 0 \qquad \textbf{(Eq.2.17)}$$

The electromagnetic in geophysics methods described by Maxwell's equations mendtioned above. The current flowing through the transmitter coils and produces a magnetic field that varies in time called the primary field. This field, according to Maxwell's equations, induces an electrical current in the conductive ground. These induced currents, with the associated electrical field, generate in turn a magnetic field, the secondary field, measurable with a receiver coil. At the receiver coil, a total field, that is the sum of the primary and the secondary is measured. This is valid for the electromagnetic method in the frequency domain. In this chapter will focuse on frequency domain electromagnetic.

2.2.2 FDEM Method: Principle and Measuring Procedure

The sources (Tx) has electromagnetic energy involve electrical currents that will inject into the earth or flow in a wire-loop. The input signals injected to the earth can be harmonic or transient and its propagation through the earth are in FDEM and TDEM. The electromagnetic field generated by source usually called a primary electromagnetic field (see Figure 2.7). As the primary magnetic field is very close to a dipole field at some distance from the transmitter coil, it can be regarded as a field of a magnetic dipole sitting in the center of the transmitter coil and having an axis perpendicular to the area of the coil. The oscillating primary magnetic field induces eddy currents in the subsurface. The induction of eddy currents in the subsurface depends upon the physical properties and its environment. These currents, in turn, generate the secondary magnetic field which is dependent on the underground conductivity distribution. The secondary magnetic field is picked up by the receiver coil (Rx) and related to the primary magnetic field expected at the center of the receiver coil (Figure 2.7). As the secondary field is very small with respect to the primary field, the primary field is generally bucked out and the relative secondary field is measured in parts per million (ppm) (Kirsch, 2009).

Due to the induction process in the underground, there is a small phase shift between the primary and secondary field, i.e., the relative secondary magnetic field is a complex quantity having in-phase (R) and quadrature (Q) components (Kirsch, 2009). The orientation of the transmitter coil is horizontal or vertical and the receiver coil is oriented in a maximum coupled position, resulting in horizontal coplanar, vertical coplanar or vertical coaxial coil systems.

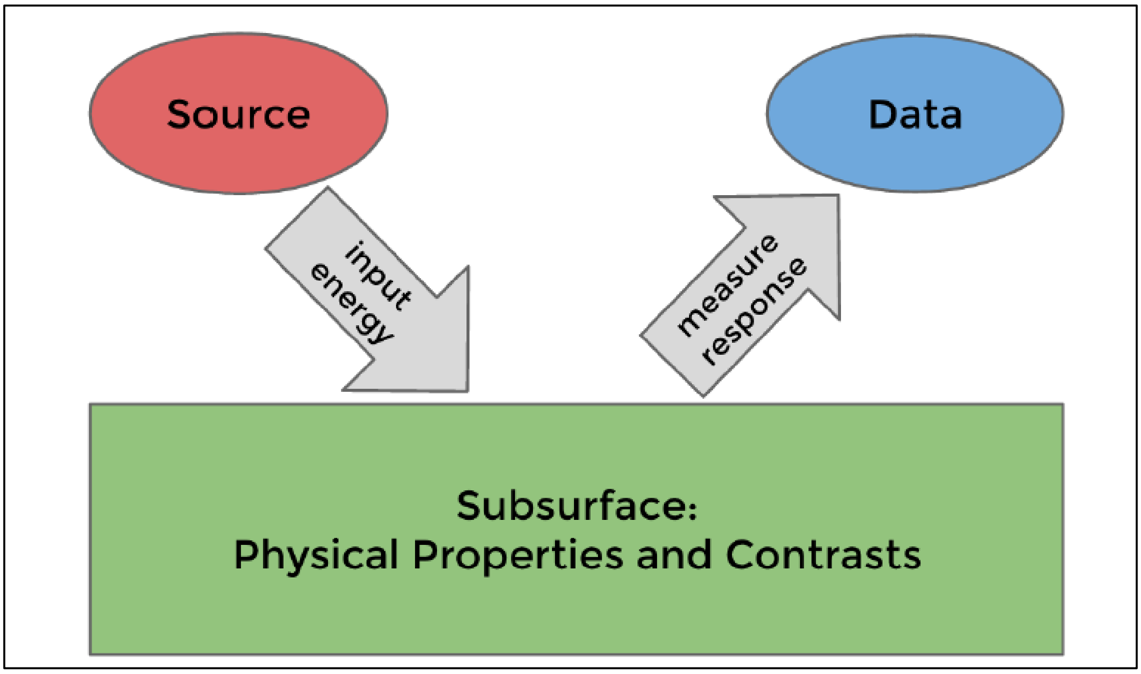

Figure 2. 7 Sources provide energy to excite the earth. Responses depend upon the physical properties and contrasts in the subsurface and measure responses at the surface generate data

Solving the induction equation with respect to a horizontal coplanar-coil system (Siemon, 2009). The complex secondary magnetic field recorded in the sensor give the information about the physical properties. Although the data contain information about the subsurface, subsequent processing, and inversion to reduce the noise and to generate the physical property distribution in the subsurface. The distribution of physical properties in the subsurface used to extract meaningful information.

The homogeneous induction of secondary magnetic field vector F in the earth for the electromagnetic filed vector solved by Maxwell's equation as given (Siemon,2009).

$$\boldsymbol{Z}\left(\frac{\boldsymbol{z_s}}{\boldsymbol{z_p}} = (\boldsymbol{Ri} + \boldsymbol{Q})\right) \qquad \textbf{(Eq.2.18)}$$

where Z is complex and normalized secondary magnetic field, *Z*s is complex secondary field, *Z*p is primary field, R is inphase/real components of Z, Q is out of phase/quadrature/imaginer components of Z and $i = \sqrt{-1}$ is imaginer unit.

For a horizontal-coplanar, vertical-coplanar and vertical-coaxial pair with a coil separation r and at an altitude h above the surface, the relative secondary magnetic field Z is given (Arab-Amiri *et al,* 2010).

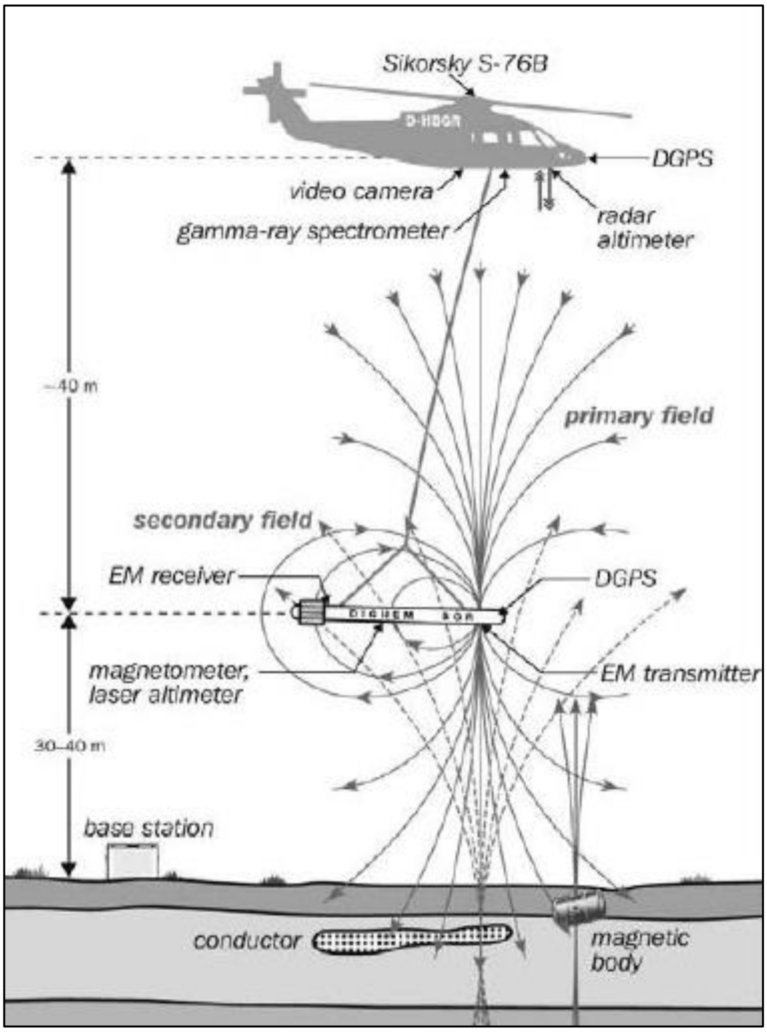

Figure 2. 8 Helicopter-borne geophysical system: Electromagnetic, magnetic, GPS and laser altimeter sensors are housed in a bird (Arab-Amiri et al, 2010)

Equation 2.18 valid for horizontal-coplanar

$$\boldsymbol{Z = r^3 \int_0^\infty R_1\left(f, \lambda, \rho(z)\right)\lambda^2 e^{-2\lambda h} J_0(\lambda r) d\lambda} \qquad \textbf{(Eq.2.19)}$$

Equation 2.19 is valid for vertical-coplanar

$$\boldsymbol{Y = r^2 \int_0^\infty R_1\left(f, \lambda, \rho(z)\right)\lambda^2 e^{-2\lambda h} J_1(\lambda r) d\lambda} \qquad \textbf{(Eq.2.20)}$$

And equation 2.14 for vertical-coaxial

$$\boldsymbol{X = r^2 \int_0^\infty R_1\left(f, \lambda, \rho(z)\right)\lambda^2 e^{-2\lambda h \frac{J1\,(\lambda r) - \lambda J_0(\lambda r)}{2}} dt} \qquad \textbf{(Eq.2.21)}$$

where r is the horizontal distance between transmitter and receiver coils, R_1 is reflection factor containing the underground vertical resistivity distribution ρ(z) with z pointing downwards, h is sensor height above ground, and λ is wave number. J_0 and J_1 are Bessel functions of first kind and zero or first order, respectively and can be approximated as follows (Arab-Amiri *et al,* 2010):

$$\boldsymbol{J_0(x) \cong 1 - \frac{x^2}{4} + \frac{x^2}{4} - \cdots}$$
$$\boldsymbol{J_1(x) \cong \frac{x}{2} - \frac{x^3}{16} + \frac{x^5}{384} - \cdots} \qquad \textbf{(Eq.2.22)}$$

The horizontal secondary electromagnetic field perpendicular and along the transmitter and receiver direction as long as the r < 0.3 h. The secondary field perpendicular at Y direction showed in Eq.2.20 and along the X direction as showed in Eq.2.21 (Mundry 1984). Eq.2.19, 2.20 and 2.21 are complex integral, they can be evaluated numerically using Hankel transform. To approximate the Bessel function J0 by the first term of Eq.2.22, the coil separation has to be sufficiently smaller than the sensor altitude. The reflection factor for a homogeneous half-space model can be derived from Eq.2.19. For a homogeneous half-space, R0 is defined as:

$$\boldsymbol{R_0 = \frac{\lambda - v}{\lambda + v}, \quad v = \sqrt{\lambda^2 + \frac{2i}{p^2}}, \ p = \sqrt{\frac{2\rho}{\omega\mu_0}}, \delta = \frac{h}{p}} \qquad \textbf{(Eq. 2.23)}$$

Where p is the skin depth, ρ is the resistivity of the half-space, and μ0=4π×10−7 Vs/Am is the magnetic permeability of free space. The penetration of the electromagnetic field into the earth depends on both the system frequencies used and the resistivity distribution in the subsurface.

Where secondary field transformation depends only on the ratio $\boldsymbol{\delta} = \frac{h}{p}$, Figure 2.9 shows the complex function Z. This Figure consisting of Real and Quadrature component of Z and also amplitude and its ratio. In transformation process requires at least two curves to perform the transformation of secondary field.

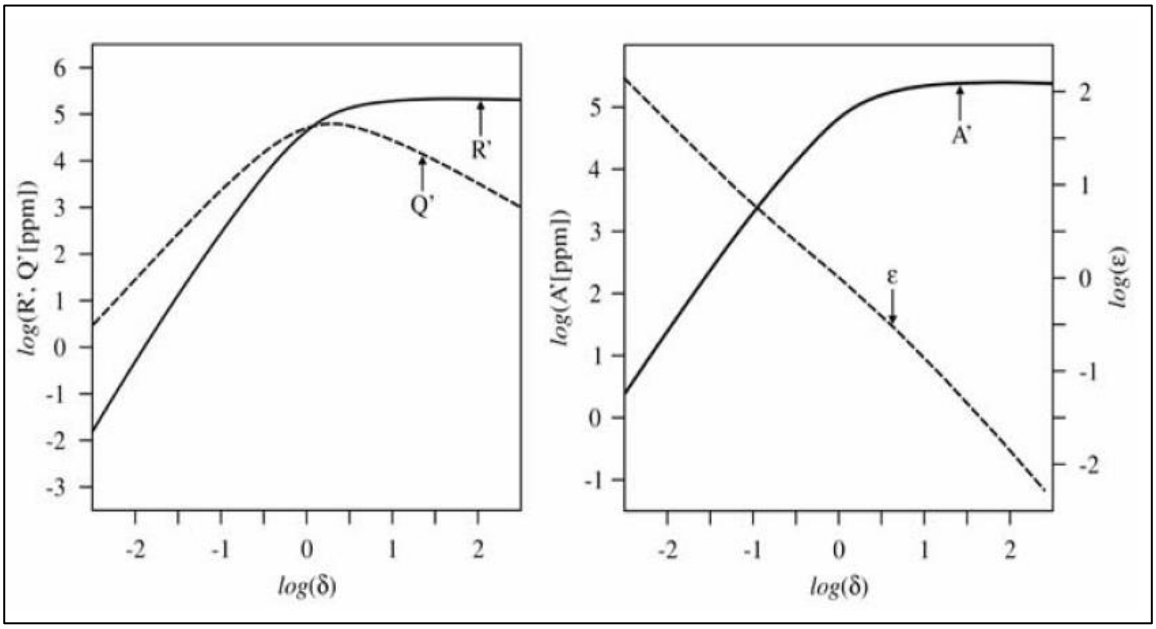

Figure 2. 9 The transformed secondary field Z for arbitrary half-space resistivity R and Q (left), Amplitude (A) and phase ratio (ε) (right) on log-log scale (Kirsch, 2009)

2.2.3 Electrical Properties of Rocks

Several near surface conditions can affect the response measured by from abrupt changes in the topography and weathering of entire geological provinces, to internal porosity, mineral composition and fluid saturation levels of the underlying materials. Most constituents of fresh rocks are fundamentally electrical insulators (resistors), whilst salt water, clays and massive sulphides are electrical conductors (Ley-Cooper and Davis, 2015a). Rock resistivity variation depends on another parameter of rock itself. Those parameters such as: porosity, fluid content (oil, gas and water). Igneous and metamorphic rocks typically have high resistivity values (see Table 2.2). The resistivity of these rocks is greatly dependent on the degree of fracturing, and the percentage of the fractures filled with ground water (Loke, 2004). Sedimentary rock with high porosity occupied by fluid has lower resistivity than another compact sedimentary rock with most values below 1000 Ω·m. unconsolidated sediment rock generally low resistivity values than sediment rock. Groundwater with varies resistivity value, it is depending on the concentration of dissolved salts. Generally, the range of its resistivity value varies from 10 to 100 Ω·m. And low resistivity < 0.2 Ω·m is sea water due to the relatively high salt content (see Table 2.2).

Table 2. 2 Resistivity of rocks

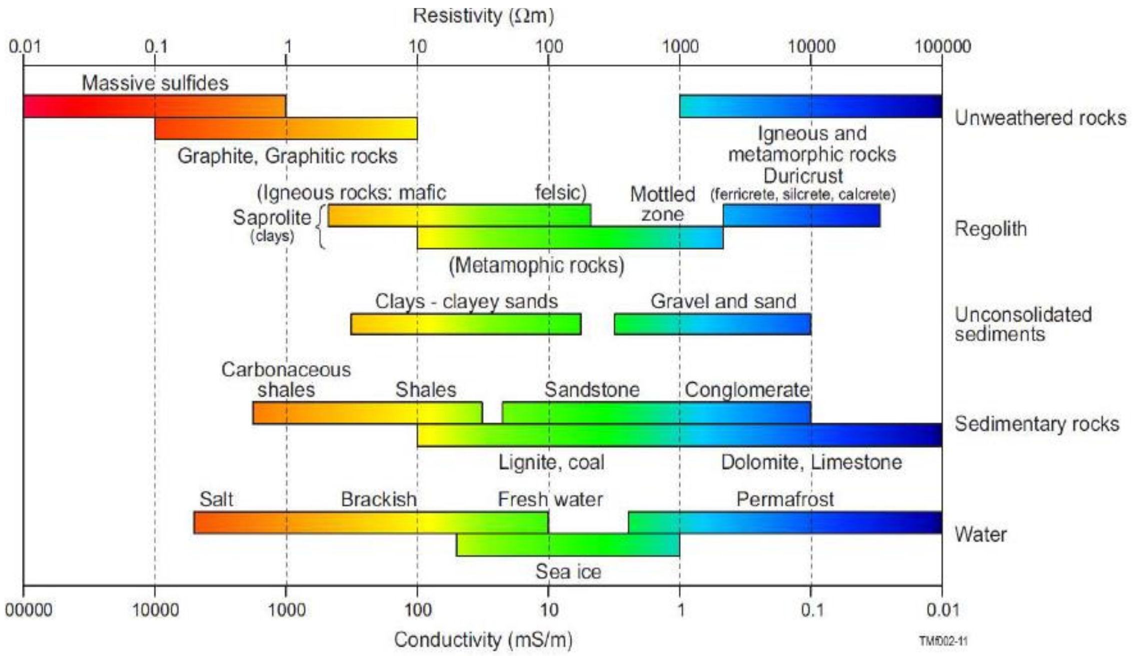

2.2.4 AEM Data Processing

The secondary electromagnetic to be composed of inphase (R) and quadrature (Q) components that measured the induced voltages of the secondary magnetic fields by the receivers. Normally, during the acquisition R and Q component of electromagnetic converted the data from millivolt to parts per million (ppm) (Valleau, 2000) with respect to the primary fields. Before doing inversion of secondary magnetic field, applied the standard data processing such as zero leveling, data correction (disturbances by external field e. g power lines) and low-pass filtering reducing the noise. Flight altitudes of several hundred meters (e.g. 350 m for a common HEM system) are sufficient to drop down the signal of the secondary field below the system noise level. This effect used for determining the zero levels of the HEM data. Remaining signals due to insufficiently bucked out primary fields, coupling effects with the helicopter, or (thermal) system drift are generally detected at high flight altitude several times during a survey flight. These basic values measured at reference points are used to shift the HEM data with respects to their zero levels (Kirsch, 2009).

Another noise also be can recorded on the sensor are nor response of geology such as radio transmitters or power lines must remove from the data by applying appropriate filtering. There are two main type of external fields (non-geological noise) are observed individual spike and lower amplitude, higher frequency noise. To enhance the quality of inversion, if spikes present in data must be removed first. The spike noise can be removed by manually or with a nonlinear or spike removal filter. To remove high frequency noise (leaving only geological wavelength) can be applied a lower-pass filter (Valleau, 2000). Induction effects from buildings and other electrical installations or effects from strongly magnetized underground sources should not be erased from the data during the first step of data processing. These effects appear particularly on a low-frequency resistivity map as conductive or resistive features outlining the locations of man-made installations or strongly magnetized sources, respectively. If necessary, these effects can be cancelled out after a thorough inspection, and the data may be interpolated in case of small data gaps and smoothly varying resistivities (Siemon, 2009).

2.2.5 Inversion of AEM

Commonly the real and quadrature component of secondary field inverted into resistivity using two principal model is a homogeneous half-space inversion and layered half space inversion (see Figure 2.10). The homogeneous half-space inversion uses single frequency and the inversion is done individually for each of the frequencies. While layered half space inversion (1D) uses all frequencies available in the data. The result of half-space inversion is the apparent resistivity, where the apparent resistivity inverse of the apparent conductivity. The component (R and Q) of secondary filed can be used to calculate the apparent resistivity if the distance between transmitter-receiver and the top of the half-space is known. The inversion of secondary field, in combination with the in-phase component R, with the quadrature component Q, with the amplitude and phase ratio. Amplitude refers to the square root of the sum of the squares of the in-phase and quadrature components.

$$\boldsymbol{A} = [\boldsymbol{Z}] = \sqrt{\boldsymbol{R}^2 + \boldsymbol{Q}^2}\ , \quad \boldsymbol{\varepsilon} = \frac{\boldsymbol{Q}}{\boldsymbol{R}} \qquad \textbf{(Eq.2.24)}$$

The secondary field on the half-space resistivity is highly non-linear (Eq.2.24), thus the inversion is not straightforward and the apparent resistivities have to be derived by the use of look-up tables, curve fitting or iterative inversion procedures. the disadvantage of single-component inversion is R component is very small for low frequencies and high resistivities ($\delta < 0.1$) or low induction mode, and also nearly constant for high frequencies and low resistivities ($\delta > 10$) or strong induction mode, and the quadrature component Q’ is not unique.

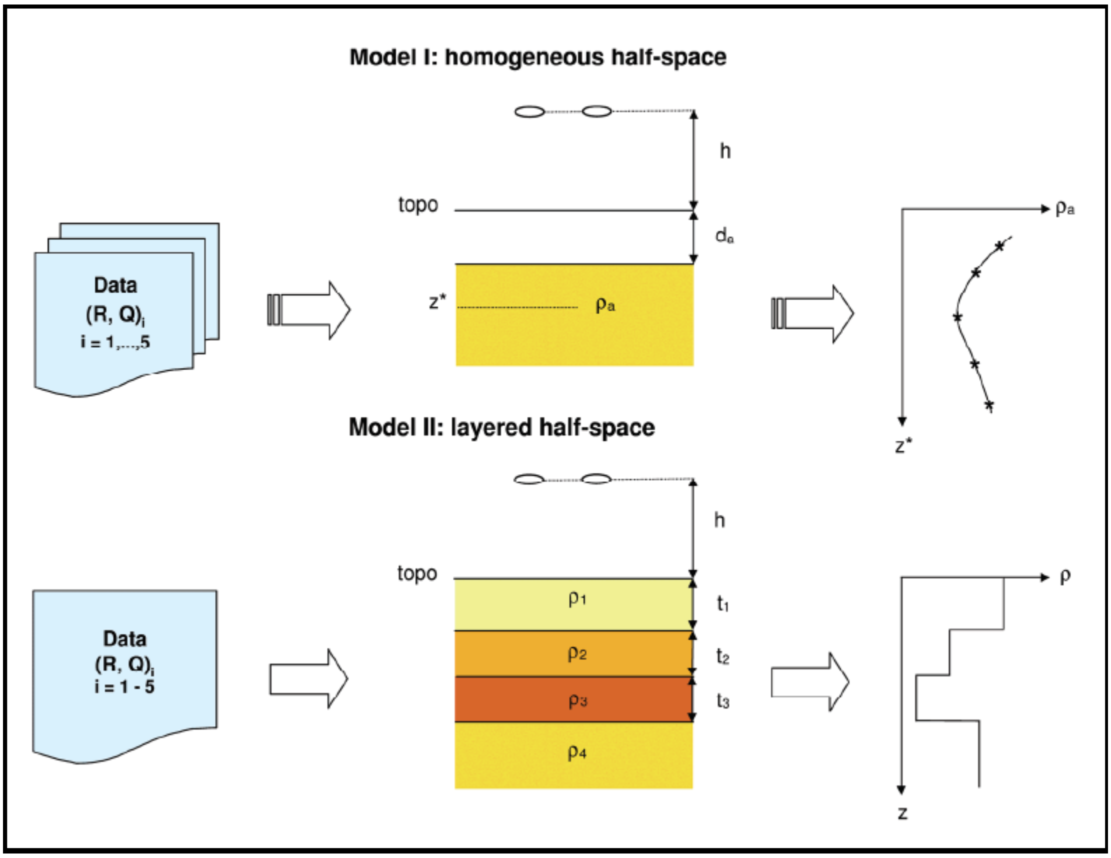

Figure 2. 10 Airborne electromagnetic data inversion. Homogeneous half-space model (model I) and layered half-space model (model II) (Siemon,_) (https://www.liag-hannover.de/fileadmin/user_upload/dokumente/grundwassersysteme/burval/buch/089-098.pdf)

Airborne electromagnetic multi-frequency has sensor height (h) and R and Q component of the secondary field. Therefore, apparent resistivity (ρa) can be obtained by using two of these three measured parameters (Fraser,1978). As the real, R, the response is very small for great penetration depths and that the quadrature response, Q, peaks at an intermediate depth, thus it is not recommended to use the real or quadrature response alone for obtaining the apparent resistivity together with the available sensor altitude (Arab-Amiri *et al,* 2010). The altitude measured in the field by laser or radar altimeters. The altitude measures in the laser or radar altimeters may be affected by the tress and building (Figure 2.10).

Sensor altitudes as an input parameter in inversion process will give the crucial disadvantage. To avoid these disadvantages in calculating apparent resistivity (from R, Q, amplitude, and ratio) and apparent distance of the sensor from the top of the conducting half-space only used the component of secondary field (Siemon, 2009). Over a homogeneous half-space ground, the calculated sensor altitude equals the measured sensor height h. For an inhomogeneous layered half-space, however, the apparent resistivity is an approximation to the true resistivity of the ground (Arab-Amiri *et al,* 2010).

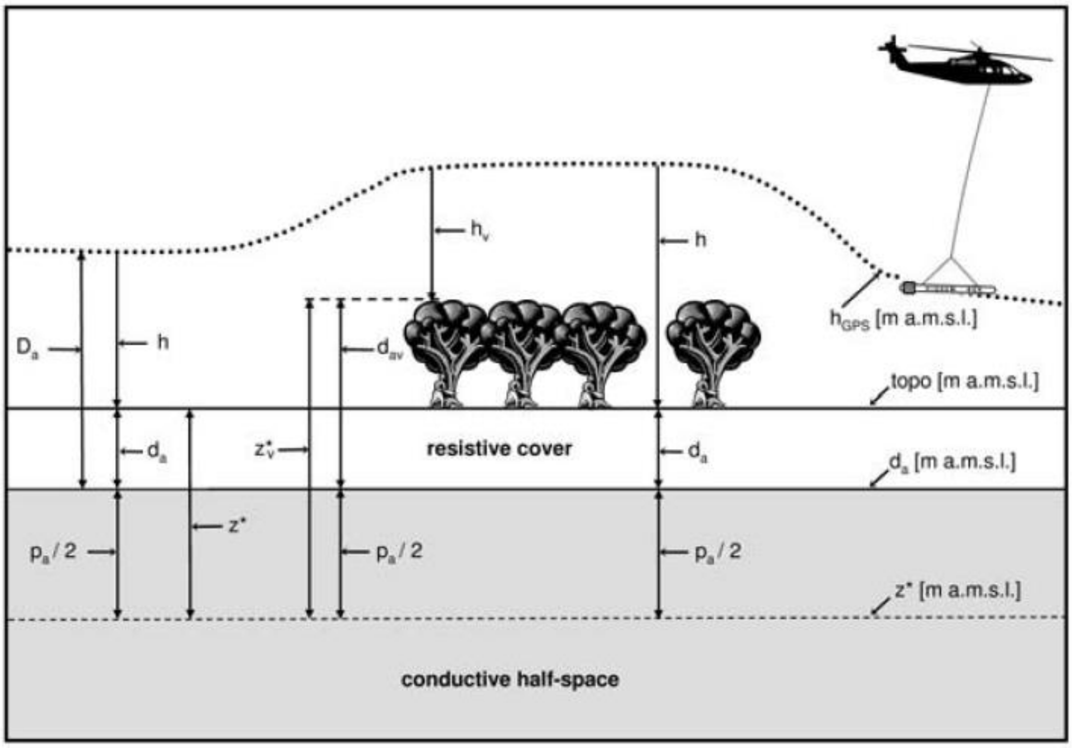

Figure 2. 11 Graphical display of apparent distance, apparent depth, centroid depth, sensor altitude h, sensor elevation h GPS and topographic elevation topo (Siemon_) (https://www.liag-hannover.de/fileadmin/user_upload/dokumente/grundwassersysteme/burval/buch/089-098.pdf)

As showed in Figure 3.5, the difference between Da and h called apparent depth (d_a). The Da (apparent distance as in Eq.2.25) can be greater h (measured sensor altitude in the field). d_a is positive in case of a resistive cover (including air) as it is the case in Figure 3.5 otherwise a conductive cover exists above a more resistive substratum (Siemon,2009).

$$\boldsymbol{d_a = D_a - h} \qquad \textbf{(Eq.2.25)}$$

From the apparent resistivity and apparent depth can be derive to obtain the centroid depth as given

$$\boldsymbol{Z^* = d_a + \frac{p_a}{2}} \text{ with } \boldsymbol{p_{a=}505{,}3\sqrt{\frac{\rho_a}{f}}} \qquad \textbf{(Eq.2.26)}$$

The centroid depth which is a measure of the mean penetration of the induced underground currents (Siemon, 2001). . Each set of half-space parameters is obtained individually at each of the HEM frequencies and at each of the sampling points of a flight line.

Chapter 3. Geomorphology, Geology and Hydrogeology of Study Area

3.1 Geography and Administrative

The study area is located at Baucau municipality of Timor-Leste. Baucau municipality situated in the northern coast of Timor Leste, administratively in the eastern of Manatuto municipality and western of Lautem municipality. To the northern part is Wetar Strait and the southern part is Viqueque municipality. This study was focused on Baucau plateau includes the western and eastern escarpment and also the northern part. Mostly, major springs emerge in the west an east escarpment and also some are in the north-east part of Baucau plateau. The airborne geophysical survey just covered entire the Baucau plateau, where it is covered all Baucau plateau and the coverage of geophysics airborne consisted of 811.24 km2. The coordinates of the corner points of the survey block are : (1) 205484 & 9057285, (2) 214498 & 9067416, (3) 219118 & 9063314, (4) 219146 & 9060593, (5) 220259 & 9059620, (6) 209513 & 9047504, (7) 205807 and 9050594 and (8) 204698 & 9053938. Those corner coordinates in WGS84 UTM zone 52.

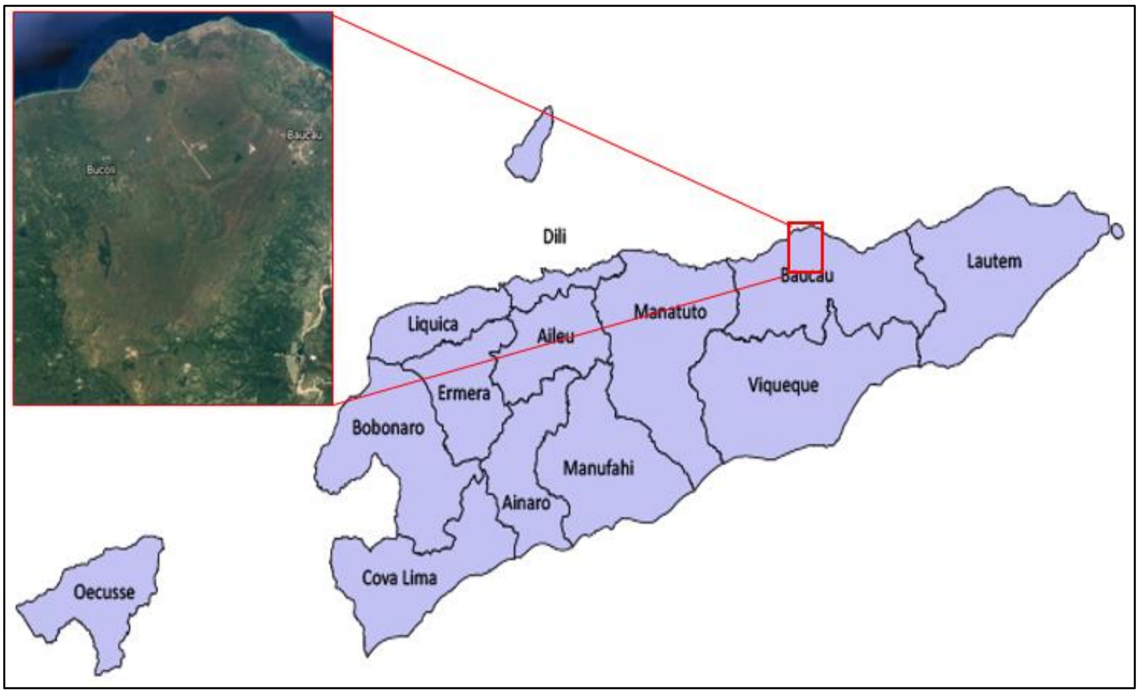

Figure 3. 1 Location research area

Source: https://www.mof.gov.tl/about-the-ministry/statistics-indicators/sensus-fo-fila-fali/download-suco-reports/?lang=en

3.2 Geomorphology

Mentzner (1977), classified physiography unit based on morphological characteristic as well as based on the altitude. The classification as in Figure 3.2. Where Baucau plateau (III) as an uplifted coral reef rising through a series of high terraced cliffs from sea level to 500 m and continues to rise gradually to over 700 m (Loilubu area) southwest of the Plateau. Around the airport, the surface is rough and pitted caused by numerous solution cavities and residual low coral ridges because of weathering of underlying coral limestone. Baucau plateau forms a big triangle with its apex to the Venilale area, in the north part its abuts against marine terrace, west and east are escarpments.

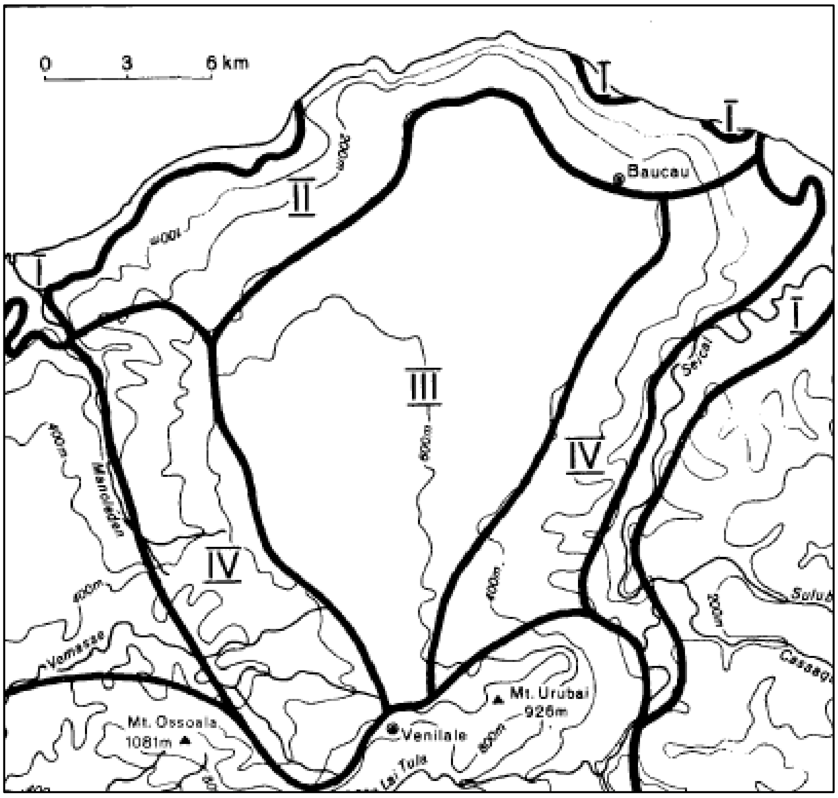

Figure 3. 2 Geomorphology of Baucau platau and surrounding area (Mentzner 1977)

In the east and west part of Baucau Plateau, the Plateau flanked by two escarpments. Both escarpments called east and west escarpment (IV). The escarpments drop from the top of the plateau down to the alluvial plain of the River Manoleden in the west and Rive Seical in the East. The morphology of the escarpment controlled by the underlying geological material. Where the coral limestone of the plateau is underlain by a layer of Viqueque formation. The other coral limestone as rest upon Bobonaro scaly clay is also reflected in the escarpment. Numerous natural springs can be found in the harder less sedimentaries from Viqueque formation such as claystones, marls, siltstone, and sandstone. The Viqueque formation reaches from 300 to 400 m down to the floodplain of the Seical River at around 50-100 m and less extensive in the western escarpment, where it covers a belt between 400 to 700 m near Loilubu village. Marine Terraces zone (II) consisting of a series of up to twelve upheaved Pleistocene marine terraces which rise abruptly from the sea in a step-like fashion. These terraces of up 100 m high cliffs which at their base are often undermined by wave-cut notches and which alternate with over 100 m wide abrasion platforms. These terraces tend to be correlated with successive shifts of the sea level due to the epeirogenetic uplift of Timor and to a lesser degree to the phases of glaciation in these latitudes. Two major springs (Uai Leo and Uai Lia) emerge from the ground at the present site of Baucau village which is located on a platform at about 300 m above sea level. Coastal Zone (I) is made up of the alluvial material of the Post-Pliocene Suai Formation. It is characterized by one or two sandy beach ridges, quite in contrast to the south coast. Large quantities of silt are washed down the slopes and deposited behind these beach ridges on account of the proximity of the mountains.

3.3 Rainfall of Timor Leste and Study Area

Due to its topographic relief and geographical location, Wallace *et al* (2012) divided seasons in Timor Leste to be: Wet season from December to May dry season from June to November. The temperature in Timor Leste is varies depending on the topography. Generally temperature decrease due to increase in elevation. In the coastal area the temperature about 270 C and decrease to the 220 C in the high land. The annual rainfall range in Timor-Leste from 800 mm-2800 mm. In the north coast the rainfall range from 800 mm, in the central highlands 1500-2000 mm and in the higher altitude region the rainfall range over 2800 mm such as in Matebian range in the east and Ramelau and Kablaki in the west part (Figure 3.3C).

The rainfall at Buacau region almost occurs from December to February, gradually decrease to the September (Figure 3.3B). The rainfall increase to the southern and decrease to the coastal area (north), due to the elevation of Baucau plateau increase to the south and decrease to the coastal area (Figure 3.3A). The monthly maximum and minimum temperature at Baucau plateau decrease from May to October and increase on November to Abril, with the minimum temperature is about 20^0C and the maximum value about 32^0C (Figure 3.3B). In the northern coastal zone the mean temperature value <24^0C caused the annual rainfall decrease to <1500 mm in the dry season for five months (Wallace et al,2012).

The groundwater at Baucau plateau very influenced by the change of temperature and rainfall. The quantity of groundwater flow below the subsurface (recharge) directly from rainfall. At Baucau plateau, the quantity of groundwater probably increase from December to the March and decrease to the May, due to high rainfall on those months. The presence of sinkholes and cave in the southern part of Baucau plateau acts as media for surface water infiltration to the underground and continuous flow to the low elevation to the surrounding area.

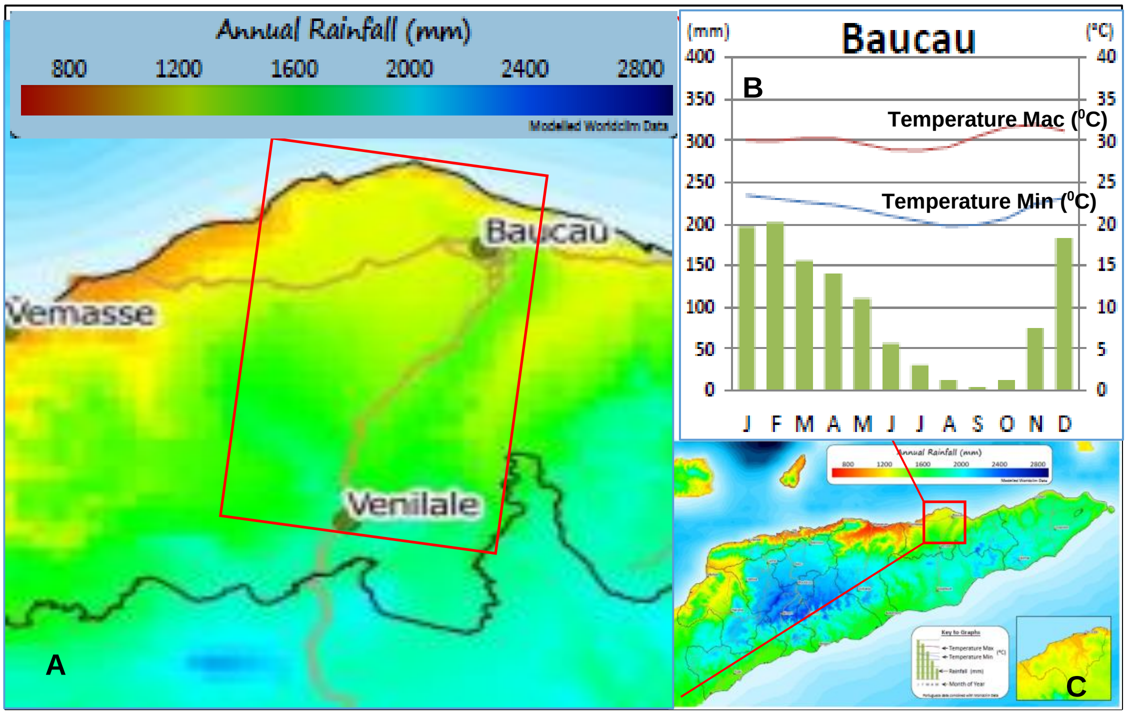

Figure 3. 3 Annual rainfall and perature of Timor Leste. Annual rainfall of Baucau plateau and surrounding area (A), Monthly rainfall and temperature of Baucau area (B) and Annual rainfall of Timor Leste *(source:*seedsoflifetimor.org/wp-content/uploads/2013/01/Rainfall-Map-With Graphs.pdf*).*

3.4 Hydrology Condition of Study Area

The principal aquifer in Timor-Leste classified to be three parts such as intergranular porosity, fissured porosity, and localized porosity. The entire of study area composed of karst from Baucau formation, Wallace *et al* (2012) described that Baucau plateau area classified into fissured porosity. As described before in geomorphology of the study area by Mentzner (1977) that the highest elevation at Loilubu area southern of Baucau plateau. The elevation decrease to the north, eastern escarpment and western escarpment. Wallace *et al* (2012) described surface water network as shown in Figure 3.4. The surface water controlled by the topography of the karst depression, mostly the elevation decrease down to the east and west escarpment of Baucau plateau and also to the north and south of Baucau plateau.

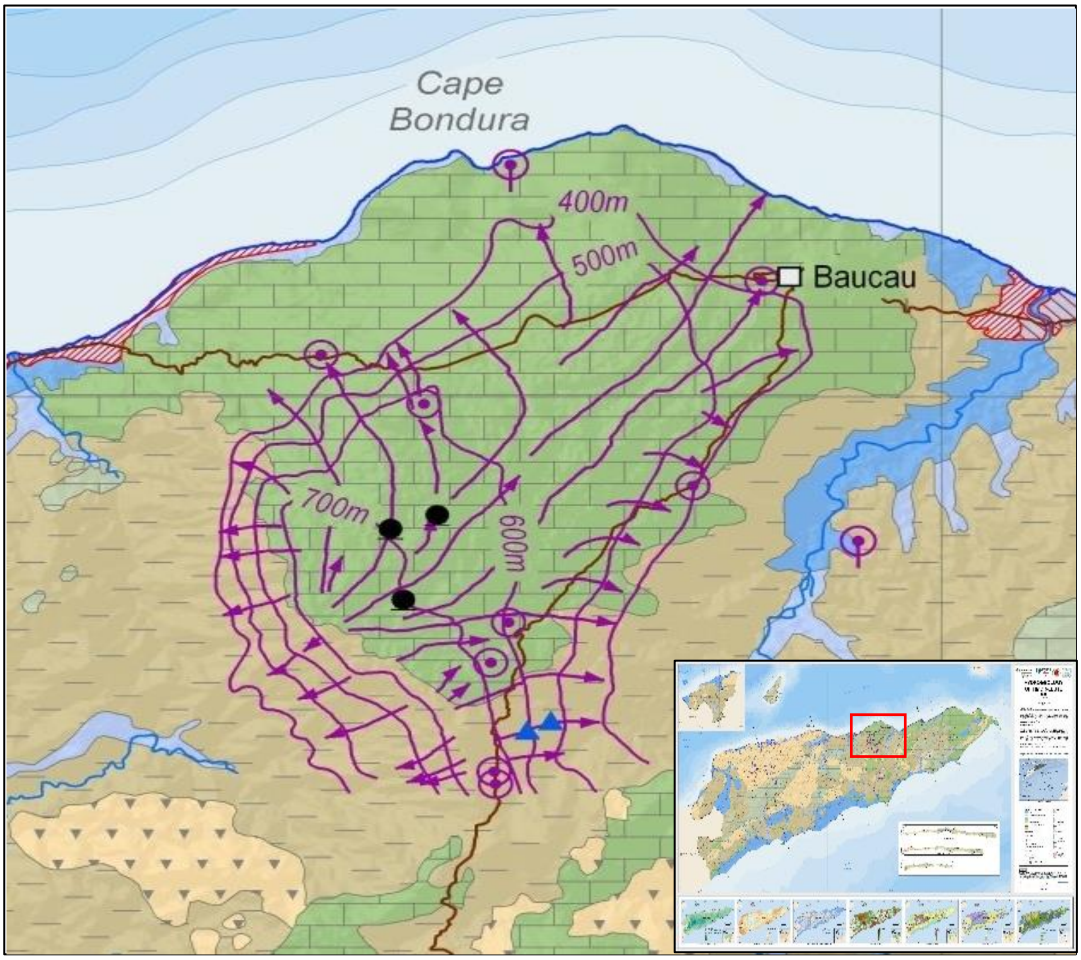

Figure 3. 4 Surface water network of Baucau plateau (Wallace et al, 2012)

The legends of local people believed that the water from Darasula on the Baucau Plateau channels off through underground cave systems in four directions: one to the western escarpment to the village of Bucoli, one to the eastern escarpment to the village of Uailili, one to Uai Lia spring in Baucau and a vertically parallel one from Uai Lia continues to the coastal springs of Wotabo below Baucau City (see Figure 3.5 left). Based on the legend believed that there are two brothers tending buffaloes at Darsula area. One day they cook and eat some yams, after eating they are thirsty and try to dig to look for water. Unfortunately, they did not water, at the same time they missing their dog and it came back all wet. They wanted to know where the dogs got this water, they made a bamboo collar tied with string for one of the dog's necks. Inside the hollow piece of bamboo, they placed ash from the fire and made a small hole in the bamboo. They followed the ash that had trickled from the bamboo collar until they came to a big cave with water inside. The younger brother then went down again to draw water. Suddenly someone came out of the water and pulled him down into it. He was under water a long time until eventually, he emerged in the still water of another cave Wai Lia spring in Baucau (Palmer, 2011).

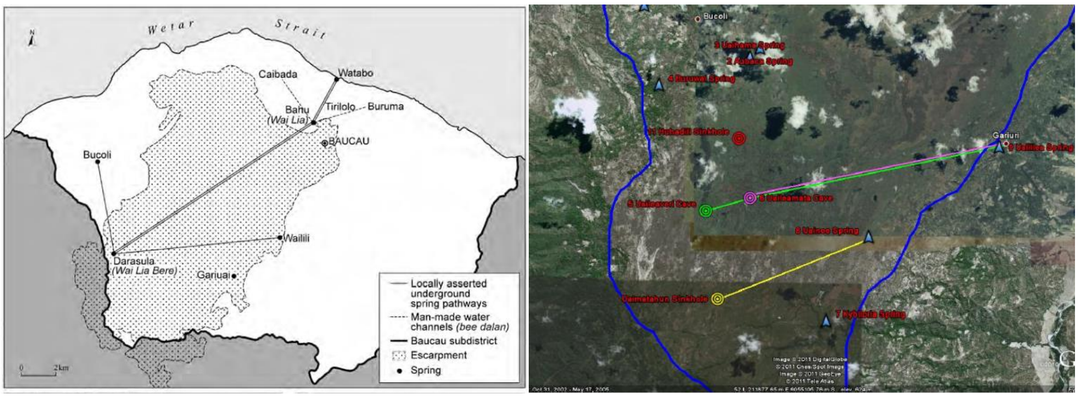

Figure 3. 5 Underground spring pathways asserted by traditional knowledge and myth narratives in Baucau (lleft) (Palmer,2010), Underground spring pathway confirmed by dye tracing investigation (right) (Furnes,2012)

Furnes (2012) reported the result of dye tracing revealed the connection of cave in Baucau plateau. The tracers placed in different four places in the high elevation plateau located in the south of Baucau plateau. The tracers introduced the direction of the groundwater flow mostly to the eastern escarpment. The tracer placed at Uaimatahun cave connects to the Uainoe cave, Uailiabere cave connects to the Uailiamata and both continue to the Uailili spring in the eastern part. By the result of dye tracing test disagrees with the legend of local people believed that Uailiabere cave connected to the Uailili spring in the east, Uailia cave in the north and Bucoli spring in the west. As we know that the limestone may have primary and secondary porosity, the secondary porosity mostly formed by the dissolution of carbonate by groundwater through the plane, fracture, and fault. The enlargement of the fissure is faster and increase the density of the fissure consequently receive more groundwater. The result of dye tracing helps us to reveal that density of fissure increase to the east and other hand high-density fissure indicated by major springs emerge on the surface in the eastern part.

3.5 Geological Background of Timor Leste

3.5.1 General Tectoni Setting Timor Leste

Timor Leste situated in the southeast of Indonesia, and northern of Australia. Timor is the largest island of the non-volcanic Outer Banda Arc (Audley-Charles, 1968). Timor Leste located in the site of an active arc-continent between the Banda Arc and the Australian continent margin (Masson *et al*, 1991). Banda Arc and Australian continent form a transition zone from subduction to arc- continent collision (see Figure 3.6). The subduction began in the Timor Island late Miocene (Audley-Charles, 1968; Cox, 2009). After ending collision between northwest Australian continental margin, the collision began in central Timor and continue migrates to the swath about 110 km/Ma (Harris, 1991).

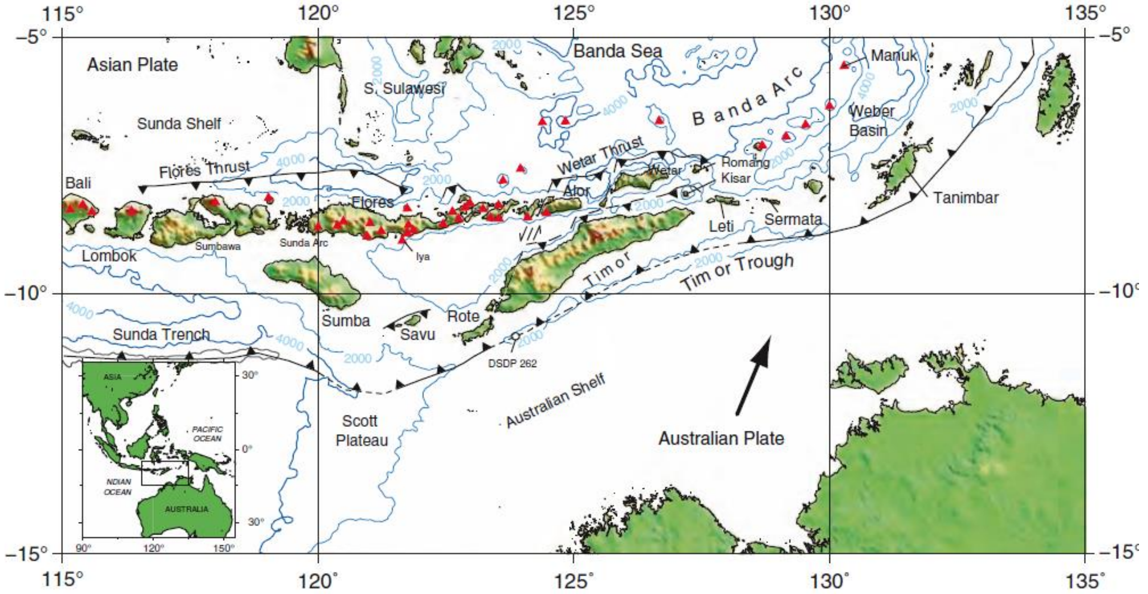

Figure 3. 6 DEM of Banda Arc Region showing active fault and active vulcanoes

There are three main of deformation in transition from subduction to collision such as; pre collisional, transitional and collisional. The pre-collisions stage of Timor began at 5-8 Ma, the result of the pre-collision formed Sunda arc. The transition phase began collision in Timor Leste at 5-3 Ma, nowdays this event still active in Sumba, Savu and Rote. Another reperesent of this phase developed back thrust system and marked by initial uplift of arc and forearc region. The collision phase started in Timor Leste about > 3 Ma. The collicion associated with complete emergence of the acretionary wedge, high uplift and erosion(Cox, 2009). During the transition, uplifted the corral terraces in entire Timor island. Coral terrace of Baucau formation as a product of uplift event. The Quaternary tectonic uplift emergence the occurancces of raised coral reef on inner and outer of Banda Arc(Cox, 2009). Chappel and Veeh (1978) conducted dating coral-reef at north coast of Timor and Atauro usinf U-Th ages, they assumed that the surface uplift along the northcoast of Timor Leste are 0.5 m/1000 year and decrease to west of Central of Timor Leste less than 0.3 m/1000 year. Than this work, continued by Cox (2009) reported surface uplift rates along the north coast vary between 0.0 and 1.6 m/ka with a mean uplift of 0.6 m/ka for the last 150,000 years.

3.5.2 Regional Geology of Study Area

The geology of study area based on Audley-Charlae (1968). Baucau plateau covered by the coral-reef limestone of Baucau formation. This formation deposited over the Viqueqeu formation. Viqueqe formation comprising of two part such as upper part and lower part. Upper part of Viqueqe fromation composed of marl and grey claystone. Baucau formation is in post-pliocene age and Viqueqeu fromation in upper Miocene age. Both formation are overlying clay of Bobonaro scaly clay in Middle-Miocene age.

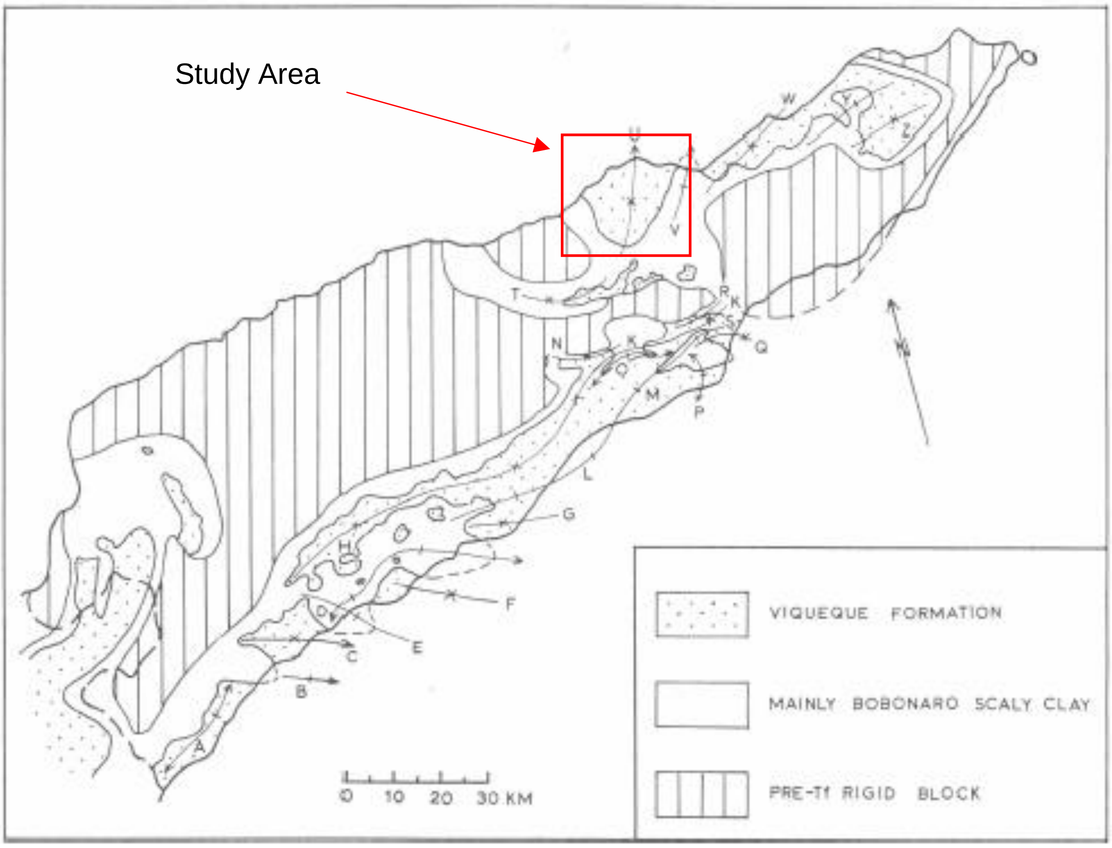

Figure 3. 7 Structures formed in formations of Mid-Miocene to Pliocene agea (Audley-Charles,1968)

As mentioned before, topographycally the study area clasified by Mentzner (1977). The eastern and soutern escarpment covered by Viqueqeu fromation and Bobonaro scaly clay, as long as in the southern of plateau. While, the Baucau plateau and norther marine terrace occupied by coral-reef limestone of Baucau.

Structurally, as show in the Figure 3.7 (symbol U), Baucau limestone deposited in a syncline of Viqueqeu fromation. The axes fold of this syncline to the northeast-southwest. Audley-Charles (1968) clasified the structure of Viqueqeu formation was formed in the Mid-Miocene to Pliocene age. Bobonaro scaly clay is an unstratified layer localized under Viqueqe formation is a competent well-stratified sequence. The

Baucau limestone deposited after Viqueqeu formation folded and faulted. During Middle-Miocene age Bobonaro scaly caly folded with Viqueqeu formation. Thus, the fold involved both formation. In the Viqueqeu-Aliambata found Viqueque formation is overturning and tightening of folds with steeper dips (see Figure 3.7 with symbol O). Further to the Matai area in the west of Viqueque-Aliambata region, reported the strike of Viqueqeu formation to the northeast-southwest and with the plunge to the north-east. The anticline is slightly asymmetrical, having a steeper northern limb. Along the crest of the fold the Viqueque Formation has been deeply eroded and in places completely removed (see Figure 3.7 with symbol A).

Structural measurement (bedding, fold and fault) from West Timor to East Timor indicated that northwest-southeast direction shortening during collision between Australia continent and Banda Arc (Zobel,2007). Harris 1991 reported maximum stress direction in the Timor is in northwest-southeast direction. Thus, fold of Viqueqeu formation identified by Audley-Charles (1968) in line with the direction of collision obtained by Zobel (2007) and Harris (1991).

3.6 Geology of Study Area

Karst aquifer is different from the non-karst aquifer (fracture and granular). Therefore, need a specific investigation to reveal the drainage pattern under subsurface. There are several works has conducted groundwater investigation over Baucau karst area. Unfortunately, these investigation did not enough to reveal the groundwater aquifer in entire Baucau plateau. Probably, due to lack of geological information aim to conduct good result in geophysical interpretation. Therefore, in this work conducted the geological investigation in the field during a week. The main purpose of field investigation to collect some geological data which may support the geophysical interpretation. Field investigation in this work comprising of surface karst feature observation, natural spring identification, stratification bedding measurements and in addition groundwater physical measurements.

3.6.1 Karst Feature Indentified in ths Study Area

In the Baucau plateau, coral-reef limestone is typically soft with a rugged upper surface, with fissures, and rock cavities (see Figure 3.8 left). These surface feature produced by dissolution of raining water which infiltrate in small fracture/crack in the karst. Due to the dissolution over time, the surface eroded water enlarged the cavity/crack. This process continues and often lead to the development of cave, sinkhole and sinking stream. The dissolution in the Baucau plateau is very important, due to development of underground drainage pattern for groundwater flow. Field investigation observed in the southern plateau high karstified than in the northern plateau.

Figure 3. 8 Cavities in the coral-reef limestone (left) and sinkhole (right) in the study area

In the southern part, surface karst feature characterized by the large sinkhole, and some sinkhole continues developed dolina, blind valley and sinking river. Further to the north, karst feature does not complex as in the north. There are large number of sinkholes in this northern area with small size (see Figure 3.8 right). Sinkholes in Baucau plateau have an important role in karst groundwater. Where they serve as an agent connection between surface water and groundwater. In the southern part, the sinkhole also acts as spring and discharge water during in heavy/rain season. For example, Uainoe sinkhole acts as discharge water in the rainy season and going to dry in the dry season. Also, these sinkholes may aim to identify underground drainage, due to the underground drainage probably align the alignments of sinkholes observed on the surface.

3.6.2 Spring Identification in the Study Area

The numerous natural springs identified in the study area in various location. Mostly natural spring emerge in the east and west escarpment of Baucau plateau and in the north-west of Uatabo beach. In the eastern escarpment the natural spring occur from Bercoli along the escarpment and continue to the Uatabo beach. In the west escarpment, occurred in the Aubaca, Buruai and continue to the Bucoli area. In the Berecoli area the natural springs occur along the road to Venilale. According to the field investigation, mostly natural spring occurred in this area in the contact lithology.

3.6.3 Lithology

The geological map in scale 1:25.000 modified from Audley-Charles (1968) with scale 1:250.000 (see Figure 3.13). Baucau plateau mostly covered by karst of Baucau formation and eastern and western part occupied by Viqueqeue formation and Bobonaro Scaly Clay. Suai formation is a minor formation was found in the northern part of Baucau plateau and alluvial deposit in Seical river and karst low depression in the blind valley.

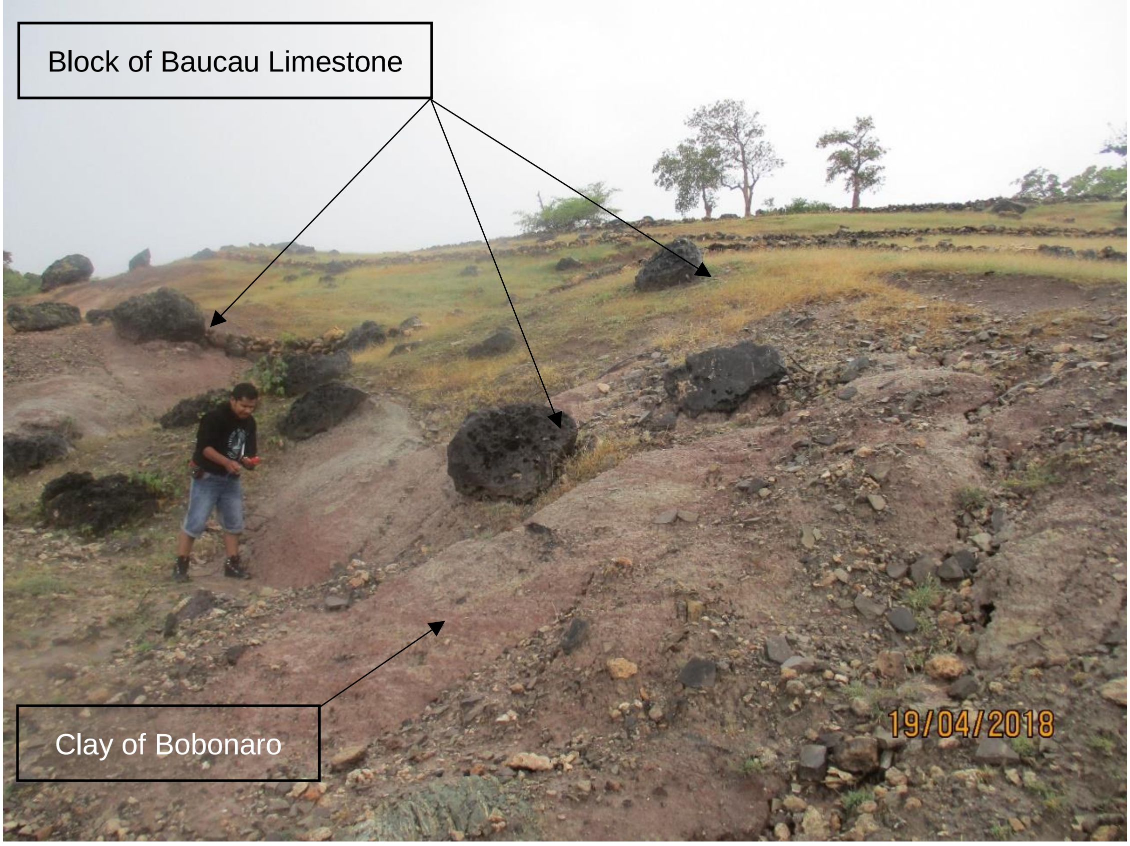

Figure 3. 9 Clay of Bobonaro Scaly Clay with block of Baucau limestone in the west of Uatabo beach

Audley-Charles (1968) classified Bobonoaro scaly clay in the Middle Eocene age. Stratigraphycally Bobonaro scaly clay lied under Viqueque formation and Baucau formation. Field investigation observed, In the surface study mostly this formation found in the southern (Venilale area) part of Baucau plateau and small spot can be found in the northern (west of Uatabo beach). Generally, Babonaro clay found on the site is the red colour. In the eastern escarpment of Baucau plateau Bobonaro scaly clay mixture with the block of Viqueque formation. In the west of Uatabo beach, the clay of Bobonao under the block of Baucau limestone. This clay exposed on the surface caused by gravity sliding of Baucau limestone (see Figure 3.9).

There are several natural springs observed in this area, unfortunately they getting dried in the dry season. Consider them as seasonal natural spring. Thus in the dry season the people who living in this area is difficult to get the water. In the dry season they go to get water from the natural spring emerge in the sea. To get these fresh water they must waiting under the low tide of sea wave. Thus, interpreted Bobonaro clay under limestone acts as barier of groundwater flow in the northern part of Baucau plateau.

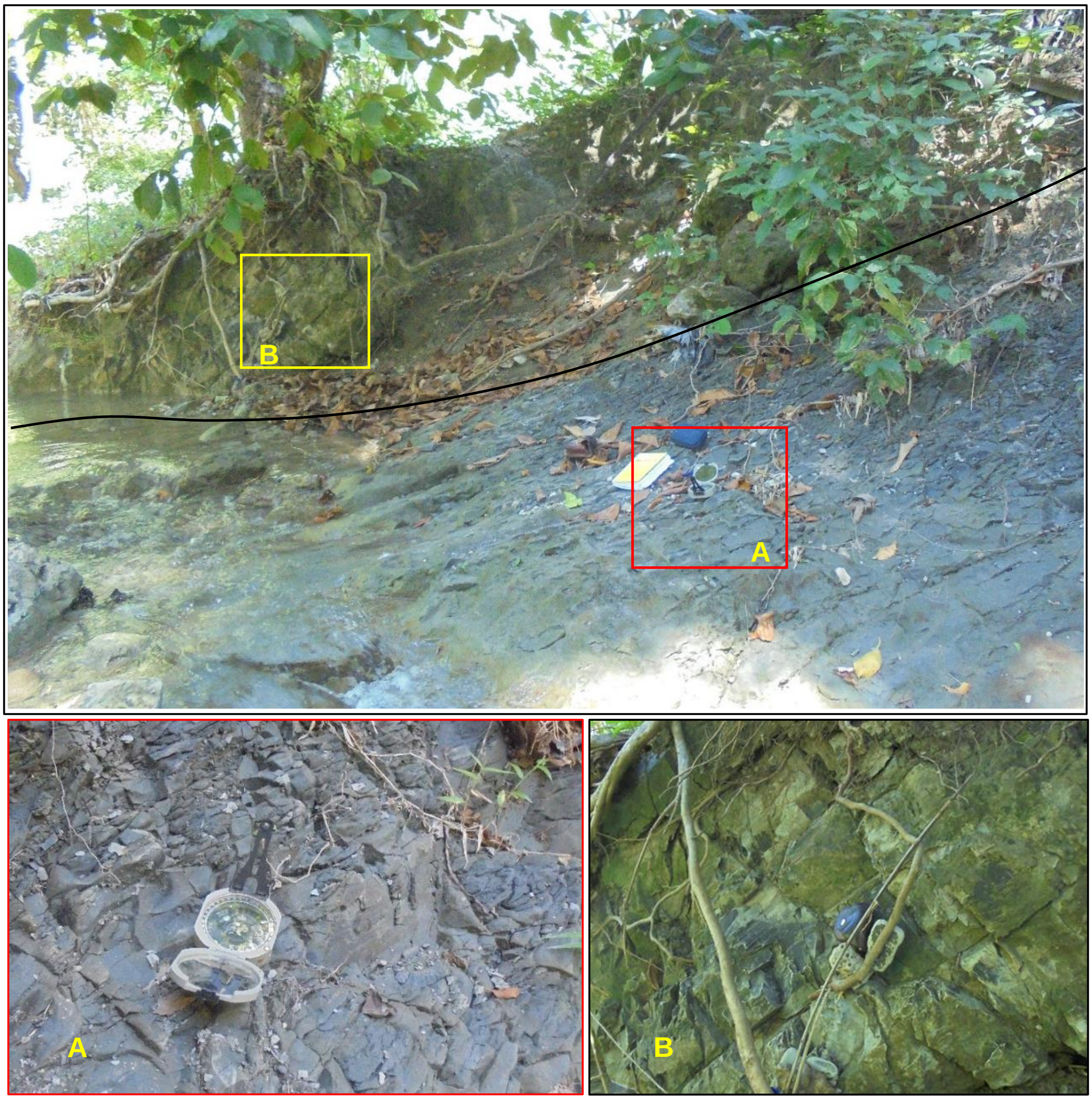

Figure 3. 10 Viqueque formation observed inside the river in Bucoli area. Grey claystone layer (A) under the marl layer (B)

Above the Bobonaro scaly clay is Viqueque formation and continue to karst limestone of Buacau formation. The distribution of Viqueque generally found in the southern part and both escarpment of Baucau plateau. Lithology of this formation observed in the field are marl and grey claystone. The grey claystone lied underlying the marls (Figure 2.10).

In the Venilale and Loilubu area, the boundary between Viqueque formation and Baucau limestone is sharp and clear. In the Venilale precisely in the area of Bercoli along the road to Viqueqeu is dominantly marls and grey claystone. Over the Viqueque formation, observed there are blocks of Baucau formation. As shown in the Figure 3.11, block of Baucau limestone localized over the Viqueque formation.

Figure 3. 11 Outcrop of Viqueque formation in the Berecole are (Venilale)

The thickness of marl layer is about 50 cm. The thickness of marl increase to north and south of this outcrop. Probably this outcrop located in the sliding gravity structure and exposed the grey claystone to the surface. In this area emerge large number of natural springs to the surface precisely in the contact of Baucau limestone and Viqueque formation. Further to the Loilubu area, the dominant lithology in the surface is marl. Another outcrop can be found inside the river in the Bucoli area and in the northern part precisely on the road to the Laga. In the Bucoli area, the outcrop of Viqeqeu located in the bank of the river, composed of marl and under the marl is grey claystone. Coral-reef limestone of Baucau formation overlay on Viqueque formation. The karst formed as a series uplift stage and marking the terrace in the northern part of Baucau plateau. It is composed of composed of a hard, vuggy, cavernous, massive, white coral-reef limestone. Baucau limestone extended from the Venilale area to the Uatabo beach and Uailili area to the Bucoli area. This limestone is a young limestone with high potential for the groundwater. Commonly high karstified in the Ostico area (Southern part of the plateau) with prominent large cave and sinkhole, and in the northern part of the plateau low karstified due to yielding small dolina.

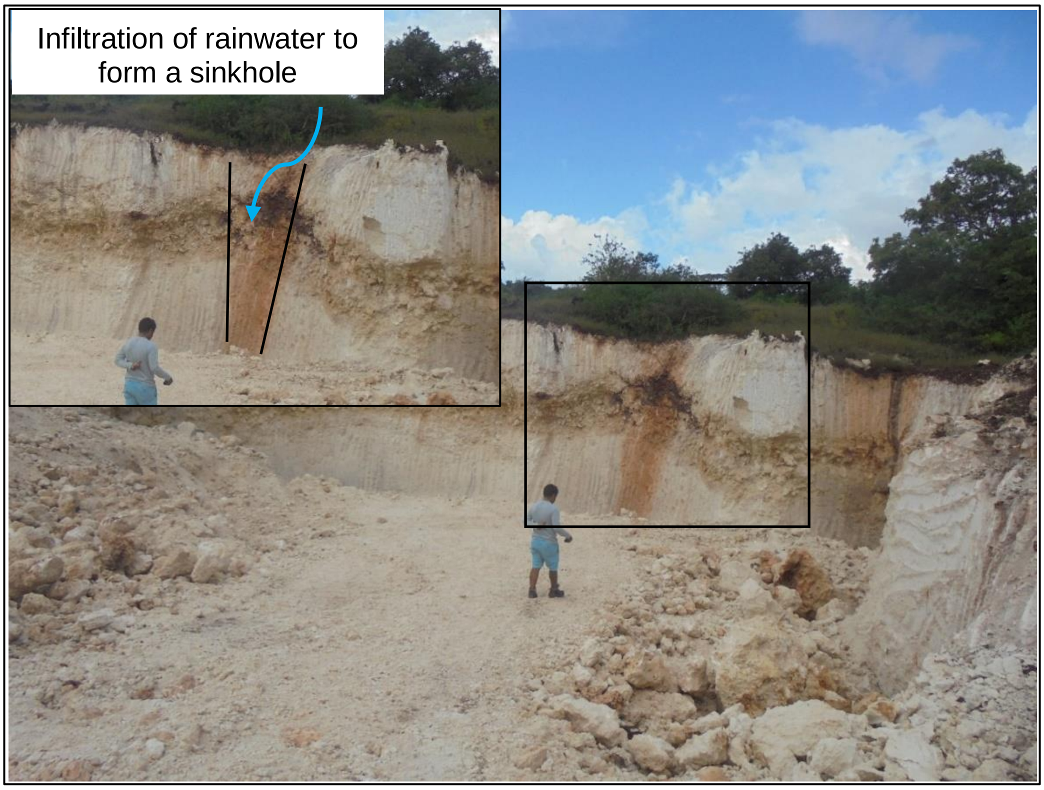

Figure 3. 12 Excavation Coral-reef of Baucau formation in the north plateau. Infiltration of rainwater disolve through the crack of coral-reef limestone and will continue formed a sinkhole

By combining regional geological map of Audley-Charles (1968) and field investigation was modified regional geological map to sclae 1:25.000. Integrating between aerial imagery and DEM of LIDAR data was aimed to delineat the new boundary of fromation. The outcrop was found in Berecoli and Loilubu area used and other observation along both escarpments were used to delineate new lithology boundaries. As in the geological map in Figure 3.13, field investigation was foud outrop of Viqueque formation and clay of Bobonaro in the Uatabo beach.

Accroding to the bedding measurements in the field, the author decided to conduct several geologiacl sections with various direction. The geological section are A-A', B-B' and C-C'. They will controlled by airborne geophysical data and borehole data (seesFigure 3.13). Due to the section cross over some TDEM and borehole site. The main goal of these section are may aim to reveal the underground drainage pattern in entire the study area. The geological sections will discuss detailed in Chapter 5.

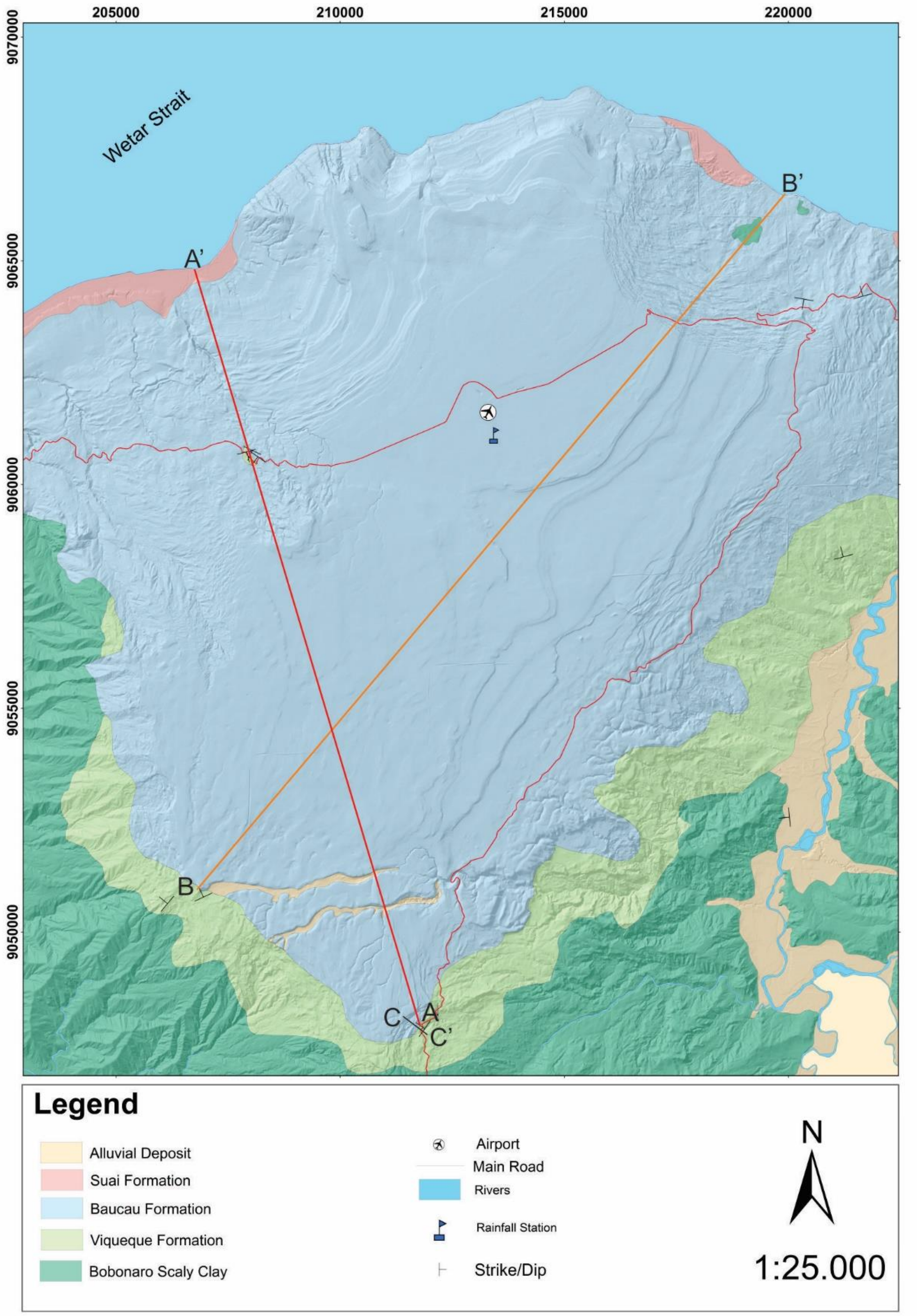

Figure 3. 13 Geology Map of Study area modifeid from Audley-Charles (1968)

3.6.4 Structural Control on Baucau Limestone Developement

This work was focused on coral-reef of Baucau limestone, due to this limestone acts as groundwater aquifer in the Baucau plateau. Field observation shows the karst limestone deposited over Viqueque formation was folded and faulted. Thus, the bedding measurement conducted on Viqueqeue formation. Through the inclination of Viqueqeu formation may aim to reveal underground drainage trend in karts aquifer. Field observation was conducted around east and west escarpment and north of plateau. The main goal is to observe and measure structural feature and lithology contact around the plateau. Structurally Viqueque formation characterized folding and fault. This finding is directly in line with the previous finding of Audlery-Charles (1968), where according to his observation reported that Baucau limestone deposited after Viquequ formation folded. Therefore, folding of Viqueqeu formation very important for underground drainage occurrences in the karst. Lithologically, Viqueqeu formation act as aquicludes under the karst limestone. Structural measurements in the field indicate the dipping of Viqueqeu formation with various values. Generally in the eastern escarpment, bedding of Viqueqeu formation inclined to the west and north-west. An outcrop measured in Uaillili area with structural value $175^0/45^0$ NE. Another outcrop in the Kaibada area with value $210^0/30^0$ NE. To the southern edge of the plateau, precisely in the Berecoli area the bedding inclination of Viqueque formation is 25^0 NE and with strike 215^0 NE. This outcrop as shows in the Figure 2.11. Further to the Loilubu area the inclination of Viqueqeu formation more less similar in Berecoli area, where the inclination ranged from 25^0-27^0 NE and strike ranged from 220^0 and 240^0 NE.

Figure 3. 14 Structure fold of Viqueqeu fromation in the estern escarpment

To the north of plateau, precisely at Bucoli area bedding of Viqueqeu formation exposed in the bank of the river. This outcrop composed of marl and grey claystone (see Figure

3.10), this lithology similar to the outcrop observed in the Berecoli and Loilubu area (southern edge of the plateau). Several outcrops were measured in the bank of the river, the bedding inclination opposite to the outcrop exposed in the Berecoli and Loilubu area. The outcrop can be observed in the along the bank of the river. The thickness of Baucau limestone is lying over the Viqueqeu formation in this area up to teens meters. The strike of these outcrops ranged from 100^0 – 125^0 NE and the inclination of bedding ranged from 45^0-50^0 NE. In the southern of Uatabo beach, along the road to Laga exposed several outcrop of Viqueque formation with the dipping value is 15^0 NE with strike 100^0 NE. The outcrop in the Bucoli and south of Uatabo beach do not mapable in the Audely-Charle (1968) geological map, due to the large-scale of map (see Figure 3.13).

Field observation indicates the Viqueque formation characterized by fold and fault. Baucau limestone deposited after Viqueque formation lifted and folded. In the Figure 3.14 the faulted folding of Viqueqeu formation situated in the eastern escarpment. It is clearly proved that the development of karst limestone of Baucau formation mostly controlled by the structure the underlying formation.

From those measurements indicates the Baucau limestone in the plateau deposited in the syncline of Viqueqeu formation. Where axial plane of Viqueqeu folds toward northeast-southwest. Probably, the plunge of the toward s to the north-east. The result of field investigation similar pattern of results was obtained by Audley-Charles (1968). Where, the fold exes direction similar to the structure found in the Viqueqeu-Aliambata region and Matai area. The result which is obtained in line with the collision direction proposed by Zobel (2007) and Harris (1991). Where the maxmimum direction from northwest-southeast. Thus, the underground drainage in entire Baucau plateau possible mostly controlled by the underlying structure. Probably, under Baucau limestone there are several tight fold and asymmetrical fold of Viqueqeu formation.

Chapter 4. Airborne Geophysical, Rainfall and Filed Measurements Data Processing And Models

4.1 Material and Data

The Major software to process and enhance geophysical data is Geosoft Oasis Montaj and another software has used the data in various format is ArcGIS. Geophysical airborne data obtained from DNGRA are airborne electromagnetic in the frequency domain and airborne magnetic. The spesific geophysical airborne data and coils configuration as in Chapter 1 Table 1.1. The traverse flight line trend to northeast-soutwest and the tie lie to northwest-southeast.

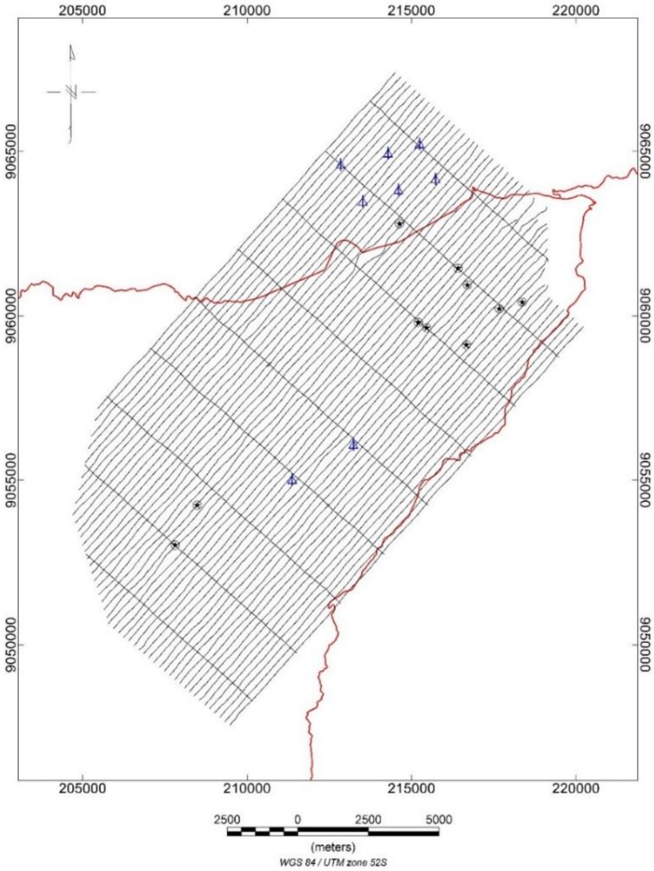

Figure 4. 1 Airborne flight line in the study area and avaiable TDEM/SNMR and borehole site in the Baucau plateau

The flight line cross over several TDEM/SNMR and borehole site, which are used to enhance the inversion of geophysical airborne. There is rainfall station located in the Baucau airport, the rainfal data used to highlight the precipitation in entire the research area. Dye tracing infromation extracted from the report, than used TRAC Software to obtain diameter of underground drainage.

The flow rate in each spring conducted by using float method and pH, EC, TDS, and temperature using Hanna instrument. To achieve the purpose of research, by correlating between geological data obtained during field investigation geophysical airborne data.

4.2 Airborne Geophysical Data Processing

4.2.1 Aiborne Magnetic Data

The original database of airborne magnetic data in GDB format. This airborne magnetic data corrected in RMI and the coordinate projected in UTM 52S. In this step reduced the RMI to the RTP to obtain RTP anomaly and continue to the vertical and horizontal derivative. From horizontal derivative in x and y-direction to obtain total horizontal derivative. In other hands the RMI use to do Euler deconvolution to identified the geometry sources. The step of the airborne magnetic data processing as follows.

4.2.1.1 Residual Magnetic Intensity

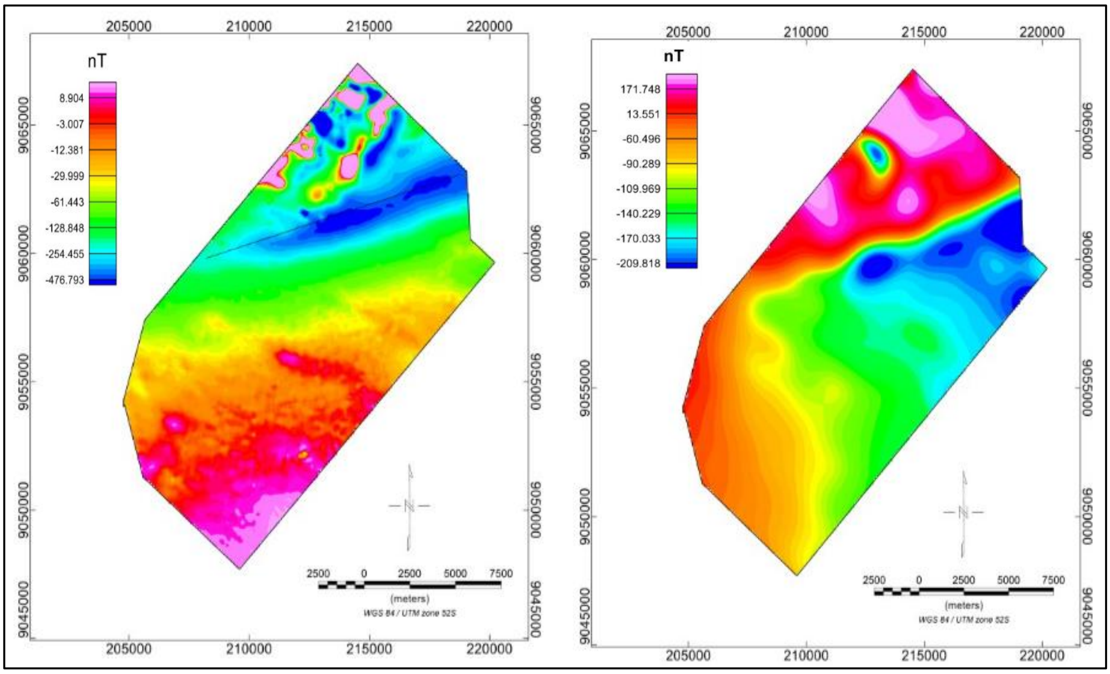

Figure 4. 2 Residual Magnetic Intensity Map (left), Residual magnetic intensity reduced to pole (right)

The residual magnetic intensity of survey area as in the Figure 4.2 left. RMI data which were corrected with diurnal variation recorded in base magnetic and were the subtraction of IGRF.The gridding of each magnetic point in RMI map using the minimum curvature algorithm and with gridding cell size is 100 m (1/2 of line spacing, where the line spacing is 200 m). This RMI map showed the distribution of magnetic susceptibility distribution along Buacau plateau.

4.2.1.2 Reduce to pole

The survey area is located in the low latitude in the southern hemisphere. Thus, before doing anomaly separation, the RMI need to do reduce to the pole using filtering technique called RTP (reduce to pole). The main objective of RTP has overcome the undesired distortion of shapes, sizes, and locations of magnetic anomalies due to the effect of the inclination of Earth's magnetic field or to align the peaks and gradients of the magnetic anomalies directly over their sources. The reduction to the pole operator developed by Grant and Dodds in MAGMAP Oasis Montaj as given in Eq.2.2. As we know that RTP is an effective technique to delineate the boundaries of the bodies causing the anomalies. To produced RTP magnetic map in survey location by using magnetic parameter that obtain from Oasis Montaj software with Inclination (I) = -33,2, Declination (D) = 2.2 and IGRF = 44284.4 nT. After applying RTP on RMI map, obtained RTP mantic map as in the Figure 4.2 right. RTP magnetic map gives the result that does not influence by Earth's ambient magnetic field where it provides a more accurate position of anomalies sources. The higher magnetic anomaly shifted to the northern part, this area composed of major higher magnetic anomaly and visible a spot of lower anomaly squeezed among higher anomaly. The lower magnetic characterized in the middle with the trending of in northeast-southwest. Extension of lower magnetic anomaly increase gradually elongated to the south-west.

4.2.1.3 Power spectrum analysis

Power spectrum transformation is a technique used to separate the magnetic anomalies produced at different source depths. The FFT was applied on the residual magnetic intensity reduced to pole for calculating the energy spectrum curves and estimating the residual (shallow) and regional (deep) sources. From the power spectrum curve, the regional and residual as well as noise signals are determined. The result of power spectrum analysis is shown in Figure 4.3, there is three linear segment obtained by using FFT technique. The gradient of each linear segment used to calculate a depth of causative source.

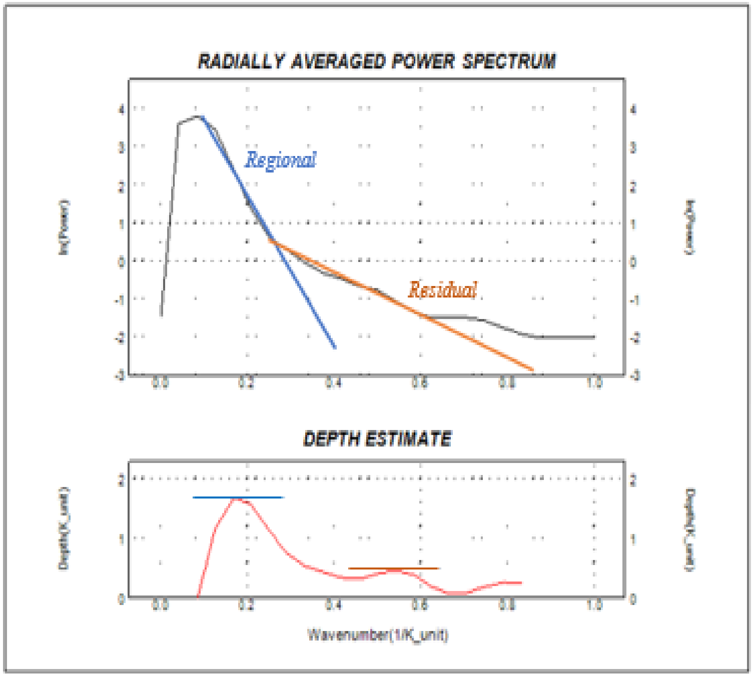

Figure 4. 3 Power spectrum analysis of RMI reduced to pole

4.2.1.4 First directional Derivative

First vertical and horizontal (x and y-direction) performed in RMI to enhance shallow sources in the survey area. This technique used to enhance linear feature which may be contact, fault, fracture etc. The magnetic lineaments extracted from enhance (directional derivative) the airborne magnetic map represents geological structure.

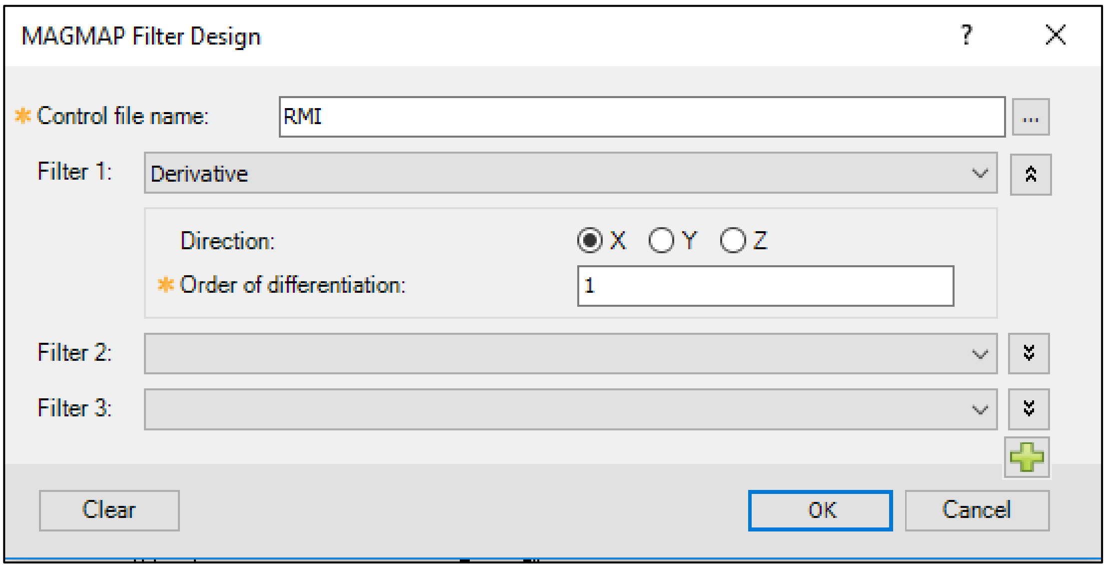

* Control file name: RMI

Filter 1: Derivative

Direction: ● X ○ Y ○ Z

* Order of differentiation: 1

Filter 2:

Filter 3:

Figure 4. 4 Calcaulation of first directional derivative in MAGMAP Oasis Montaj

The first vertical derivative (1VD) used to sharpen the edges of magnetic anomalies. Reduced to the pole of residual magnetic intensity contain shallow and deep sources. Therefore, applying vertical derivative on residual magnetic intensity reduced to the pole to sharpen the edges of the anomalies. Mathematically the directional (horizontal derivative in x and y-direction) and first vertical derivative as shows in Eq.2.3 and 2.4. The directional derivative obtained from MAGMAP of Oasis Montaj, the input data of this processing is RMI and choose the order of derivative (nth-order) than execute the data. In Figure 4.4 the output/result of directional derivative in the first order of RMI.

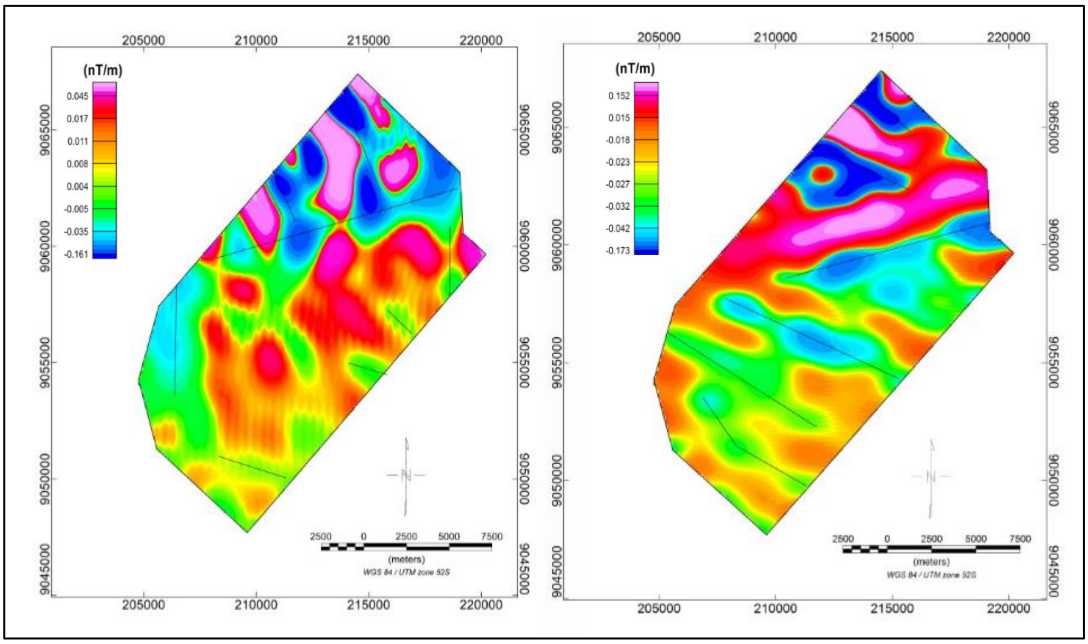

Figure 4. 5 First horizontal direvative in x direction (a), First horizontal direvative in y direction (b)

4.2.1.5 Total horizontal derivative

The combination two orthogonal horizontal derivative (dx and dy) used to define detect the edges of magnetized structures. This process according to the formula proposed by Cordell and Grauch in Eq.2.5. Combination first horizontal derivative in x direction (see Figure 4.5 left) and first horizontal derivative in y direction (Figure 4.5 right) as shown in the Figure 4.6 right. Then, the first vertical derivative obtained from RMI as shown in Figure 4.6 left.

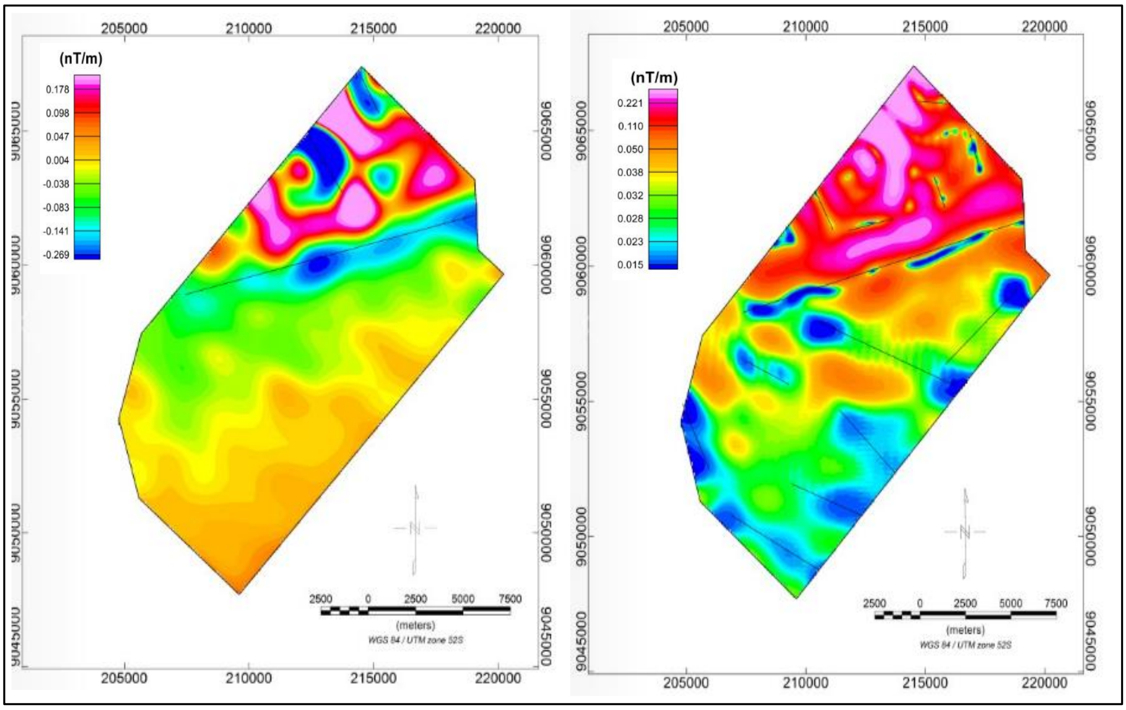

Figure 4. 6 First vertical direvative in z direction (left), Total horizontal derivative (right)

4.2.1.6 3D Euler deconvolution

Euler Deconvolution is an inversion method for estimating location and depth to magnetic anomaly source. To obtain the result of Euler deconvolution, using RMI has reduced to the pole as in Figure 4.2left. Euler depth as shown in Figure 4.7, with range depth value from 0-550 m. The Euler deconvolution is applied on RTP airborne magnetic data. The grid cell size is 2000 m with maximum depth tolerance of 15%. The map shows the locations and the corresponding depth estimations of geologic sources of magnetic anomalies. Most of the Euler solution concentrate in the north of survey area and in the network fault with trending northeast-southwest has a depth between 300-550 m. This fault possible faults affecting the sedimentary layers and also can be obtained by total horizontal magnetic field and first vertical derivative. These give consideration that there is a good agreement between Euler Deconvolution, total horizontal derivative and the karstic feature recorded by DEM of LIDAR.

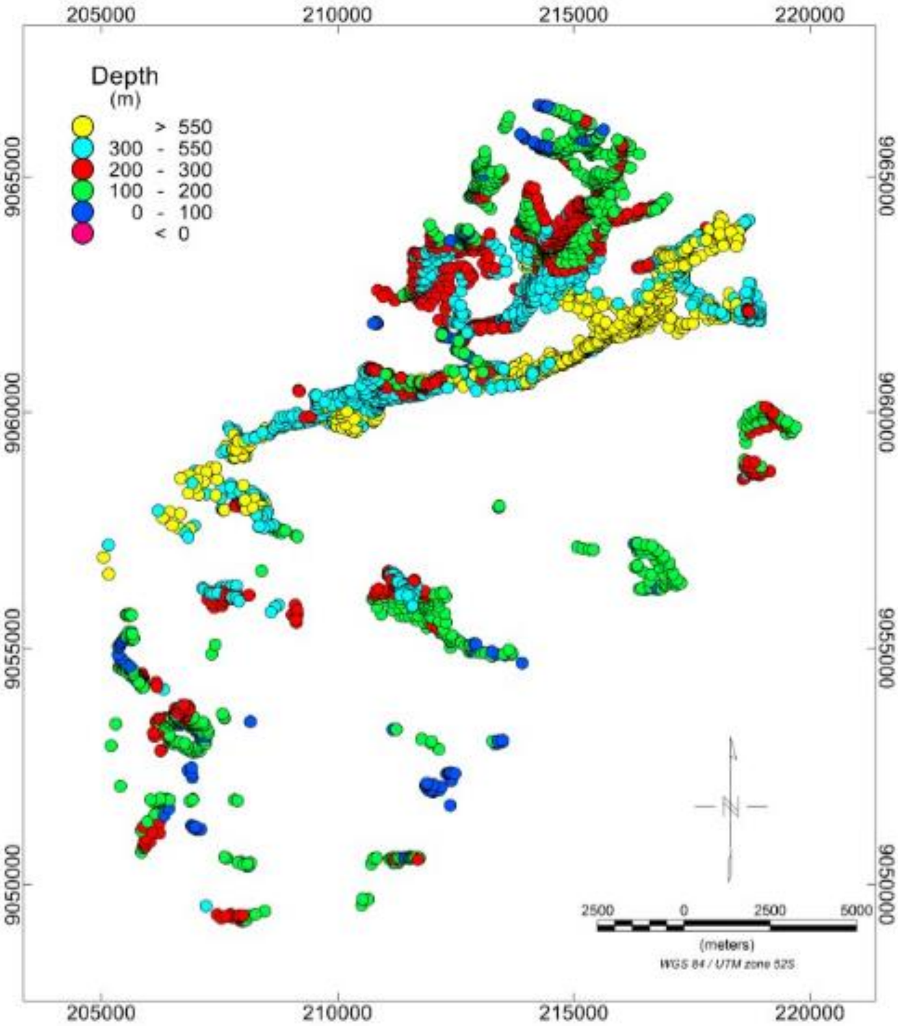

Figure 4. 7 3D Euler deconvolution

4.2.2 Electromagnetic Airborne Processing

The original database airborne electromagnetic data in GDB format same as airborne magnetic data. The electromagnetic database consists of the secondary electromagnetic field, coordinate in UTM 52S and the bird altitude from aircraft radar altimetry. Each frequency of the secondary electromagnetic field and its sensor distance can be seen in Table 1 Chapter 1. The airborne electromagnetic processing using HEM menu of Geosoft Oasis Montaj. Secondary magnetic field of each frequency used to calculate resistivity value based on the response of geological subsurface. The product of resistivity value calculated in every flight line, than griding to obtain resistivity map of each frequency. The resistivity inversion column in database channel need convert to array channel with the objective to build resistivity vertical section of every flight line. The steps of airborne electromagnetic data processing in this work as follows.

4.2.2.1 Calibration

The secondary electromagnetic field of each frequency measured in receiver consist of inpahase (IP) and quadrature (Q). In the database of data origin the in-phase and quadrature named ‘cpi’ and ‘cpq’ than followed by the frequency value. Usually, the secondary magnetic field recorded in millivolt, in this step firstly the secondary magnetic field in millivolt convert to the part per million (ppm). But normally the survey contractor it during data acquisition.

4.2.2.2 Generate Resistivity and Depth Nomogram

Each frequency of secondary electromagnetic field has a pair of resistivity and depth in term generate to the half space. Mean the generation of these nomograms is based on a uniform conductive half space model (Geosoft, 2005). To generate resistivity and depth nomogram goes to HEM and Project setup than Resistivity nomogram. The output of this process is every frequency comprising of resistivity nomogram with code R400H, ‘R’ is resistivity ‘400’ is frequency and depth nomogram with code D400H, ‘D’ is depth and ‘400’ is frequency. To view resistivity and depth nomogram by displaying grid on the map as shown in Figure 4.8.

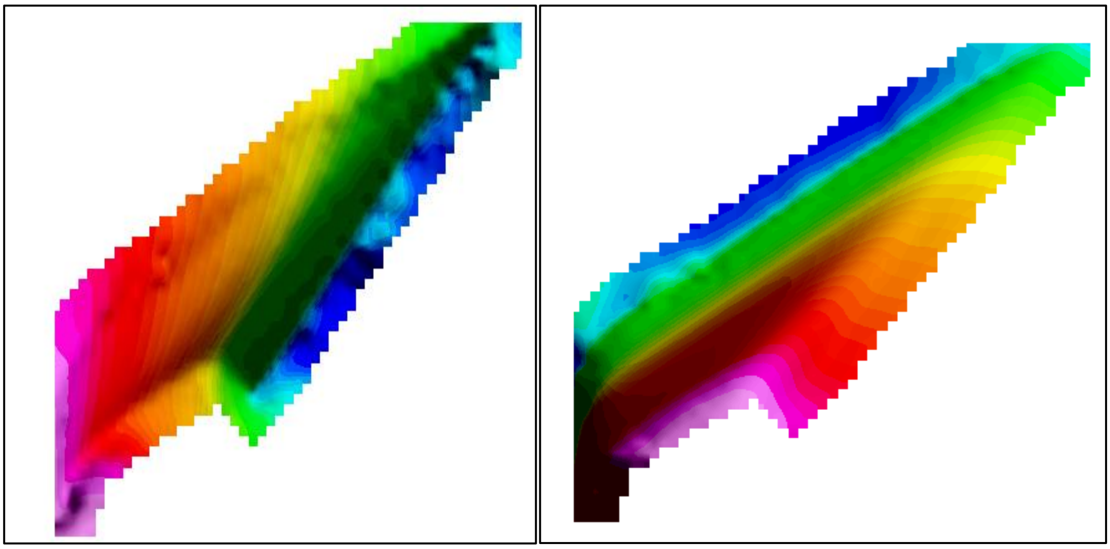

Figure 4. 8 Resistivity nomogram (left) and depth nomogram (right) of frequency 400 Hz

The apparent depth are the apparent distance form the bird to the top of the conductive half sapce. The apparent thickness of the overlying resistivity layer is obtained from the returned depth by sibstracting to the true bird heigh, where the bird heigh calculated from the radar altitude mounted in the aircraft. The concept calculating apparent depth in this process based on the Eq.2.25.

4.2.2.3 Zero levelling

Prior conduct zero leveling on inphase and quadrature of electromagnetic data before apparent resistivity and depth calculation. Remaining signals due to insufficiently bucked-out primary fields, coupling effects with the aircraft or thermal system drift are generally detected at high flight altitude several times during a survey flight (Siemon, 2009). The typical procedure is to periodically fly the bird to a height well above the earth (200–300 m), so that measurable secondary fields cease to exist. This procedure may not yield accurate zero levels at the usual survey altitude of 25–40 m, due to change in temperature with altitude can affect the transmitting-receiving coil separation or coil alignment (Huang and Fraser, 1999).

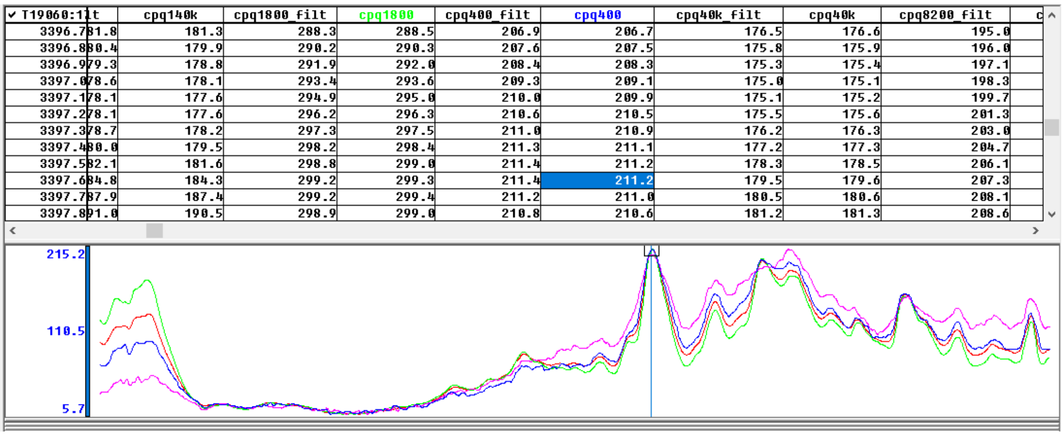

✓ T19060:1	t	cpq140k	cpq1800_filt	cpq1800	cpq400_filt	cpq400	cpq40k_filt	cpq40k	cpq8200_filt	c
3396.7	81.8	181.3	288.3	288.5	206.9	206.7	176.5	176.6	195.0	
3396.8	80.4	179.9	290.2	290.3	207.6	207.5	175.8	175.9	196.0	
3396.9	79.3	178.8	291.9	292.0	208.4	208.3	175.3	175.4	197.1	
3397.0	78.6	178.1	293.4	293.6	209.3	209.1	175.0	175.1	198.3	
3397.1	78.1	177.6	294.9	295.0	210.0	209.9	175.1	175.2	199.7	
3397.2	78.1	177.6	296.2	296.3	210.6	210.5	175.5	175.6	201.3	
3397.3	78.7	178.2	297.3	297.5	211.0	210.9	176.2	176.3	203.0	
3397.4	80.0	179.5	298.2	298.4	211.3	211.1	177.2	177.3	204.7	
3397.5	82.1	181.6	298.8	299.0	211.4	211.2	178.3	178.5	206.1	
3397.6	84.8	184.3	299.2	299.3	211.4	211.2	179.5	179.6	207.3	
3397.7	87.9	187.4	299.2	299.4	211.2	211.0	180.5	180.6	208.1	
3397.8	91.0	190.5	298.9	299.0	210.8	210.6	181.2	181.3	208.6	

Figure 4. 9 Inphase and quadrature channel displayed to examine the zero signal and ground response

Huang and Fraser (1999) grouped resistivity leveling errors into three types: leveling errors associated with a block of flight lines, leveling errors associated with flying direction, and a variety of leveling errors of smaller spatial wavelength. Therefore, display the inphase and quadrature channel to examine there is zero signal or no ground response. For example in the Figure 4.9, Inphase and quadrature channel displayed to examine the zero signal and ground response.

4.2.2.4 Apparent Resistivity and Depth Calculation

In this step the input each frequencies inphase and quadrature of secondary electromagnetic field have applied zero levelling and the nomogram resistivity calculated before. Apparent resistivity calculation using Resistivity menu of HEM and the output of this process in apparent resistivity of every frequency. In same process, used to calculate apparent depth. The process of apparent resistivity and depth as in Figure 4.10.

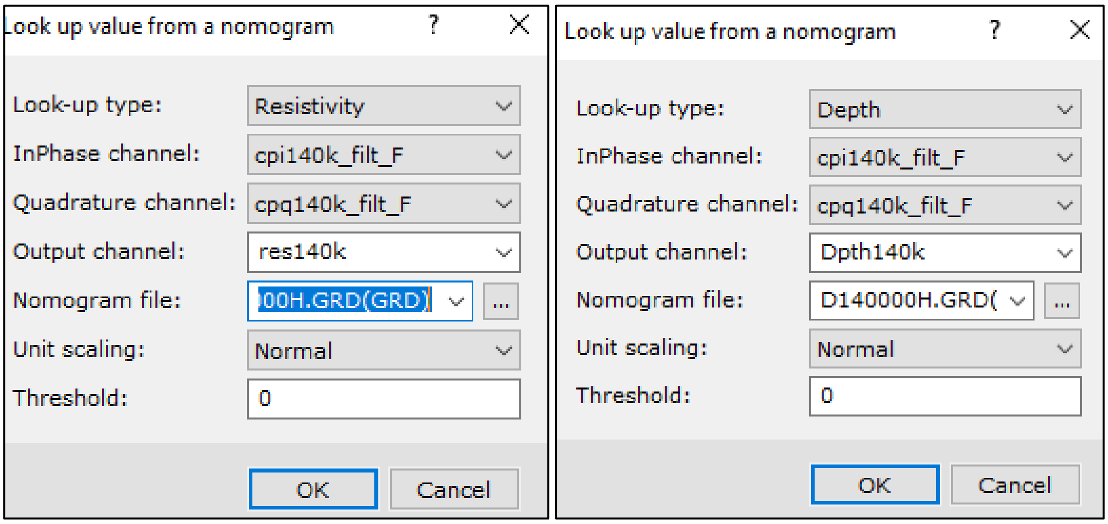

Look-up type: Resistivity
InPhase channel: cpi140k_filt_F
Quadrature channel: cpq140k_filt_F
Output channel: res140k
Nomogram file: 00H.GRD(GRD)
Unit scaling: Normal
Threshold: 0

Look-up type: Depth
InPhase channel: cpi140k_filt_F
Quadrature channel: cpq140k_filt_F
Output channel: Dpth140k
Nomogram file: D140000H.GRD(
Unit scaling: Normal
Threshold: 0

Figure 4. 10 Apparent resistivity calculation (left) and Apparent depth calculation (right)

4.2.2.5 Resistivity Inversion

The inversion of the apparent resistivity to obtain resistivity value according to the geological condition beneath the earth surface. The inversion of secondary field, in combination with the in-phase component R, with the quadrature component Q, with the amplitude and phase ratio. Amplitude refers to the square root of the sum of the squares of the in-phase and quadrature components. Mathematically this inversion based on Eq.2.24.

To view resistivity and depth nomogram by doing gridding on inverted resistivity. The griding of inverted resistivity using the minimum curvature algorithm and with gridding cell size is 100 m (1/2 of line spacing, where the line spacing is 200 m). An inverted resistivity of electromagnetic as in Figure 4.11. The resistivity map indicates the distribution of resistivity value in the survey area. The highest resistivity showed in red colour with range value 1000 ohm.m to 10000 ohm.m. The lowest resistivity value with colour blue-yellow with range value from 1 ohm.m-900 ohm.m. The highest resistivity value in the map represent the lithology in the Baucau plateau with high resistivity value and lower resistivity value in the map represent the lithology with lower resistivity in the Baucau plateau. The inversion of resistivity value in channel database. To display vertical section of resistivity value on each flight line, the database channel converts to array database channel. The array database comprising of resistivity inversion value and depth value. DEM of LIDAR data uses to control the elevation of the vertical section.

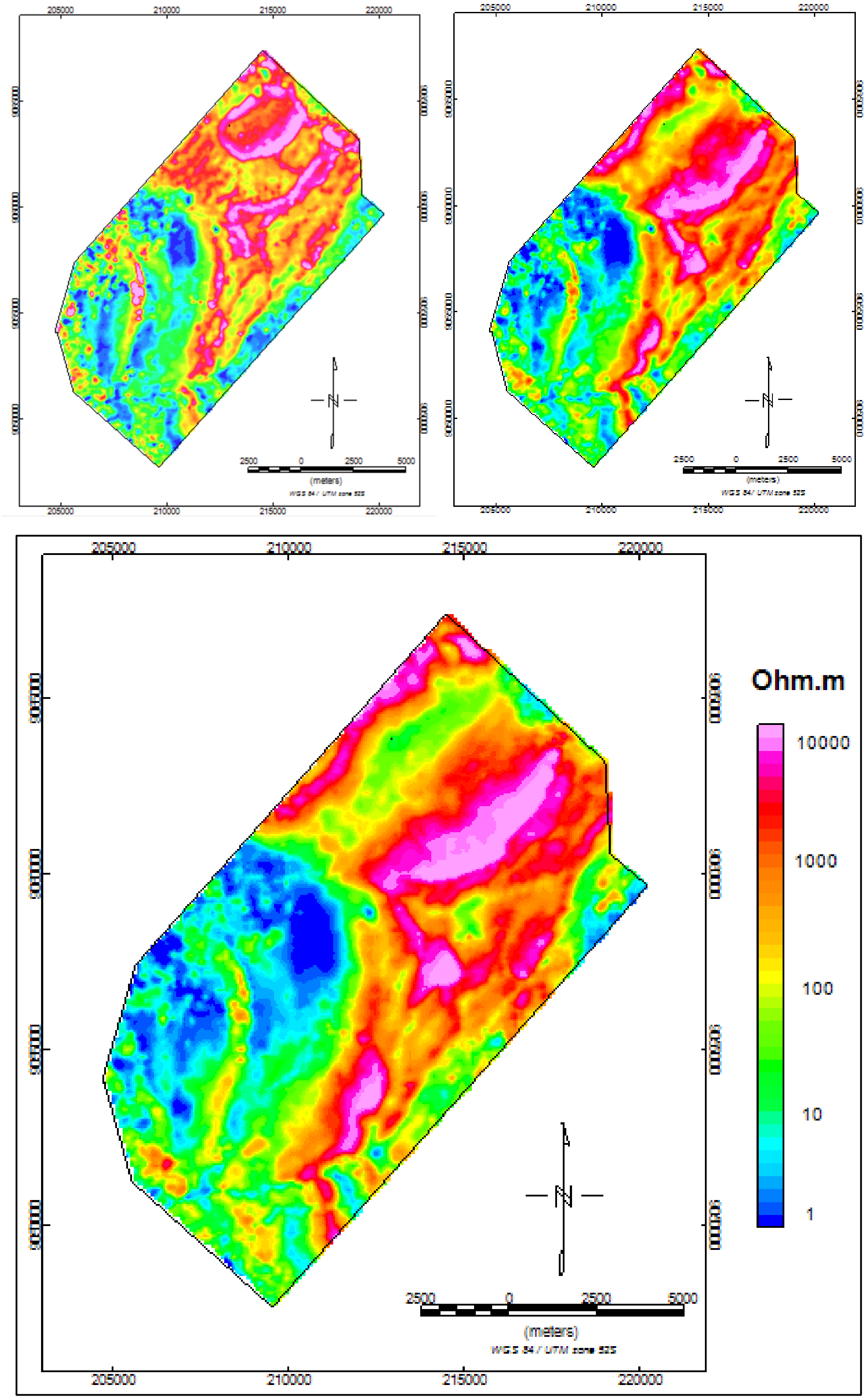

Figure 4. 11 Resistvity map of airboene electromagnetic. The resistivity map in frequency 400Hz (a), the resistivity map in frequency 1800Hz (b) and the resistivity map of frequency 140k Hz (c)

4.3 Dye Tracing Interpretation

Fluorescent tracer injected in the Uailiabere cave on 18 Jan 2011. Precipitation in Baucau plateau is high in January. The amount of this tracer was injected 4.5 kg. The distance between Introduction site to sampling site (Uailibere cave-Uailili spring) approximately 9 km. The tracers flow to the Uailiamata, than both continue to the Uailili spring in the eastern escarpment. The first arrival tracer sampling apperead at Uailili spring after 7 days. The result of measurement demonstrated in BTC graphic (see Figure 4.12). Concentration of tracer in Y-axis and Time in day in X-axis.

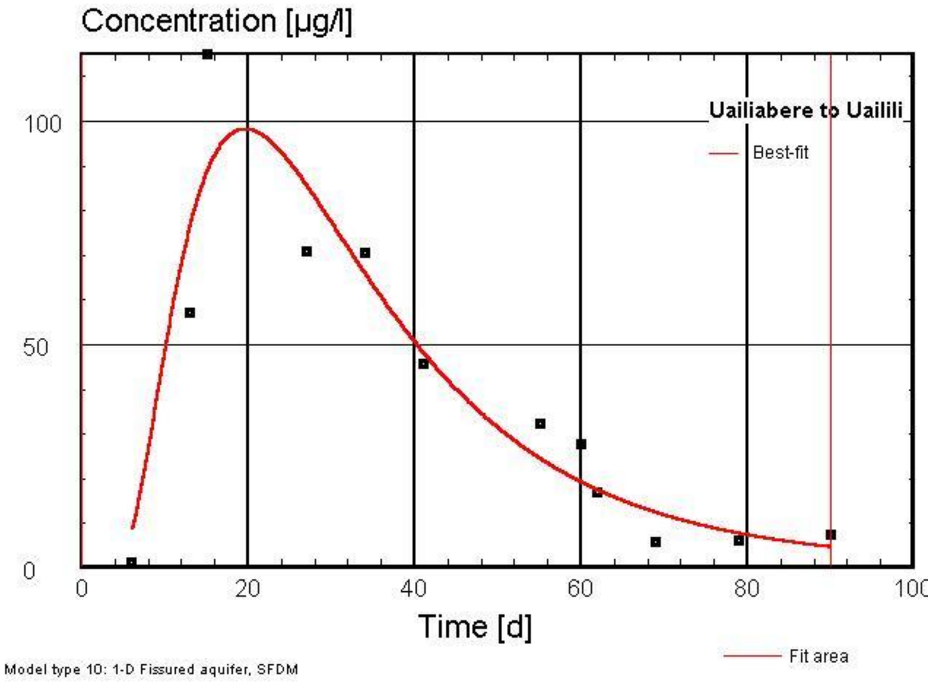

Figure 4. 12 Dye tracing grpahic of Uailiabere cave to Uailili spring

Time to peak tracer concentration about 20 days and for peak tracer concentration is about 97 µg/l. (Kass,1998) assumed that, mean transit time and distance betwee injection site and smapling site in the BTC graphic are used to calculate the mean effective velocity. The mean transit time of Fluorescent tracer is 27 days. Thus, the effective flow velocity obtained 330 km/day. Further, the effective flow velocity to determine the diameter od conduit. The drainage diamter calculation obtained 0.5 m. The Peclet-Number of fluorescent tracer is 5, it is indicated low dispersion. It indicates the dispersion of tracer, in this case with the value 5 interpreted as mechanical dispersion. Probably this low dispersion effected by the variation flow path and the diameter of underground drainage.

4.4 Rainfall Data Processing

A meteorology station is located in the Baucau airport, it is controlled by DNMG under MOPTC Timor Leste. The rainfall data used in work from 2012 – 2017. The original data obtained from DNMG in CSV file type measured in daily precipitation. The rainfall data processing used Microsoft Excell software 2013. Thus, precipitation data calculated monthly and annual precipitation to identified the intensity of surface water infiltrate under the karst in Baucau plateau.

Table 4. 1 Annual rainfall of Baucau Plateau

Year/Month	2012	2013	2014	2015	2016	2017
Jan	177	297.7	155.7	218.1	148.9	224.9
Feb	414.3	272.3	203.1	175.4	299.1	109.8
Mar	370.9	274.9	62.5	280.6	82.4	263.1
Abr	73.6	133.4	84	191.1	226.7	92.5
May	175.4	146.3	41.2	84.9	115.2	13.8
Jun	2.6	121	59.6	40.7	51	29.2
Jul	0	104	0.3	0	13.5	45.2
Aug	0	0.4	0	0.3	7.9	n.a
Sep	0	0	0	0	24	n.a
Oct	0	14.1	0	0	157.8	36.5
Nov	0	134	19.9	30.9	92.8	255.9
Dec	0	261.7	148.4	65.1	248.8	149.5
ANNUAL	1213.8	1759.8	774.7	1087.1	1468.1	1220.4

n.a=not available

Based on the result indicated that during last six year the highest precipitation about 1759,8 mm/ year in the year 2013 and lowest precipitation about 774,7 mm/year in the year 2014 (See Table 4 and Figure 4.2). By the precipitation data revealed that the high precipitation occurs on January with monthly precipitation range from 148,9 mm/month and decrease to the less than 1 mm/month on June or July. From July or August the precipitation is zero, then the precipitation begins at November to December.

4.5 Physicochemical Behavior of the Groundwater

The pH, TDS, and EC of measurements all the study sites as shown in Table 4.1. These parameters were measured in situ with a Hanna Instrument. The pH value ranged from 6.8 to 8.5. Lower pH value in the Uaidau spring and lowest pH in the Uaihisu and Aubaca spring. The lowest value probably influenced by rainwater, due to the measurements conducted in the raining. The temperature value ranged from 23.7 Celsius degree to 37 Celsius degree. The EC value ranged from 0.57 m/S to 1.26 m/S. The higher pH and EC value located in Tasi Laran spring, this spring located in the sea. Highest values influenced by the sea water.

Table 4. 2 Physical Parementer Measurements of Natural Springs

Spring	Physical Parameter			
	pH	EC (mS)	TDS (ppm)	T (Celcius)
Bucoli	7.5	0.57	325	27
Bucoli 1	7.5	0.76	226	27
Aubaca	6.8	0.73	162	28
Waihisu	6.8	0.66	280	28
Uailili	7.8	0.74	**950**	27
Uainoe	7.1	0.92	**698**	29
Uaidau	7.9	0.81	**698**	23
Baduulu	7.2	0.9	**709**	24
Lugulari	7.5	0.87	**627**	24
Uaimatahun	7.2	0.51	368	25
Uailua	7.8	0.83	**576**	27
Dambua	7.3	0.85	284	28
Loidua	7.3	0.72	340	29
Uaimataoli	7.3	0.65	492	28
Tasi Laran	8.5	1.03	**670**	28
Uailiabere	7.3	0.66	184	37
Buruai	7	0.67	172	37

The relation between temperature and TDS and EC demonstrated in graphic 4.1 and 4.1. Both graphics indicates the EC and TDS linear with the temperature. There is two point is out of the linear line, both points relate to the highest temperature were measured in the Uailiabere cave and Buruai natural spring. Probably, the highest temperature caused by the measurements conducted in the shining weather. Thus, the surface temperature affecting those measurement value. Then through the graphic infer the groundwater flow in the same regime.

Graphic 4. 1 Temperature Vs EC

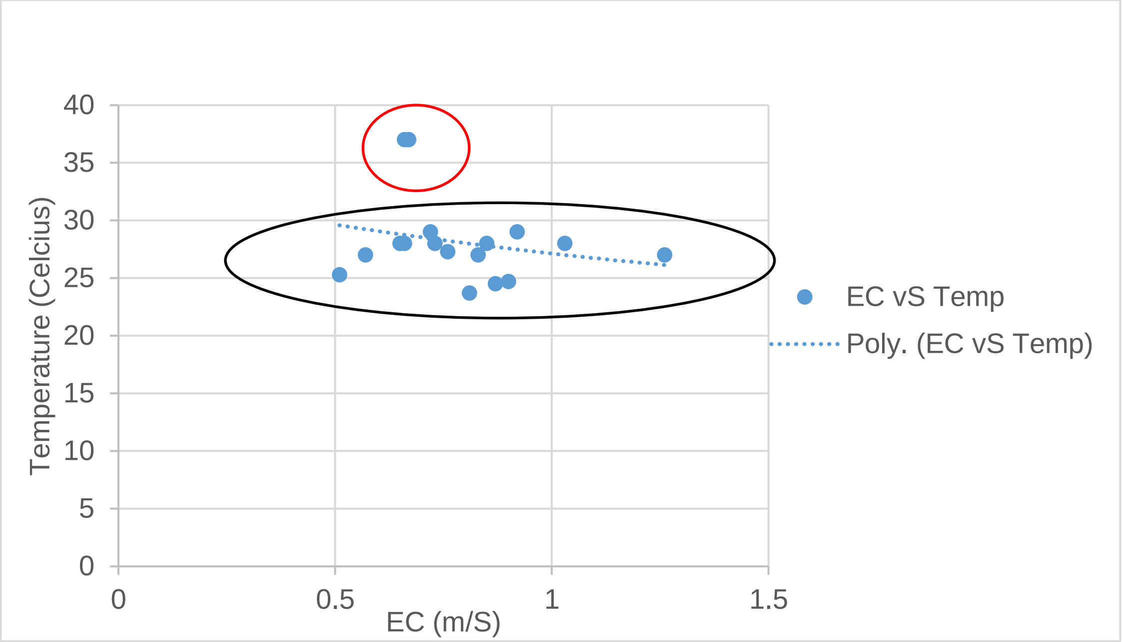

Graphic 4. 2 Temperature Vs TDS

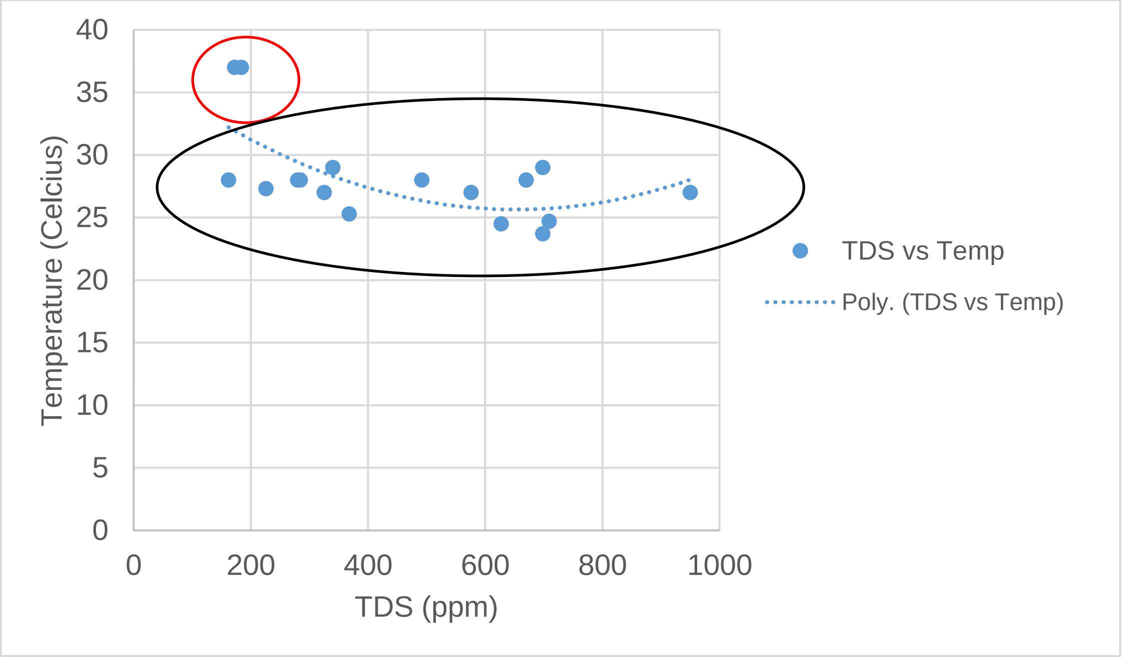

4.6 Flow Rate Data Calculation

Flow rate measurement on groundwater which is emerged in the spring. The measurements using float method. Every spring measured fourth than average the time. The average time and the distance used to calculate velocity. Before calculating the discharge of groundwater, firstly calculate the average. Than Average area and velocity of water used to determine the discharge of spring. The discharge of spring obtained by using Eq.1.1.

Table 4. 3 Discahrge of Spring in Study Area

Spring	Location	Discharge (Q l/s)	Comments
Uaidau	Berecoli	0.1	Measureable
Buruai	Buruai	0.6	Measureable
Uaihisu	Uatabo	0.5	Measureable
Uainoe Sinkhole	Fatumaca	< 0.9	Estimated
Bucoli	Bucoli	<1.5	Estimated
Uailili	Uailili	< 2	Estimated

The discharge calculation indicated in the Uaidau spring located in the Berecoli area with value 0.1 l/s. Buraui spring in the Buruai area (south of Bucoli area) indicated with value 0.6 l/c. Uaihisu spring located in the Uatabo area with discharge value 0.5 l/s. Due to the condition of the field do not support to do measurements, some estimated based on observation in the field. In the Boculi the probably the discharge of approximately about 1.5 l/s. In the Uailili area there a lot of spring emerge in the same region, due to the condition estimated the discharge approximately about less than 2 l/s. And in the Uainoe sinkhole probably the discharge about 0.9 l/s. Based on field measurements and observation indicated a high discharge in the Uailili and Bucoli area. Lower discharge in the Berecoli area interpreted Berecoli area is local flow. The variation discharge in the study area probably according to the capacity of the aquifer and degree of karstification in the spring aquifer.

Chapter 5. Interpretation and Result

5.1 Airborne Geophysical Data Interpretation

The airborne geophysical data consist of airborne electromagnetic and airborne magnetic data. The electromagnetic data was used to delineate the distribution of coral-reef limestone and the airborne magnetic data was used to reveal the geological structure in the study area. Based on the electromagnetic data interpreted the thickness of coral-reef limestone increase to the north and decrease in the south-west of plateau (see Figure 5.1). In this section, the discussion will focus on correlation among airborne electromagnetic and borehole data and TDEM information.

In order to attain the thickness of the limestone southeast-northwest and north east-south west trending within the subsurface, the resistivity vertical section was applied on flight line T19020 and L10280 (see Figure 5.1). The vertical section often used to know the vertical change of rock properties. The AEM vertical section model of this line is clear to distinguish two different layers and the resistive layer with value 1000 ohm.m above is inferred being related to coral-reef limestone of Baucau formation and the underlying low resistive with resistivity value from 1 ohm.m -100 ohm.m associated with Viqueque formation. Further, separate into two different layers, moderate resistivity with value 10 ohm.m -100 ohm.m associated with marlstone and very low resistivity with value 1 ohm.m -10 ohm.m is relatively influenced by the variation moisture in grey claystone (see Figure 5.3).

To enhance the vertical section of AEM resistivity inversion model, it was correlated with ground TDEM/SNMR information from Ley-Cooper & Davis (2015) and several boreholes data near the profile line. The distribution of boreholes and TDEM/SNMR site can be seen on the figure 5.1. The flight line of T19020 shows southeast-northwest trending. The line was crossing over four TDEM/SNMR sites and a borehole at the end of line. The TDEM/SNMR ground investigation was conducted after AEM data survey. This geophysical ground investigation was proposed by Ley-Cooper & Davis (2015) based on the thickness of limestone and paleo-drainage analysis on electromagnetic data. The AEM inversion result is agreeable with TDEM information and boreholes data. In the borehole BH_MI05 coral-reef limestone is overlying on clay layer at depth 69 m, the information of this borehole agreeable with AEM inversion (see Figure 5.3). The AEM inversion was marked maximum thickness of coral-reef limestone in Baucau formation coincide under TDEM/SNMR_L1_03 with the depth of about 100 m. From the various depth of the limestone boundary, it looks like the coral-reef limestone was deposited in a syncline. The other flight line L10280 trending to northeast – southwest was crossing over a TDEM/SNMR site in the north (TDEM/SNMR_L2_02) and a borehole (BH-M2-02) in the southern.

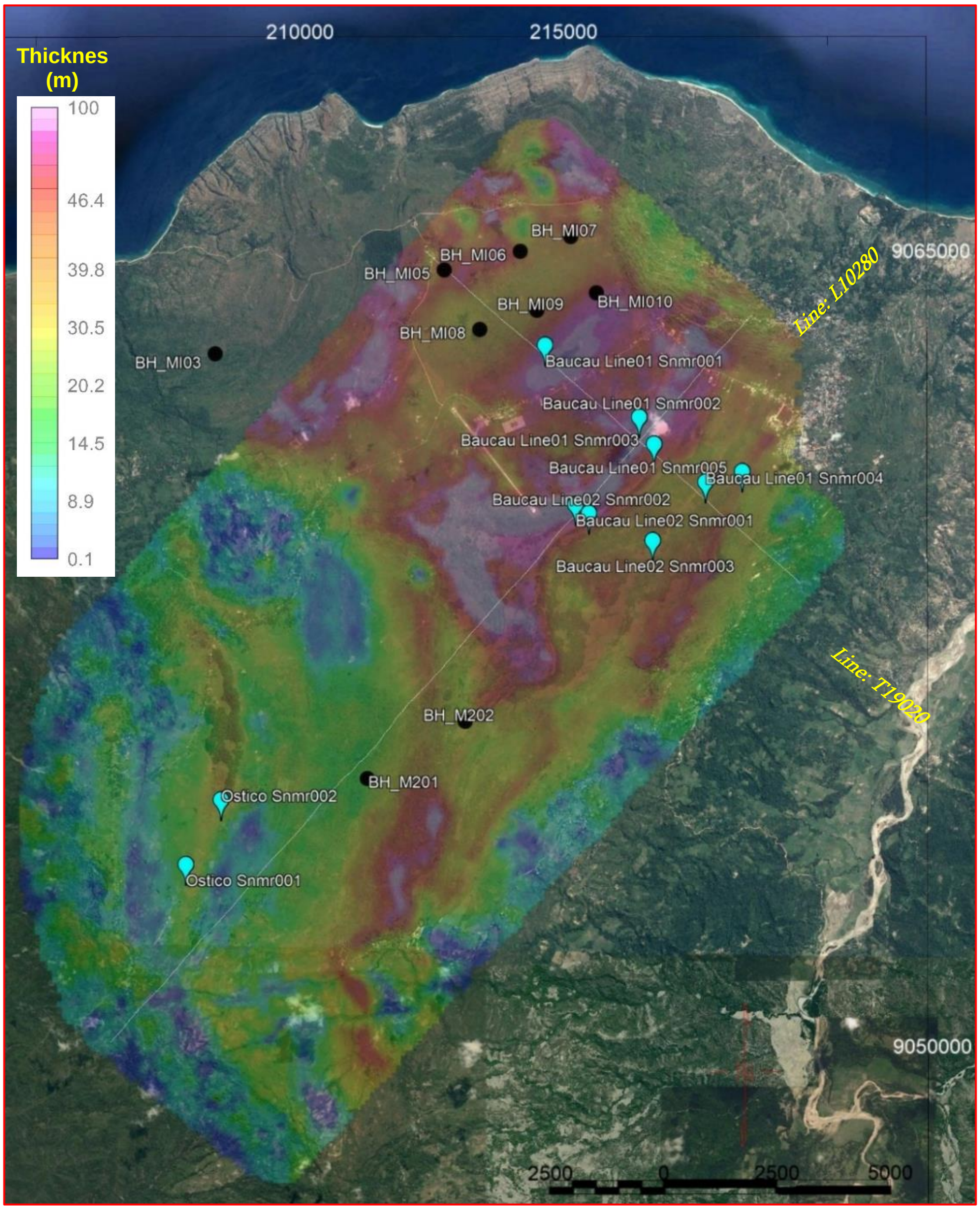

Figure 5. 1 The thickness map of coral-reef limestone Baucau formation, boreholes, TDEM/SNMR site and flight line overlaying on Google earth Map

The end of coral-reef limestone of this borehole is with the depth of about 49 m, and over this depth was crossed marls from upper part of Viqueqeu formation. The information of this borehole was well correlated with the inversion of electromagnetic. Another borehole (BH-M2-01) is near this line confirmed that the end of coral-reef limestone at 17 m, and over this depth was found marls from upper part of Viqueqeu formation. The second borehole (BH-M2-02) also agreeable with the thickness map of limestone, the end of coral-reef layer in this borehole at 49 m (see Figure 5.1).

Further to the north of plateau, there are six boreholes are located in the north-west of TDEM/SNMR_L1_03 site. These boreholes were reported that the coral-reef limestone contact directly to the clay layer which is located under Baucau formation. The information of these six boreholes are in line with inversion of airborne electromagnetic, where the end of coral-reef layer ranged from 40 m-68 m (see Figure 5.3). Field investigation, the author was found clay of Bobonaro clay exposed on the surface in the Uatabo beach. Probably, this clay has relationship to the clay was intersected by the six boreholes.

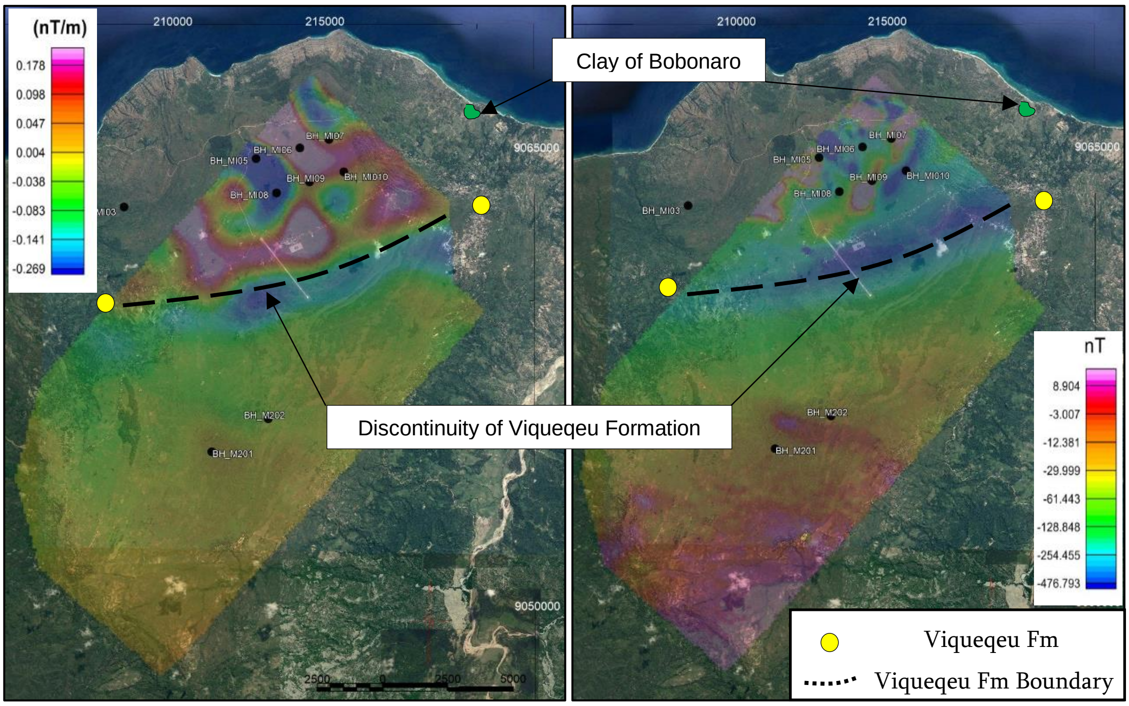

Figure 5. 2 First vertical derivative (left) and RMI (right) of airborne electromagnetic shows the anomaly feature northeast-southwest trend. This anomaly feature probably, response of the discontinuity of Viqueque formation

In another side, RMI anomaly map, vertical first derivative (Figure 5.2) and total horizontal derivative anomaly map (Figure 4.4b) shown anomaly feature (dotted black line) coincide on the Bucoli area to the south of Uatabo beach. Power spectrum in Figure 4.3 distinguished the source of depth in three segments. The first segment is regional, the response of this segment from the deeper part with depth 1.75 Km. The second segment is residual, the response of residual segment from shallow with depth 500 m. The last segment is the noise segment. Based on the geological information that, the Baucau limestone (the thickness 100 m) located above Viqueque formation (the thickness of lower and upper part: 500 m) and both of them above Bobonaro scaly clay. Probably the deeper sources caused by Bobonaro scaly clay. While the shallower sources are probably due to Baucau limestone and Viqueque formation consisting of chalky, clay and marl. The power spectrum analysis result is similar to the 3D Euler

Deconvolution in Figure 4.7, where the deeper source is around 500 m. The deeper source in 3D Euler Deconvolution mostly localized coincide on the anomaly-feature in RMI, first vertical derivative, and total horizontal derivative. Thus, probably indicates the response of the discontinuity of Viqueqeu formation. This interpretation is agreeable with geology field investigation (outcrop of Viqueqeu formation in Bucoli and Uatabo area/yellow circle in) and boreholes data. Thus, the author interpreted that coral-reef limestone is lying over Bobonaro scaly clay in the north of Baucau plateau (see Figure 5.2). Probably the high susceptibility anomaly in the magnetic map (see Figure 5.2) caused by serpentinite and volcanic rock. This hypothesis suggested due to the outcrop of serpentinite exposed in the road to Laga and volcanic rock exposed in the beach.

5.2 Geology LIDAR and Dye Tracing Data Interpretation

The airborne geophysical method is an indirect method, thus it has limitation used to identify the geological condition under the subsurface. Therefore, integrating between geophysical and another (geology, boreholes, aerial imagery and LIDAR) data will give a better result. In order to achieve the goal, DEM of LIDAR was used to obtain the surface feature of karst (terrace, lineaments, valley, and sinkholes). The DEM LIDAR useful to identify the various types of structure were formed. Structurally, there is three gravity sliding zone they are: Uatabo sliding zone, Uailili sliding zone, and the Berecoli sliding (see Figure 5.5). These sliding zone will discuss later.

Karst feature extraction on DEM and aerial imagery in this work was used manual technique. For the reason, this method is easy to identify geological elements from non-geological elements. For example in Figure 5.4, aerial imagery aim to distinguish the sinkhole was formed from the geological process and handmade. There is the various size of sinkholes were identified in entire the Baucau plateau. The distribution of sinkholes is high in the southern and northern of the plateau. In the southern part was extracted several sinkholes in various depth and length, some sinkholes transformed to be dolina, blind valley with hundred meter diameter and the depth up to tens of meter.

According to the process of sinkhole formation clasified in four types are dissolution, cover subdidinece, cover collapes and artificail. The sinkhole formed in Baucau plateau mostly are dissolution process (see Figure 3.12) and several are artificial. Where, dissolution occur when the rainwater gradually percolate through crack (see Figure 3.8 left) in the limestone and dissolving it. The soil which is trapped into the sinkhole and plug the ouflow to form a ponds . Mostly the large number of ponds were found in the northern plateau (see Figure 5.4).

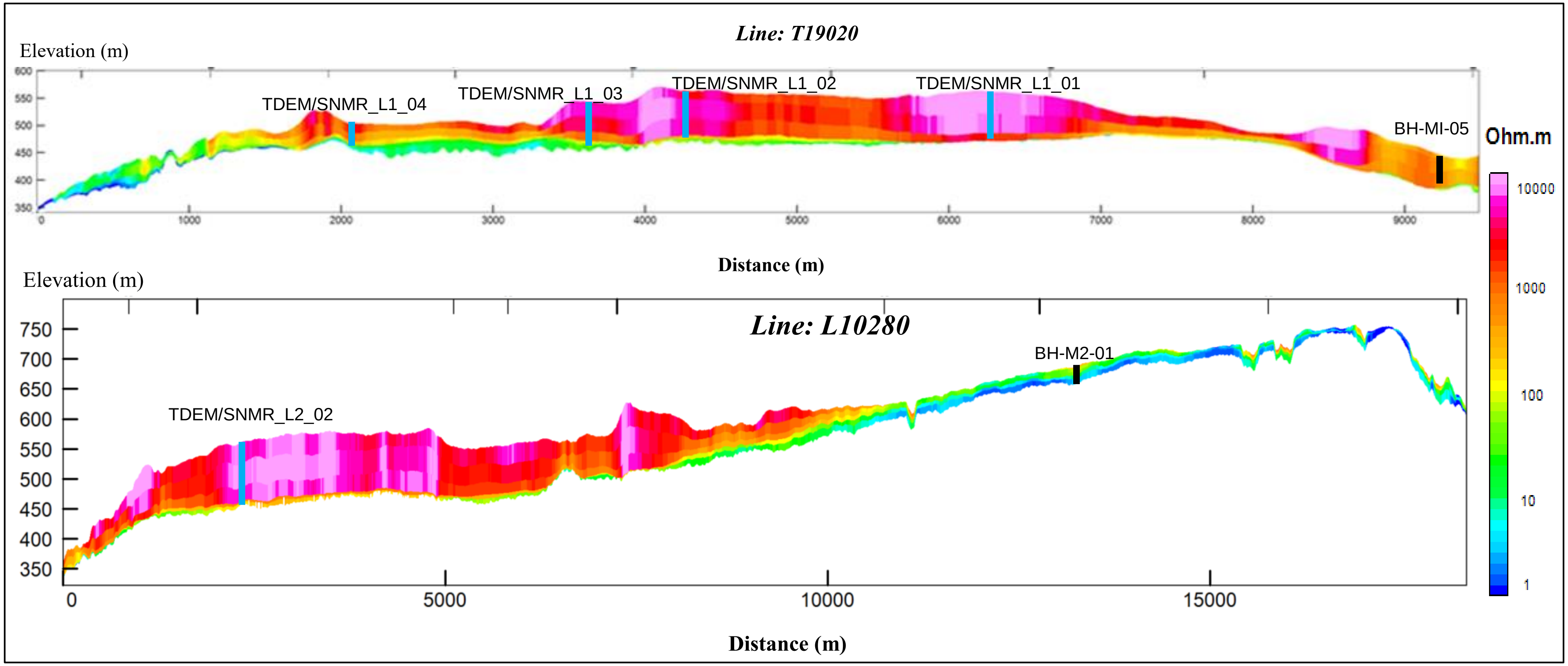

Figure 5. 3 The vertical section of inversion result of resistivity/depth model. They obtained from inversion measured in-phase and quadrature in the secondary electromagnetic field. The resistivity vertical section model of flight line T19020 trending to the north east-south west (Bottom)of flight line T19020 (above) and flight line L10280 (below)

Based on the feature and size of the sinkholes, in the southern part was high karstified than the sinkholes in the northern part. Thus, the older rocks are dissolved in advance, it is likely to create much fissured beneath the surface but can be affected also by the level of hardness of the brick against the solution. In another side there is a large sinkhole in the northern edge of the plateau (with depth 47 m and its lenght 882 m), it is Cakung sinkhole. These sinkholes have an important role in karst groundwater. They serve as an agent connection between surface water and underground drainage in the Baucau plateau.

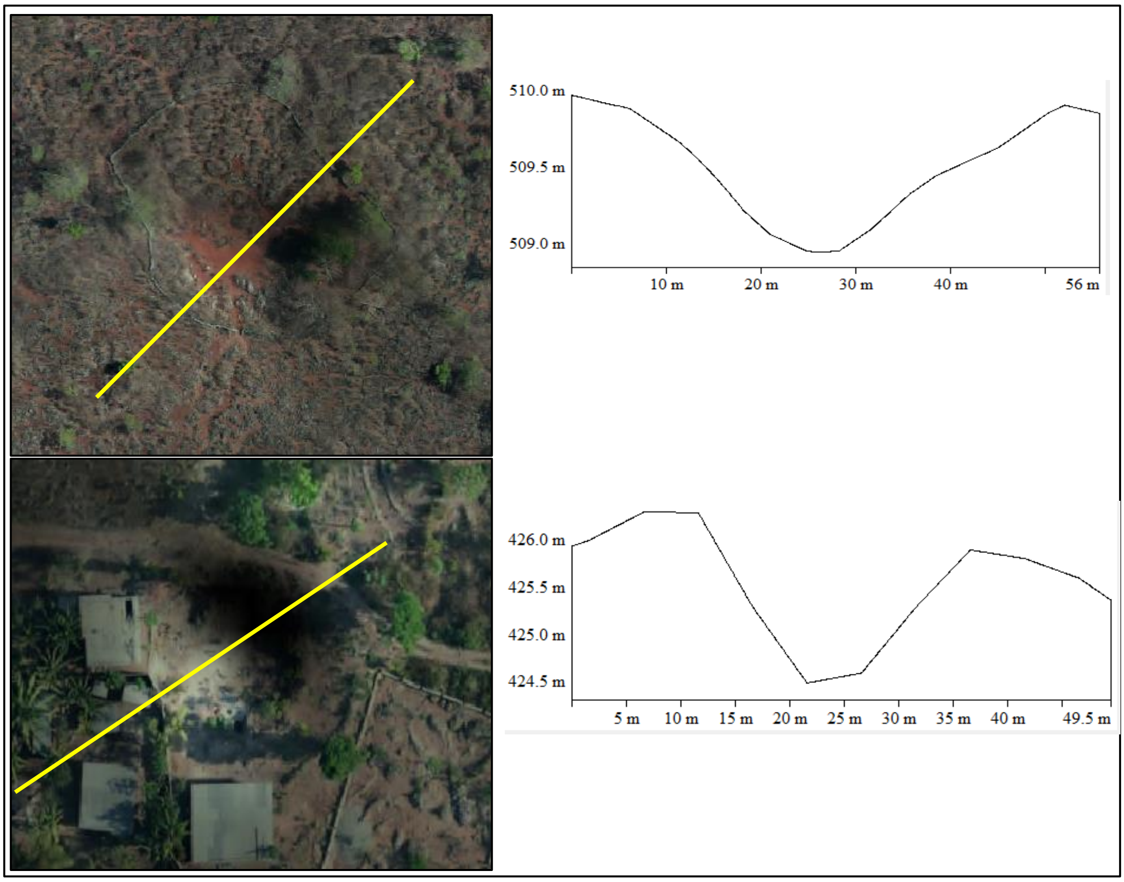

Figure 5. 4 Sinkhole feature observe in aero photo overlay with DEM LIDAR, sinkhole from nature (upper) and handmade sinkhole (bellow)

In order to identify the prominent factor on the development of karst is by analysis the karst lineaments. Field investigation in entire of survey area very difficult to observe structure in the karst, due to rugged terrain and dense vegetation. DEM of LIDAR data with a resolution 5 m was used for the extraction of lineaments. According to the lineaments' direction was distinguished to be three zones such: zone A in the south-west, zone B in the southern edge and zone C from Fatumaca to Uatabo beach. Zone A characterized the lineaments south-west the trend, zone B characterized the lineaments to the east and zone C north-east trend than turns to the west to form a separate zone. In this section will discuss these zone separately (see Figure 5.5).

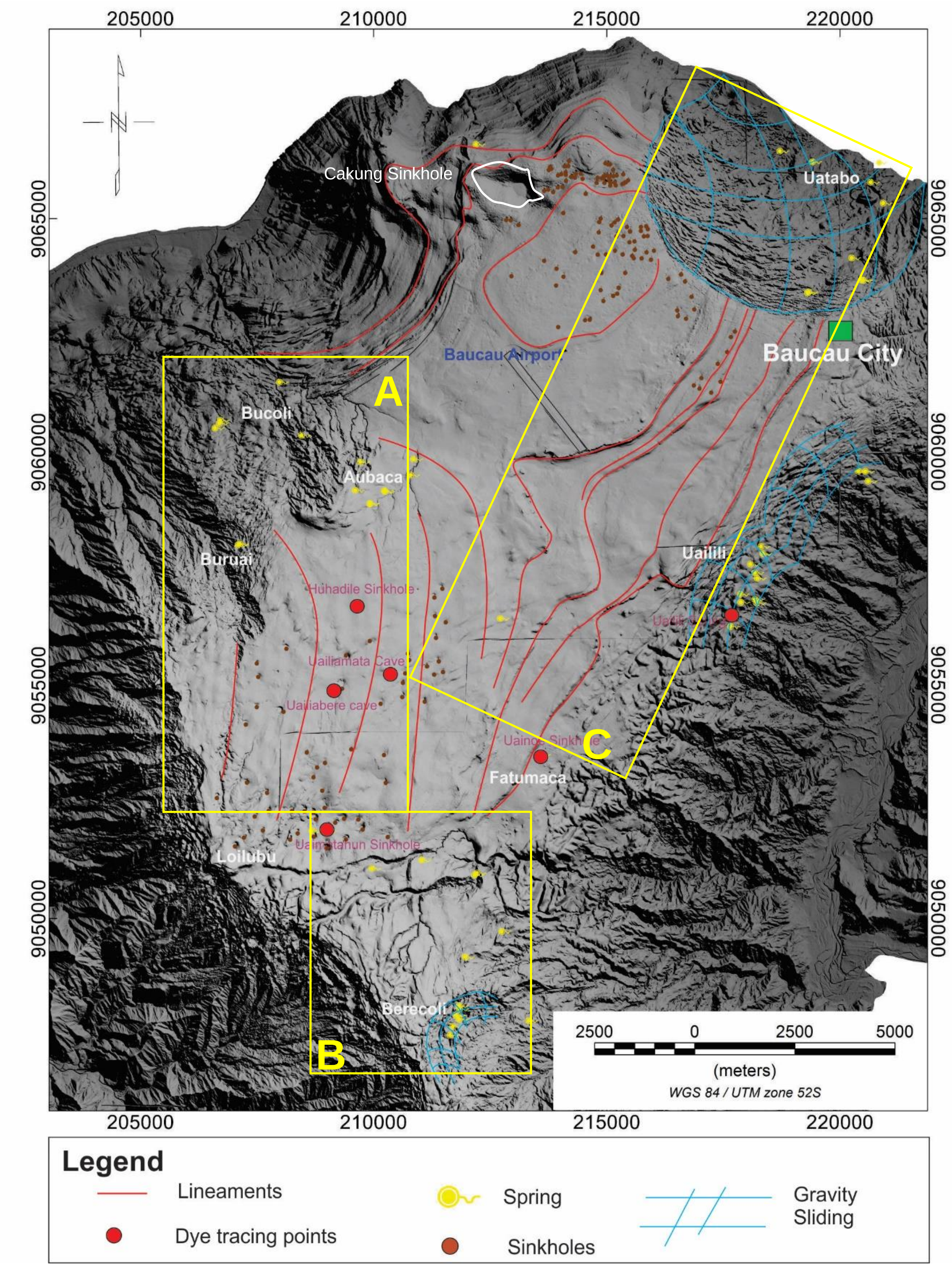

Figure 5. 5 DEM LIDAR overlay with karst feature lineaments, sinkhole, and tracer injection point. The zone distinguished based on the direction of karst feature lineaments

5.2.1 South-West (Zone A)

The airborne electromagnetic response in this zone is low anomalies (1-50 ohm.m) (see Figure 5.1), and low resistivity was interpreted Viqueqeu formation closer to the surface. The natural spring mostly emerge in the Aubaca area, Buruai and continue to the Berecoli. The emergence of these natural springs was interpreted strongly related to the decreasing the thickness of coral-reef limestone (see Figure 5.1). The lineaments was extracted based on the karst terrace, where the lineaments north-south trend. The sinkholes were extracted about 1-15 m deep with length and width of over 5 m and 200 feet respectively. They formed linear with the lineaments.

In terms of thickness, the surface high vegetation distribution and two SNMR data was showed a water concentration below 25% at a depth of 40-60 m in this area. Therefore, at 2015 conducted three well test in the south-west of the Uailiabere cave to prove the interpretation (see Figure 5.6). A borehole was drilled coincide on TDEM/SNMR point which indicated high ground concentration. Unfortunately, these boreholes are dry holes. In the edge of the south-west plateau, another private well with depth 60 m also dry hole. These borehole test confirmed the end coral-reef limestone at depth 34-39 m. The thickness of coral-reef limestone of these boreholes agreeable with the thickness of limestone in Figure 5.1. Ostico borehole 1 intersects limestone dry cave at depth 3-5 m.

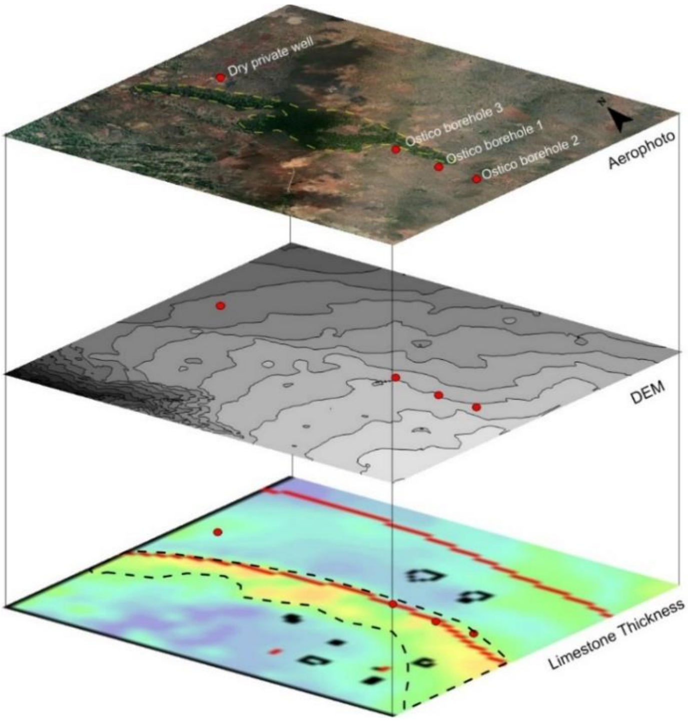

Figure 5. 6 Overlay aero imagery, DEM, limestone thickness map and dry hole site

Figure 5.7 shows the cross-section A-A' from Berecoli area to the north-west through Bucoli area (see Figure 3.13). Combination of field observation data, airborne geophysical data and borehole data has obtained this section. In the Berecoli are was found lithology contact between Viqueqeu formation and Baucau formation. As discussed in Chapter 3, structure field measurement was revealed that coral-reef of Baucau limestone deposited on a syncline with fold axes to the north-east. The orientation of this section approximately perpendicular to the fold axes (see Figure 5.1), and the author inferred there are several fold of Viqueqeu formation lying under the coral-reef.

According to the limestone thickness map in Figure 5.1, interpreted the thicker limestone considering as a syncline and thickest limestone as anticline. This cross section shows the development of the fold and the various thickness of limestone. The thickness of limestone depends on in which structure it was deposited. In the south-east part, Uaimatahun cave and blind valley coincide on the syncline. The blind valley east-west trend, it follows the axes of the fold. Further to the north-west, Uailiabere and Uailiamata caves were interpreted locate coincide over a syncline. There is an anticline separate both synclines, as demonstrated in Figure 5.7.

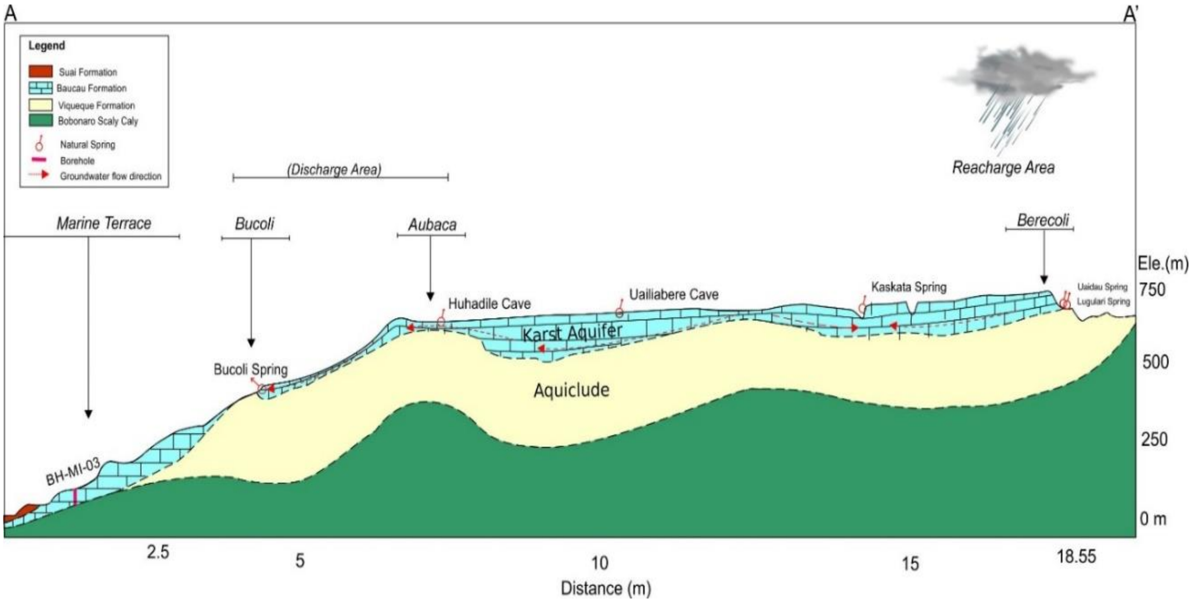

Figure 5. 7 Cross section A-A'. This cross section from Bercoli area to Bucoli area

These structures have an important role of underground drainage direction, where the drainage pattern was formed following the fold axes. This interpretation agreeable with the result of dye tracing data. The tracer confirmed the drainage pattern flow to the east, follow the axes of the fold. Based on geological and tracer result, the author concluded that the natural spring emerges in the Aubaca, Buruai, and Bucoli flow in different underground drainage, however the tracer injection point aligned to the north-west direction. The tracer was injected in the Uailiabere cave with the water level at 9 m from surface. Probably there are another karst drainage forms in the lower (lithology contact) carrying water to the Bucoli area, due to the limestone is 30 m-40 m thick in this area. Further to the Aubaca and Bucoli area the thickness of Baucau limestone is decreasing, thus interpreted the emergence of natural springs on the surface in Buruai, Aubaca, and Bucoli strongly related to the aquiclude closer to the surface. In the north-west Bucoli area, a borehole (BH-MI-03) reported the marine terrace layer overlay directly on the clay of Bobonaro. Therefore aquiclude discontinuities do not allow the continued flow of water into the most north-west region (zone of the sea-terrace).

Discharge in Buruai natural spring is about 0.6 l/s, due to the condition of spring in the Aubaca and Bucoli area do not use float method to measure groundwater flow rate. These spring are permanent spring, thus interpreted the recharge of in the southern plateau. According to the observation the flow rate of Aubaca and Bucoli higher than Buaruai area, due to there are several natural springs occur in both area. Groundwater physical (pH, EC, TDS, and Temperature) were measured in Bucoli spring, Aubaca spring, Buruai spring, and Uailiabere cave (see Table 4.2). These groundwater physical are indicated theses groundwater in the same regime.

5.2.2 Southern Edge of Plateau (Zone B)

In the most southern edge (Berecoli area) of the plateau, the lineaments do not appear in the LIDAR data. Further, the south of the valley obtained a gravity sliding zone on DEM LIDAR data (see Figure 5.5). This sliding zone is a small sliding zone if compared to the Uailili and Uatabo. The field investigation was found bedding of Viqueqeu formation exposed on the surface, precisely in the gravity sliding zone. This outcrop can be seen along the road to the Venilale, and it is comprising of marl and grey claystone (see Figure 2.11). Audley-Charles (1968) confirmed that the upper part of Viqueqeu formation is comprising of marl and grey claystone. Thus, inferred the outcrop was found in Berecoli area (sliding zone) is the upper part of Viqueqeu formation. Further along the road (to the end of the plateau) in the south was found red clay Bobonaro scaly clay. During field investigation, observed the natural springs emergence localized in the contact lithology between Viqueque formation and Baucau formation (see Figure 5.8).

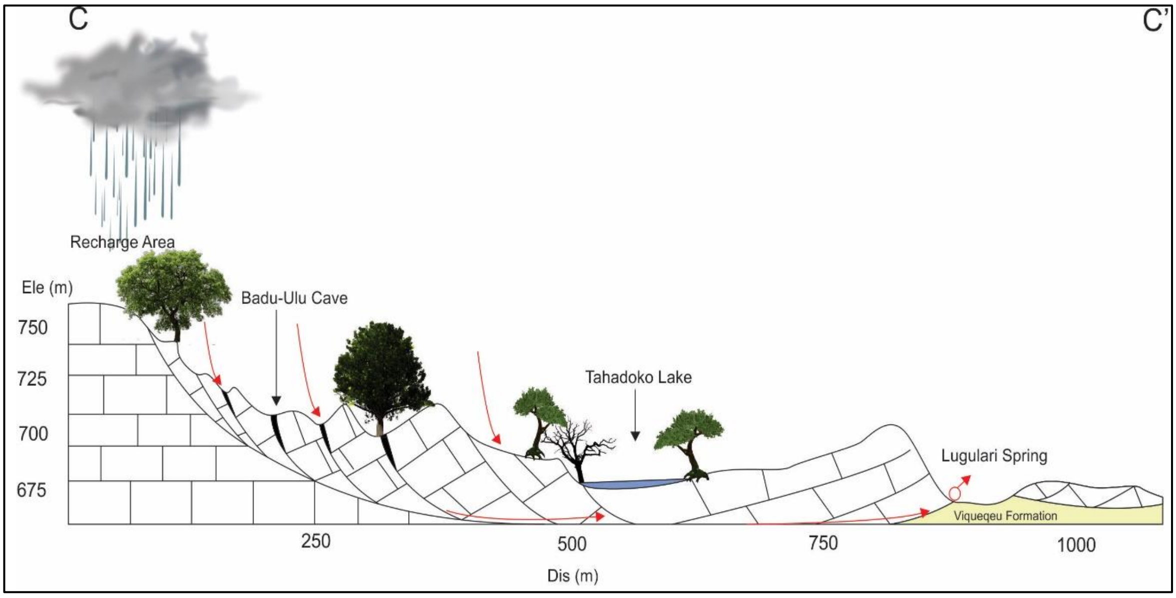

Figure 5. 8 Cross section along gravity sliding zone in Berecoli area

The higher elevation in this zone act as recharge area (see Figure 5.8), annual precipitation indicates about 1500 mm/yr. During the rainy season, the rainwater infiltrates into cave/structure which was produced by the gravity sliding. Several caves were observed on the high elevation in the site are Uaidae Ana cave, Madahu Mane cave, Madahu Feto cave (see Figure 5.9). The depth of Madahu cave approximately 80 and Madahu feto/mane cave approximately 20-30 m. Down to the low slope, there is a lake, local people named it Tahadoko Lake. The water level in these caves and lake increase during the rainy season and decrease in the dry season. The rainwater which is trapped into the caves and lake flow through along the crack to the low elevation. Probably, the water also flows through the contact lithology, than emerge on the surface form natural spring.

Flow rate measurement in several natural springs around this zone indicated the highest discharge is about 0.1 l/s. The quantity of water emerges on the surface based on the reserve of water was accumulated into the cave. Thus the natural spring around this sliding zone was interpreted local flow, where the water which is trapped in the caves in high elevation. The physical parameter such as pH, EC, TDS, and the temperature was measured the several natural springs. The pH values ranged from 7.2-7.8. EC values ranged from 0.81-0.9 mS, TDS values ranged from 627-709 ppm and temperature ranged from 23.7 – 24.5 degree Celsius.

Figure 5. 9 Natural Springs and caves observed in the Gravity sliding zone Berecoli area

5.2.3 Uaineo, Uailili to Uatabo Beach (Zone C)

In this section will discuss from Uainoe, Uailili and continue to the Uatabo area. Along the eastern escarpment, the thickness of limestone is decreased, thus the aquicludes closer to the surface. Therefore, the emergence of natural spring along this escarpment strongly related to the thickening of the aquifer layer.

Uainoe sinkhole located in the Fatumaca area, tracer indicated this sinkhole connected to the Uaimatahun cave in the south-west of Fatumaca. This sinkhole dries in the dry season and filled with water in rainy season. The field observation indicated the quantity of water in the Uaimatahun is very small compared to the water emerge in the Uainoe sinkhole. There is a drilling well in the south approximately 40 m from Uainoe sinkhole. The water level of this well is about 70 m. During the dry season, the water level of this well is constant and when pumping the water appear in the Uainoe sinkhole (pers.com. with the staff of SAS). The water table fluctuation depends on the precipitation. During high precipitation water table in this rise and water appears in the Uainoe sinkhole and decrease in low precipitation, thus Uainoe sinkhole going to dry.

Figure 5. 10 Uainoe sinkhole. In the rain/wet season (left) and In the dry season observed on the aerophoto (right). The direction of water flow indicated in yellow line in the figure

Due to increasing the quantity and emergences water in Uainoe sinkhole interpreted there another drainage containing large water connected to the Uaimatahun drainage. The water level in the Uaimatahun cave is 2 m considering as upper drainage, and lower drainage probably in the contact lithology between marl and coral-reef of limestone. The emergence of groundwater in Uainoe is similar to spring in the Bucoli, where the emergence of spring related with the Viqueque formation closer to the surface (decreasing the thickness of aquifer).

Figure 5.11 indicates the underground drainage pattern interpreted according to the sinkholes alignment on LIDAR and aero imagery. The topography of underlying layer (Viqeuque formation) as an aquiclude is highest in the Uaimatahun cave and sloping down towards Uainoe sinkhole. Therefore the drainage pattern formed according to the structure of Viqueque formation.

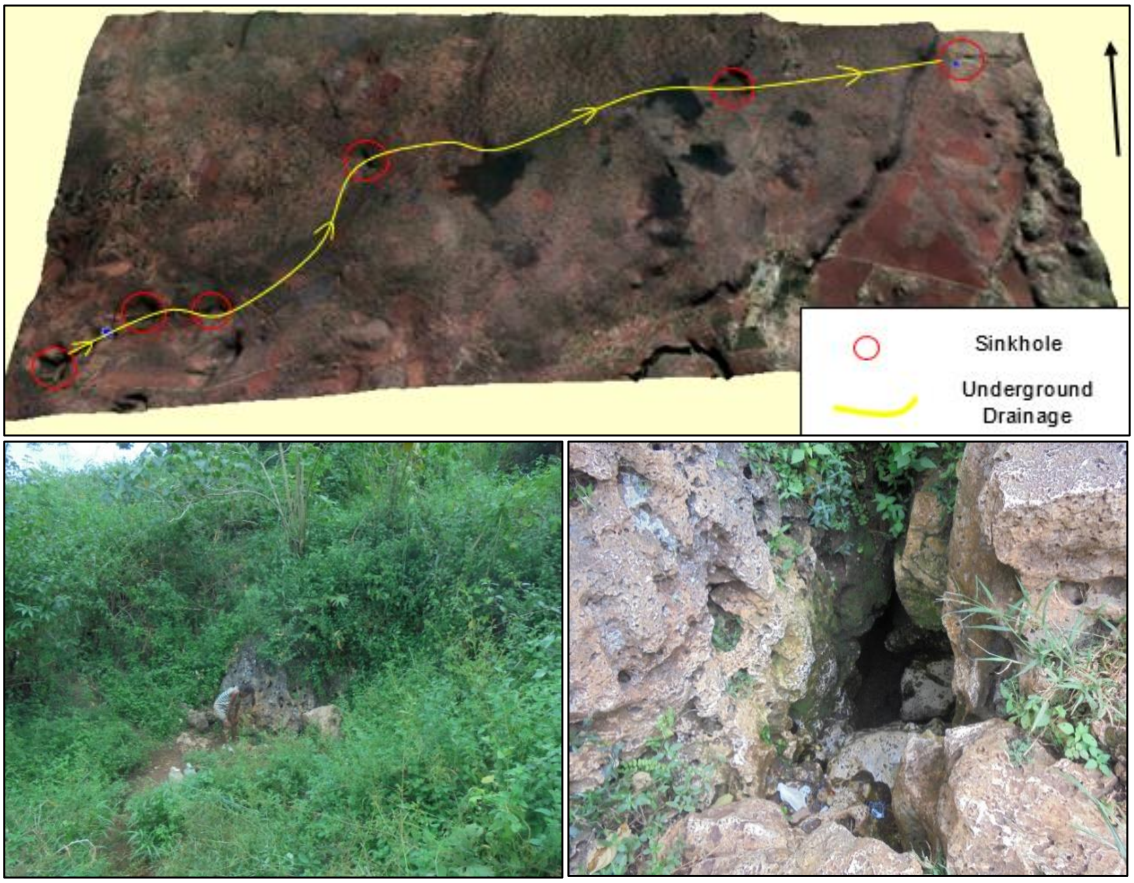

Figure 5. 11 The underground drainage pattern interpreted accroding to the sinkholes alignment on LIDAR and aerophoto (Top). Uaimatahun cave (Bellow)

Karst surface feature observed on LIDAR data and aerial imagery may aim to guess the drainage pattern beneath the surface. Sinkholes alignment probably coincide with the underground drainage pattern (see Figure 5.11). This drainage direction similar to the paleochannel proposed by Furness (2012). Where, aquiclude is highest in the south-west and sloping down towards the sea in the north and east and west escarpment. Therefore the drainage pattern mostly formed according to the topography of the aquicludes layer (Viqueqeu formation).

Further to north-east Uainoe is Uailili area. Structurally, Uailili area located in the gravity sliding zone. Natural spring abundantly emerges in this area. Similar with another natural spring have discussed before, that the emergence natural spring in Uailii area due to the decreasing the thickness of coral reef limestone. Dye tracing informed the source of this groundwater from Uailiabere and Uailimata cave, the discharge of Uailiabere cave about 3 l/s (pers.com. with the staff of SAS). The quantity of water Uailili is higher compared to the Uainoe sinkhole, due to a large number of natural spring. Flourence tracer calculation obtained the diameter of drainage is about 0.5 m. The Peclet number indicated low dispersion, probably related to the variation of drainage diameter and drainage orientation (see Figure 5.12).

Figure 5. 12 The underground drainage pattern interpreted accroding to the sinkholes alignment on LIDAR and aerophoto (Top). Uailili spring (Bellow left), Uailiabere cave (Bellow right)

Figure 5.12 indicates the underground drainage pattern interpreted according to the sinkholes alignment on LIDAR and aerial imagery. The topography of underlying layer (Viqeuque formation) as an aquiclude is highest in the Uailiabere and Uailiamata cave and sloping down towards Uailili area. Therefore the drainage pattern formed according to the structure of Viqueqe formation. Karst surface feature observed on LIDAR data and aerial imagery aims to guess the drainage pattern beneath the surface.

Further to the north of Uailili is Baucau city than continue to the Uatabo beach. The thickness of coral-reef limestone increase to the north. Natural springs mostly emerge in the eastern of gravity sliding zone (see Figure 5.5). Where the emergence of natural spring aligned with lineaments. Another natural spring emerges in the sea. According to the airborne electromagnetic data and ground TDEM information indicated the thickness of coral-reef limestone increase to the northern part (see Figure 5.1 and Figure 5.3). Total horizontal derivative and RMI of airborne magnetic data reveal there is a structure with trend north east- south west. According to the field investigation indicated probably the lateral end of Viqueque formation in the Bucoli and south of Uatabo beach (road to Laga). Thus, possible the response of

RMI anomaly and total horizontal derivative anomaly feature is related to the discontinuity of Viqueqeu formation (see Figure 5.2).

Figure 5.11 shows the cross-section from Loilubu area to the Uatabo beach (see Figure 3.13). Similar to the section before, the combination of various data and information to build this section. Indicated that the thickness of coral reef limestone decrease to the south-west (Loilubu area) and increase to the north (Uatabo beach). Recharge area in the Loilubu (1500 mm/yr) area and discharge in the gravity sliding zone (Baucau old town to Uatabo beach).

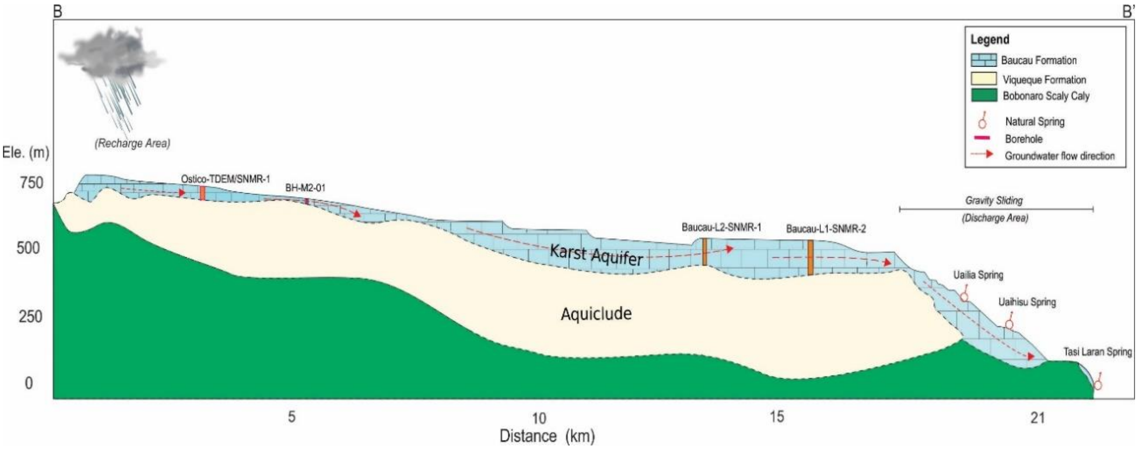

Figure 5. 13 Cross section B-B’, this ection from Loilubu to Uatabo beach

Uailia and Uaihisu natural spring are very important for the Baucau old town a region in the north of plateau in supplying drinking water and for irrigation. During heavy rainfall, groundwater level occurs, which causes the numerous unexpected natural spring in the west of Uatabo beach.

The emergence of natural spring in gravity sliding zone aligned with the lineament of karst terrace (see Figure 5.1). Local people were informed that there some spring emerge in the deep sea. Flow rate measurements in a spring located on the Uatabo beach, this spring precisely in a fault aligned with lineaments. Probably, interpreted that this fault as the product of gravity sliding. The discharge water in this spring about 0.6 l/s. The in situ physical measurements of several natural springs occur in Uatabo area as follows. The pH value ranged around 6.8 to 7.3, except the spring in the sea is 8.5 and the EC value is about 1.03 mS. The TDS value ranged from ranged from 280 ppm – 670 ppm and the temperature around 28 degrees Celcius.

In the north-west of Baucau city inferred the which is non-potential for groundwater flow path. As discussed in the geophysical data interpretation before that, the borehole data and field investigation assumed under this area is Bobonaro scaly clay. Thus, there is no drainage connect to the main recharge area, due to isolated by the structure. Several natural springs emerge in the north along the beach of this area are seasonal natural spring. The recharge area of these seasonal springs are the sinkholes in the top of marine terraces. The rainwater infiltrates these sinkholes than flow to the lower elevation (to the beach).

5.3 Result

Cross section A-A' and B-B' provide an insight that the distribution thickness of the Buacau karst aquifer influenced tectonic activity. These sections show that indeed the Baucau karst aquifer thickness controlled by the underlying structure. It is markedly thicker within the syncline and thinner above the anticline structures Viqueque formation. Notice from Figure 5.1 and Figure 5.3, where the vertical section of airborne electromagnetic and thickness map that there are a positive correlation among TDEM information, borehole data and airborne electromagnetic inversion model. In other side anomaly feature of airborne magnetic agreeable to the geological information observed in the field, especially the lateral distribution of Viqueqeu formation (aquicludes layer).

Surface geomorphology similar with underlying layer morphology. Underlying geomorphic unit very important to contribute groundwater flow in the Baucau plateau. It is by providing the space of drainage pattern formation. The degree of karstification also important, wherein the soft layer ground easily enlarge the crack or the fissure of coral-reef limestone. The main flow of groundwater mostly controlled by the underlying structure. Based on the result, the groundwater main flow in the Baucau plateau classified in three zones such: Zone A flows to the Buruai, Aubaca, and Bucoli area. Zone B located in the most southern of the plateau, the groundwater mostly flow to the east. Zone C from Fatumaca continues to the Uatabo beach. Thus, probably the underground drainage trending as in Figure 5.14.

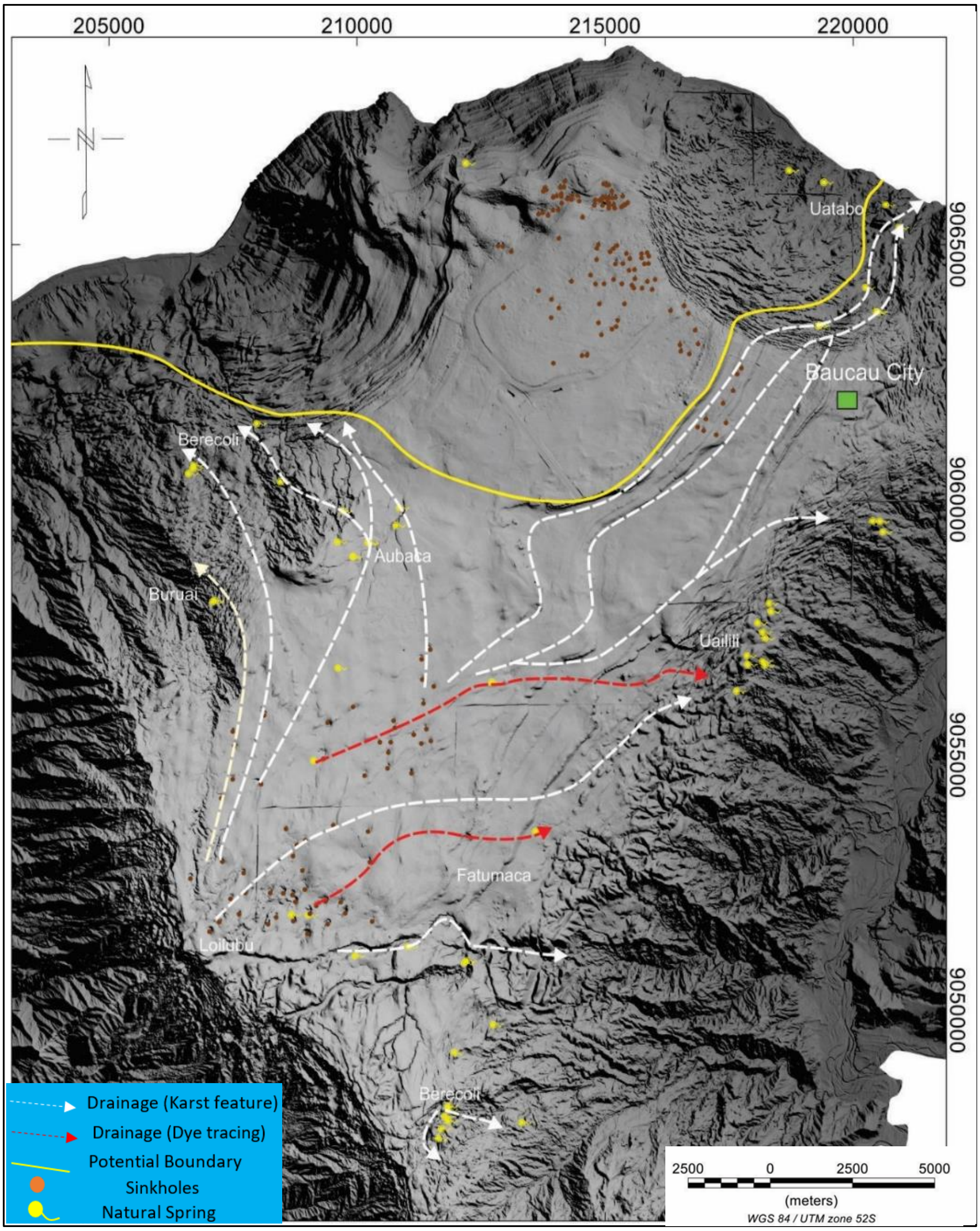

Figure 5. 14 Underground drainage interpreted according to dye tracing and karst feature

The white line interpreted based on the surface feature and the red line according to the dye tracing data. Due to the density of population is high in the Baucau city, the further study must be conducted cross the drainage pattern in the west of Baucau city. According to the field investigation indicated the main underground drainage pattern in the Baucau plateau classified flow to the three different area such as north-west (Bercoli, Buruai, and Aubaca), north (Uatabo) and East (Uailili and Uainoe) (see Figure 5.14).

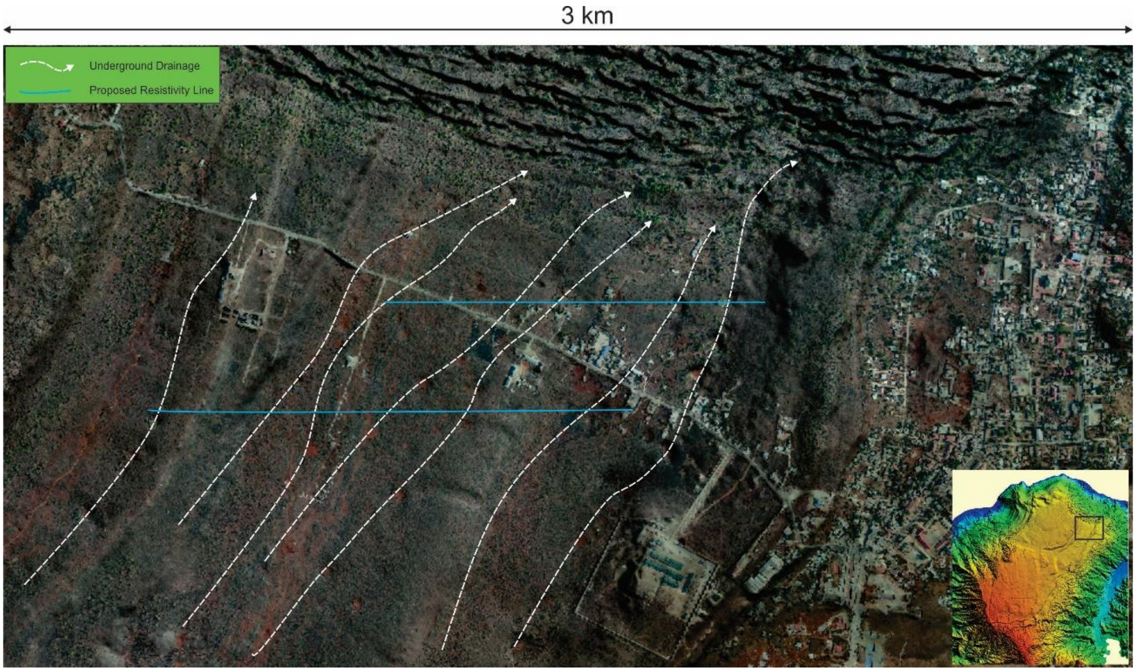

Figure 5. 15 Underground drainage and proposed further resistivity investigation line

Baucau city consists of two cities: old town and new town. Old town situated in the gravity sliding zone. New town situated in the south of old town (see Figure 5.14). Due to localization, new town lack of water supply. In the old town Uailia and Uaihisu natural spring as the main water supply for the local people in that area. Therefore, based on the result recommended conducting more detailed studies in the west of Baucau new town. Resistivity ground survey with high resolution will give more detail underground condition. The resistivity line (blue line in Figure 5.15) intersect the underground drainage (dotted white line in Figure 5.15) was inferred based on surface karst feature.

Chapter 6. Conclusion and Recommendation

6.1 Conclusion

According to the result of geophysical airborne and geological integrating concluded that:

1. Coral-reef limestone deposited in a syncline of Viqueqeu formation with the axes fold to the north-east. Viqueqeu formation composed of marl and grey claystone interpreted as aquicludes and coral-reef limestone acts as groundwater reservoir rock.
2. The coral-reef limestone of Baucau formation thicker in the south-west of plateau and the thickness increase to the north and south of Baucau plateau. The TDEM and borehole data agreeable with vertical section of electromagnetic inversion.
3. The underground drainage pattern fully controlled by the underlying structures, thus the dye tracing data indicated the groundwater flow follow the axes of the fold. The tracer injected in the Uailiabere flow through the drainage with diameter 0.5 m. The dispersion of tracer is low, interpreted related to the variation of diameter and direction of drainage.
4. There are three gravity sliding zone in the study area, mostly natural spring emerge in the gravity sliding. The emergence of natural spring to the surface due to the aquicludes layer closer to the surface. The natural spring emerge in the contact lithology. Natural spring emerge in the Berecoli area interpreted groundwater local flow. Further to the west of Uatabo beach found seasonal spring, due the discontinuity of aquiclude layer.
5. The annual precipitation ranged from 500-1500 mm/yr, high precipitation in the south and decrease to the north. Karstification is high in the south and formed several large numbers of sinkholes and valley. These rainwater infiltrate to the subsurface through these sinkholes (allogenic recharge).
6. Main underground drainage direction: north-west (Berecoli and Buruai), north (Uatabo) and east (Uainoe and Uailili).

6.2 Recommendation

1. Ground geophysical investigation (resistivity method) to prove the underground drainage in the area as mentioned in Chapter 5.
2. Further detailed geological investigation along the escarpments to reveal the detailed structure of the aquicludes (Viqueqeu formation).
3. Protect the sinkholes from the pollutant (trash, other danger chemical element), due to they could easily pollute some spring that emerges in the surface, especially in spring that has a direct connection with the dumped sinkhole.

References

Audley-Charles, M. G., 1968.Geology of Timor Portugues. Geol. Soc. Lond. Mem

Arab-Amiri.A.R, Moradzadeh.A ,Fathianpour.N ,Siemon.B,.2010. Inverse modeling of HEM data using a new inversion algorithm. Journal of Mining & Environment, Vol.1, No.2, 2010, 9-20.

Arisoy M O and Dikmen U., 2013. Edge Detection of Magnetic Sources Using Enhanced Total Horizontal Derivative of the Tilt Angle. Bulletin of the Earth Sciences Application and Research Centre of Hacettepe University 34 (1), 73-82

Blakely, R.J. and Simpson, R.W., 1986, Approximating edges of source bodies from magnetic or gravity anomalies, Geophysics, 51, 1494-1498.

Benischke., 2007.Tracer techniques, in Goldscheider, N., and Drew, D., eds., Methods in Karst Hydrogeology: Leiden, Taylor & Francis, International Contributions to Hydrogeology 26, p. 147–170.

Castro.L.G, Ferreira.F.J, Barros.A, Bongiolo.S, Romeiro.M.A.T, Souza.J. 2010. Realce do gradiente horizontal total de anomalias magnéticas usando a inclinação do sinal analítico. Parte II - Aplicação a dados reais. IV Simpósio Brasileiro de Geofísica

Chappell, J., and Veeh, H., 1978, Late Quaternary tectonic movements and sea-level changes at Timor and Atauro Island: Geological Society of America Bulletin, v. 89, p. 356-368

Cooper.G.R.J and Cowan.D.R.,2004. Filtering using variable order vertical derivatives.Computers & Geosciences 30(5):455-459.

Cordell, L., and V.J.S. Grauch, 1985. Mapping basement magnetization zones from aeromagnetic data in the San Juan basin, New Mexico, in W. J. Hinze, ed., The utility of regional gravity and magnetic anomaly maps: SEG, 181-197.

Cox.N.L,.2009. Variable Uplift from Quaternary Folding along the Northern Coast of East Timor, Based on U-series Age Determinations of Coral Terraces. Master Thesis of Department of Geological Sciences Brigham Young University

Demiroglu.M., 2016. Classification of karst springs for flash-flood-prone areas in western Turkey. Natural Hazard and System Science. Doi: 10.5194/nhess-16-1473-2016

Dentith.M and Mudge.S.T,.2014. Geophysics for the Mineral Exploration Geoscientist. Cambridge University Press

Fraser.D.C,.1978. Resistivity mapping with an airborne multicoil electromagnetic system. – Geophysics 43: 144–172.

Ford C & Williams ., 2007. Karst hydrology and geomorphology. Chichester Wiley.
Fairhead.J.D, 2004. GRAVITY AND MAGNETICS IN TODAY'S OIL & MINERAL INDUSTRY. School of Earth Sciences, University of Leeds, Leeds LS2 9JT, UK

Furnes.,2011. Baucau Limestone Dye-Tracing Experiment. Unpublished report

Grant, F. and West, G., 1965, Interpretation Theory in Applied Geophysics, Mc Graw-Hill.

Gunn, P.J,.1975. Linear Transformation of Gravity and Magnetic Fields. Geophysical Prospecting, 23, 300-312. https://doi.org/10.1111/j.1365-2478.1975.tb01530.x

Gunn J., 2004. Encyclopedia of Caves and Karst Science. Taylor and Francis Group, London Great Britain.

Harris, R., 1991. Temporal distribution of strain in the active Banda orogen: a reconciliation of rival hypotheses: Journal of Southeast Asian Earth Sciences, v. 6, no. 3/4, p. 373-386.

Hinze.J.W, Frese.R.V, and Saad.A.H,.2013. Gravity and Magnetic Exploration Principles, Practices, and Applications. Cambridge University Press

Huang.H and Fraser.D.C,.1999. Airborne resistivity data leveling. GEOPHYSICS, VOL. 64, NO. 2 ; P. 378–385

John,S_. Application of Electromagnetic and Electrical Resistivity Methods in Investigating Groundwater Resources of The Sunyani Municipality in The Brong-Ahafo Region of Ghana. Master degree thesis of Kwame Nkrumah University of Science and Technology Ghana. (http://ir.knust.edu.gh/bitstream/123456789/6261/1/SOMIAH%20JOHN.pdf access on 01 Feb 2018)

JAIN,S., 1988. Total Magnetic Field Reduction-The Pole or Equator? A Model Study. Canadian Journal Of Exploration Geophysics.Vol.24,No.2; P 185-192.

Joy P. Michaud. J.P and Wierenga.M., 2005. ESTIMATING DISCHARGE AND STREAM FLOWS A Guide for Sand and Gravel Operators. Washintong State Department of Ecology

Kass.W,.1998.Tracing Technique in Geohydrology. A.A.Balkema Netherlands

Kirsch.R,.2009. Groundwater geophysics a tool for hydrogeology 2nd. Ed. Springer

Kass.W,.1998. Tracers Technique in Geohydrology. A.A.Balkema, Netherlands

Kavousi A and Raeisi E., 2014. Estimation of Groundwater Mean Residence Time in Unconfined Karst Aquifers Using Recession Curves. Journal of Cave and Karst Studies, v. 77, no. 2, p. 108–119. DOI: 10.4311/2014ES0106

Kearey.P, Brooks.M and Hill.I, 2002. An Introduction to Geophysics Exploration. 3rd edition Blackwell Science Ltd

Komolafe A A., Kuria Z N., Woldai T., Noomen M and Anifowose A Y B., 2013. Investigations into the Tectonic Faults on Magadi Geothermal Field Using Ground and Aeromagnetic Data. Physical Review & Research International 3(4): 385-406

Ley-Cooper and Munday T J., 2011. Aquifer Characterization in Timor-Leste using Ground Electromagnetics. CSIRO: Water for a Healthy Country National Research Flagship Technical Report: EP-22-08-11-43.

Ley-Cooper and Davis A C.,2015a. Assessment and modelling airborne electromagnetic data, over the Baucau limestone Timor-Leste. Technical report, CSIRO, Australia.

Ley-Cooper and Davis A C., 2015. Baucau Region Report: Surface Nuclear Magnetic Resonance. CSIRO Land and Water Technical Report (EP-15-14-35).

Loke,2004**.** Tutorial : 2-D and 3-D electrical imaging surveys.Geotomo Software Pty Ltd

Lowrie*.W,. 2007.* Fundamentals of *Geophysics*, 2nd ed. Cambridge University Press

Masson, DG, Milsom, J, Barber, AJ, Sikumbang, N & Dwiyanto, B 1991, 'Recent tectonics around the island of Timor, eastern Indonesia', Marine and Petroleum Geology, vol. 8, no. 1, pp. 35-49

.

Michaud.J.P and Wierenga.M,. 2005. ESTIMATING DISCHARGE AND STREAM FLOWS A Guide for Sand and Gravel Operators. Washintong State Department of Ecology

Mazor.E.,1991. Applied chemical and isotope groundwater hydrology;New York,Halstead Press

Metzner, J. (1977) Man and environment in Eastern Timor: a geoecological analysis of the Baucau-Viqueque area as a possible basis for regional planning. Australian National University, Canberra.

Metwaly M and Alfouzan F., 2013. Application of 2-D geoelectrical resistivity tomography for subsurface cavity detection in the eastern part of Saudi Arabia. Geoscience Frontiers,4, 469-476

.

MacLeod, I., Vieira, S. and Chaves, A.C., 1993. Analytic signal and reduction-to-the-pole in the interpretation of total magnetic field data at low magnetic latitudes, Third International Congress of the Brazilian Geophysical Society, Rio de Janeiro

Mochales T., Casas A M., Pueyo O., Roman M T., Pocovi A., Soriano M A., Anson D., 2008. Detection of underground cavities by combining gravity, magnetic and ground penetrating radar surveys: a case study from the Zaragoza area, NE Spain. Environmental Geology. Volume 53, Issue 5, p.1067–1077.

Ornai B J.,2017. Cartografia Geológica e Análise da Qualidade de Agua Subterrânea no Aquífero Cársico de Baucau do Posto Administrative de Baucau Vila Município de Baucau. Monografia, Departamento de Geologia e Petróleo Faculdade de Engenharia, Ciência e Tecnologia Universidade Nacional Timor Lorosa'e.

Oyedele K F, Oladele.S, and Emakpor.A.C., 2015., Exploration for limestone deposit at Onigbedu, South Western Nigeria. RMZ – M&G Vol. 63 pp. 139–0150

Palmer.L,.2010. Enlivening development: Water management in post-conflict Baucau city, Timor-Leste. Department of Resource Management and Geography, The University of Melbourne, Victoria, Australia. doi:10.1111/j.1467-9493.2010.00404.x

Pilkington, M., and Keating, P., 2004. Contact mapping from gridded magnetic data –a comparison of techniques, Exploration Geophysics, 35, 206-311.

Reid.A.B, Allsop.J.M, Granser.H, Millet.A.J and Somerton.I.W,.1990. Magnetic interpretation in three dimensions using Euler deconvolution. GEOPHYSICS. VOL. 55

Reid.A.B, Ebbing.J, Webb.J.S. 2013,. Avoidable Euler Errors-the use and abuse of Euler deconvolution applied to potential field.

Rosen S and Vincent J R.,1999. Household Water Resources and Rural Productivity in Sub- Saharan Africa: A Review of the Evidence. Development Discussion Paper No. 673, Harvard Institute for International Development, Harvard University.

Spector, A., and F. Grant, 1970, Statistical Models for Interpreting Aeromagnetic Data: Geophysics, v. 35, p. 293-302.

Siemon B., Christiansen A V and Auken E., 2009. A Review of Helicopter-borne Electromagnetic Methods for Groundwater Exploration. Near Surface Geophysics (Number of magazine)_Vol, p.629-646. DOI: 10.3997/1873-0604.2009043

Siemon.B,.2001. Improved and new resistivity-depth profiles for helicopter electromagnetic data. Journal of Applied Geophysics . 65–76

Smith D V and Pratt D., 2003., Advanced Processing and Interpretation of the High-resolution aeromagnetic Survey data over the Central Edwards Aquifer, Texas, in Proceedings of the Society for the Application of Geophysics to Engineering and Environmental Problems, p. 11.

Smith D V., 2005. The State of the Art of Geophysics and Karst: A General Literature Review. United States Geological Survey

Smith B D., Cain M J., Clark A K., Moore D W., Faith J R and Hill P L., 2005. Helicopter Electromagnetic and Magnetic Survey Data and Maps, Northern Bexar County, Texas. Department of the Interior U.S. Geological Survey

Stella A E M and David F A.,2015. Regional Magnetic Field Trend and Depth to Magnetic Source Determination from Aeromagnetic Data of Maijuju Area, North Central, Nigeria. Physical Science International Journal 8(3): 1-13, DOI: 10.9734/PSIJ/2015/21652

Steuer A., SiemonB., Auken E., 2007. Comparison of Helicopter-borne Electromagnetics in Frequency- and Time-domain at the Cuxhaven Valley in Northern Germany. Journal of Applied Geophysics. Volume 67, Issue 3. p 194-205.

Supper R., Ahl A., Bauer-Gottwein P., Gondwe B., Alonso G G., Romer A., Ottowitz D and Kinzelbach W., 2009. Spatial mapping of submerged cave systems by means of airborne electromagnetics: an emerging technology to support protection of endangered karst aquifers. Near Surface Geophysics , 613-627 DOI: 10.3997/1873-0604.2009008

Telford, W.M, L.P. Geldart, R.E. Sheriff, and D.A. Keys, 1990, Applied Geophysics: Cambridge University Press, Cambridge, p. 792.

Thomson, D. T. (1982) Euldph: A new technique for making computer assisted depth estimates from magnetic data. Geophysics 47

Valleau.N.C,. 2000. Hem Data processing-a practical overview. Exploration Geophysics 31, P 584-594

Wallace.L, 2012.Hydrogeological Map of Timor-Leste.Geoscience Australia, Department of Resources, Energy and Tourism, Canberra, Australia.

Ward, S.H. and Hohmann, G.W., 1988, Electromagnetic theory for geophysical applications, in M. N. Nabighian, ed., Electromagnetic methods in applied geophysics: SEG, 131–311.

White W B.,1988. Geomorphology and Hydrology of Karst Terrains, Oxford University Press, Oxford.

Zhu J., Currens J C and Dinger J S.,2011. Challenges of Using Electrical Resistivity Method to Locate Karst Conduits-A Field Case in the Inner Bluegrass Region, Kentucky. Journal of Applied Geophysics, 75, 523-530. DOI :10.1016/j.jappgeo.2011.08.009

Zobel E.A., 2007. Origin and Tectonic Evolution of Gondwana Sequence Units Accreted to the Banda Arc: A Structural Transect Through Central East Timor. Department of Geological Science Bringham Young University

Internet Site References:

1. https://www.agw.kit.edu/img/Hydro/01_Karst_Block_Diagram.jpg - (Access on May 2018)

2. https://www.liaghannover.de/fileadmin/user_upload/dokumente/grundwassersysteme/burval/buch/089-098.pdf - (Access on March 2018)

3. https://www.mof.gov.tl/about-the-ministry/statistics-indicators/sensus-fo-fila-fali/download-suco-reports/?lang=en – (Access on Abril 2018)

4. seedsoflifetimor.org/wp-content/uploads/2013/01/Rainfall-Map-With Graphs.pdf – (Access on March 2018)